Project No. 13-5039

Multi Resolution In-Situ Testing and Multiscale Simulation for Creep Fatigue Damage Analysis of Alloy 617

Reactor Concepts Research Development and Demonstration

Yongming Liu
Arizona State University

In collaboration with:
Vanderbilt University

William Corwin, Federal POC
Sam Sham, Technical POC

NEUP Nuclear Energy University Programs
U.S. Department of Energy

Multi Resolution In-Situ Testing and Multiscale Simulation for Creep Fatigue Damage Analysis of Alloy 617

Contract No: NU-13-AZ-ASU_-0601-03 (Project 13-5039)

Final Report

Submitted by:

[1]Yongming Liu (PI) and [2]Caglar Oskay (co-PI)

[1]School for Engineering of Matter, Transport and Energy
Arizona State University
Tempe, AZ 85287

[2]Department of Civil and Environmental Engineering
Vanderbilt University
Nashville, TN 37235

April 30, 2017

for
Department of Energy
Nuclear Energy University Program

Abstract

This report outlines the research activities that were carried out for the integrated experimental and simulation investigation of creep-fatigue damage mechanism and life prediction of Nickel-based alloy, Inconel 617 at high temperatures (950℃ and 850℃). First, a novel experimental design using a hybrid control technique is proposed. The newly developed experimental technique can generate different combinations of creep and fatigue damage by changing the experimental design parameters. Next, detailed imaging analysis and statistical data analysis are performed to quantify the failure mechanisms of the creep fatigue of alloy 617 at high temperatures. It is observed that the creep damage is directly associated with the internal voids at the grain boundaries and the fatigue damage is directly related to the surface cracking. It is also observed that the classical time fraction approach does not has a good correlation with the experimental observed damage features. An effective time fraction parameter is seen to have an excellent correlation with the material microstructural damage. Thus, a new empirical damage interaction diagram is proposed based on the experimental observations. Following this, a macro level viscoplastic model coupled with damage is developed to simulate the stress/strain response under creep fatigue loadings. A damage rate function based on the hysteresis energy and creep energy is proposed to capture the softening behavior of the material and a good correlation with life prediction and material hysteresis behavior is observed. The simulation work is extended to include the microstructural heterogeneity. A crystal plasticity finite element model considering isothermal and large deformation conditions at the microstructural scale has been developed for fatigue, creep-fatigue as well as creep deformation and rupture at high temperature. The model considers collective dislocation glide and climb of the grains and progressive damage accumulation of the grain boundaries. The glide model incorporates a slip resistance evolution model that characterizes the solute-drag creep effects and can capture well the stress-strain and stress time response of fatigue and creep-fatigue tests at various strain ranges and hold times. In order to accurately capture the creep strains that accumulate particularly at relatively low stress levels, a dislocation climb model has been incorporated into the crystal plasticity modeling framework. The dislocation climb model parameters are calibrated and verified through experimental creep tests performed at 950℃. In addition, a cohesive zone model has been fully implemented in the context of the crystal plasticity finite element model to capture the intergranular creep damage. The parameters of the cohesive zone model have been calibrated using available experimental data. The numerical simulations illustrate the capability of the proposed model in capturing damage initiation and growth under creep loads as compared to the experimental observations. The microscale analysis sheds light on the crack initiation sites and propagation patterns within the microstructure. The model is also utilized to investigate the hybrid-controlled creep-fatigue tests and has been found to capture reasonably well the stress-strain response with different hold times and hold stress magnitudes.

Contents

List of Figures

List of Tables

1 Overview

1.1 Executive Summary

The objective of this project is to develop novel testing and experimentally validated prediction methodologies for creep-dominated creep fatigue response of Nickel-based superalloy, Inconel 617 (referred to as *Alloy 617*). State-of-the-art experiments and numerical analyses are proposed for the investigation of creep fatigue damage at the temperature range of 850℃-950℃. Specific research objectives to achieve the goal of this project are:

1. Perform multi-resolution testing and imaging analysis to investigate the fundamental creep fatigue damage mechanism
2. Develop a new creep fatigue testing procedure at the coupon level and generate a database for model validation
3. Formulate and implement models for the simulation of creep fatigue damage mechanisms and their interactions at the microstructure scale
4. Conduct microstructure simulations to arrive at a better understanding of creep fatigue mechanism while developing a microstructure-informed and experimentally validated phenomenological life prediction model.

The overall tasks performed at Arizona State University to achieve the specific research objectives (1) and (2) are as follows:

1. *Development of a novel creep-fatigue loading waveform to generate creep dominated damage.* An experimental testing procedure is proposed for generating creep-dominated creep-fatigue interaction data for Alloy 617 at 950C. Existing experimental studies on elevated temperature creep-fatigue of Alloy 617 employ purely strain-controlled loading waveforms with a tensile hold period at peak strain. Rapid stress relaxation of Alloy 617 implies that strain-controlled loading can only generate interaction in the fatigue-dominant regime of the damage interaction diagram. Establishment of design rules for nuclear components require creep-fatigue test data in the creep-dominant regime. This chapter shows details of multiple creep-fatigue loading waveforms that aim at producing creep dominated interaction. The custom loading waveforms are implemented on a servo-hydraulic load frame with a furnace. A hybrid-control scheme with strain-controlled ramps and force-controlled hold periods is selected for further testing, due to its flexibility in generating varying proportions of creep and fatigue damage. Experimental

data is presented and different loading schemes are compared with special emphasis is on the creep and fatigue damage contribution by the newly proposed testing method.

2. *Image-based investigation of creep-fatigue damage and damage evolution through interrupted testing.* Creep dominated creep-fatigue interaction is achieved using a hybrid-control creep-fatigue loading profile, as opposed to the traditional strain-controlled loading. Qualitative and quantitative image analysis of failed test specimens through SEM, EDS, and EBSD, is used to show that hybrid control testing is capable of producing creep dominated failure. Moreover, it is shown that the time fraction rule is not a reliable indicator of creep damage. The focus of image analysis is on surface fatigue cracks and internal creep voids. A creep-fatigue damage interaction diagram based on these micro-scale features is plotted. It is shown that the classical time fraction rule suggested in the ASME draft code for Alloy 617 has a poor correlation with observed microscale damage features. A new definition of creep damage fraction based on an effective hold time is found to correlate well with the micro-scale image analysis.

3. *Creep-fatigue life assessment using an effective time fraction approach.* A new life prediction method for high temperature creep-fatigue in Alloy 617 is proposed. The method is based on the results form hybrid-controlled creep-fatigue loading as well as evidence gathered from image-based analysis of micro-scale damage features using scanning electron microscopy. First, existing life prediction methods and testing procedures for Alloy 617 at high temperatures are reviewed. Emphasis is on the time-fraction type of models as they are widely used in design. Following this, a phenomenological life prediction model (named effective time fraction approach) is proposed by correlating a new time fraction parameter with the micro-scale imaging results. Application of the new approach to hybrid-controlled testing and classical strain-controlled testing is shown with derivations. Next, life prediction using this new method is demonstrated for both hybrid-controlled and strain-controlled tests at 850C and 950C. Detailed discussions on the comparison of the proposed effective time fraction approach and the classical time fraction approach are given. Finally, some conclusions are drawn and further extensions of this model are suggested.

4. *Creep-fatigue life assessment using a unified viscoplastic model with damage.* A unified viscoplastic model is coupled with a non-linear damage accumulation law to predict creep-fatigue life for hybrid-controlled tests. The constitutive law is modified by a damage rate model linked with the dissipation of hysteresis energy through cyclic fatigue deformation and creep deformation. Several major conclusions are drawn: The constitutive law coupled with damage shows the cyclic softening behavior for both peak stress response and effective Youngs mod-

ulus; the hysteresis energy related to fatigue deformation shows almost linear variation with respect to the number of cycles, while the hysteresis creep energy shows a power law increase with respect to the number of cycles; a nonlinear damage accumulation law by taking the power of the fatigue energy and creep energy fractions shows a good correlation with the final failure life. The current testing and simulation results suggest a power of 1/3 as an estimate for the non-linear damage accumulation law. In general, the proposed methodology shows good agreement with the experimental data for both hysteresis response, cyclic softening and life prediction.

The overall tasks performed at Vanderbilt University to achieve the specific research objectives (3) and (4) are as follows:

1. *Develop ment of a crystal plasticity model to idealize the fatigue and creep-fatigue cycles of IN 617 at high temperature environment.* The CPFE model that incorporates isothermal deformation behavior of the alloy as well as the large deformation kinematics has been formulated, implemented and validated. The proposed CPFE model includes a new slip resistance evolution law that accounts for the solute-drag creep and can capture the transient softening effects observed under fatigue and creep-fatigue tests. Model parameters in the CPFE model are calibrated by employing a model calibration procedure that is based on Gaussian Process modeling to accelerate the process. Simulations were performed using polycrystal morphologies generated using experimental (i.e., EBSD) data along with the calibrated CPFE model. The simulation predictions were found to be in good agreement with all fatigue and creep-fatigue tests at different strain ranges and hold times.
2. *Enhancement of the CPFE model by incorporating dislocation climb mechanism and intergranular damage modeling through cohesive zone modeling.* This part of work is built on the previous glide-based CPFE framework and incorporates a dislocation climb model originally proposed by Lebensohn and coworkers [110, 111] for capturing the viscoplastic deformation within the grains while grain boundary damage is modeled by CZM. The CPFE and the CZ models work in tandem to compute the viscoplastic deformation as well as progressive failure in the material microstructure. Model parameters are calibrated and validated using experimental creep tests at different hold stress amplitudes. Microscale stress and damage distribution as well as their evolution during the creep process are analyzed to gain further understanding of the underlying deformation mechanisms.
3. *Employment of the developed CPFE-CZM model to investigate the hybrid-controlled creep-fatigue test.* A fully automated multiple cycle hybrid-controlled test modeling approach is developed using Abaqus-Python scripting to implement the switching between strain- and

stress controlled loadings. The model is used to study the multiple cycle response of the hybrid-controlled tests, which further demonstrates the prediction capability of the model.

1.2 Report Organization

This report is organized as follows: Chapter 2 provides the background and literature review on experimental and numerical study of Alloy 617 at high temperature. Chapter 3 introduces a hybrid-control loading waveform that is capable of generating creep dominated creep-fatigue interaction. Chapter 4 investigates the creep and fatigue dominated regimes of interaction by analyzing sectioned surfaces of failed test sepecimens. The focus of damage analysis is on fatigue induced surface cracks and creep induced voids. Chapter 5 introduces a new method for calculating creep damage, as an alternative to the classical time fraction rule, in an effort to improve life prediction. The new method is validated by using a database of creep-fatigue tests. Chapter 6 proposes a more detailed life prediction model that uses constitutive modelling and a damage variable that is calibrated by analysis of hysteresis energy and cyclic softening. Chapter 7 describes the development, implementation and verification of an isothermal, large deformation CPFE model that considers dislocation glide as the only source of plastic deformation and assumes full-bonded grain boundaries. This model also focuses on proposing a new slip resistance evolution equation that captures the stress-softening observed in first cycle fatigue and creep-fatigue response as well as persistent re-emerging in subsequent creep-fatigue cycles after each strain hold. The extension of the CPFE model to incorporate dislocation climb mechanism for the grain deformation as well as the coupling with CZ model for intergranular damage modeling are presented in Chapter 8. The model is verified using creep tests of different hold stress magnitude. Detailed microscale analysis of deformation and damage is conducted to investigate the deformation as well as damage initiation and propagation characteristics. The application of the CPFE-CZM model to investigate the hybrid-controlled creep-fatigue tests devised in this project is presented in Chapter 9. The model is used to study the multiple cycle response of the hybrid-controlled tests, which further demonstrates the prediction capability of the model. Chapter 10 concludes the major finding of this project.

2 Background and Introduction

Creep-fatigue is an important damage mechanism in high-temperature systems that undergo cyclic thermal stresses interspersed with periods of constant load. Examples of such systems include gas turbines, heat exchangers, and microelectronics packaging [1,2]. Recent interest in creep-fatigue interaction in superalloys is driven by the need to evaluate structural materials for future nuclear power plants. The Very High Temperature Reactor (VHTR) is one of six conceptual designs proposed for Generation IV nuclear reactors. The VHTR is a gas-cooled reactor with helium as the primary coolant. The coolant is expected to reach temperatures up to 950C at the reactor outlet, before passing through an Intermediate Heat Exchanger (IHX) - which provides process heat for electricity and hydrogen production [3,4]. Steady-state operation of the plant at elevated temperatures leads to creep deformation, whereas loading transients including startup and shutdown generate fatigue [5,6]. Hence, creep-fatigue interaction is expected to be a major damage mechanism for structural materials in the IHX. Alloy 617 - a solid-solution strengthened nickel-base superalloy - is the leading candidate material for IHX tubing due to its thermal stability, creep strength, and oxidation resistance at high temperatures [79]. A detailed understanding of the creep-fatigue interaction in Alloy 617 is necessary before it can be considered as a material for nuclear construction in ASME Boiler and Pressure Vessel Code, Section III, Subsection NH [10].

A majority of current creep-fatigue life prediction methods are based on time fraction rule (TFR), ductility exhaustion (DE), or strain-range partitioning (SRP) [11]. Nuclear component design codes, namely ASME BPVC, Section III, Subsection NH[10], RCC-MR [12], and R5 [13], suggest linear summation of creep and fatigue damage fractions to predict failure. ASME and RCC-MR require a time fraction based on TFR for calculating creep damage, whereas R5 requires a strain fraction calculation based on DE. One limitation of the DE approach is that the value of creep fraction can exceed unity for some materials, leading to highly conservative predictions [11,14,15]. Takahashi [14] proposed a modified ductility exhaustion method to alleviate this limitation. The SRP method works well when enough test data is available to partition the total strain range. Hoffelner [16] improved life prediction in SRP by modifying the creep strain partition. The time fraction rule can be used to predict creep-fatigue life with the help of the following relation:

Nickel-based alloys are widely used as structural materials for turbine engine blades, aircraft engine components, and high temperature power plant steam generators due to their exceptional combination of high temperature strength and creep resistance. In particular, IN 617 is a candidate structural material for very high temperature reactor (VHTR) intermediate heat exchangers [147]. VHTR environments pose significant challenges to structural materials due to the presence of ex-

tremely high temperatures (up to 950°C) combined with mechanical loading for long periods of time [66] as well as fatigue and creep-fatigue induced by the startup and shutdown cycles. Developing a computational model that incorporates the underlying physics of the plastic deformation on IN 617 at hight temperature, which can lead to the ability to capture the response in cyclic and creep loading, and ultimately, life prediction capability is of significant interest.

$$\sum_{i=1}\left(\frac{n}{N_f}\right)_i + \sum_{j=1}\left(\frac{t_h}{T_r}\right)_j \leq D \tag{1}$$

where, n is number of cycles to failure in creep-fatigue tests, N_f is the cycles to failure in pure fatigue for the given strain range, t_h is the hold time in each cycle, T_r is the time to rupture in pure creep for a given stress and temperature and D is the allowable combined damage fraction. In this study, N_f was found from a fatigue strain-life curve and T_r was calculated from a Larson-Miller plot. The first term in Eq. (1) is a cycle fraction representing fatigue damage and the second term is a time fraction representing creep damage. The damage fractions for Alloy 617 at 950℃are expected to follow a bilinear curve on a creep-fatigue interaction diagram [6] as is typical for steels (see Fig. 2.1).

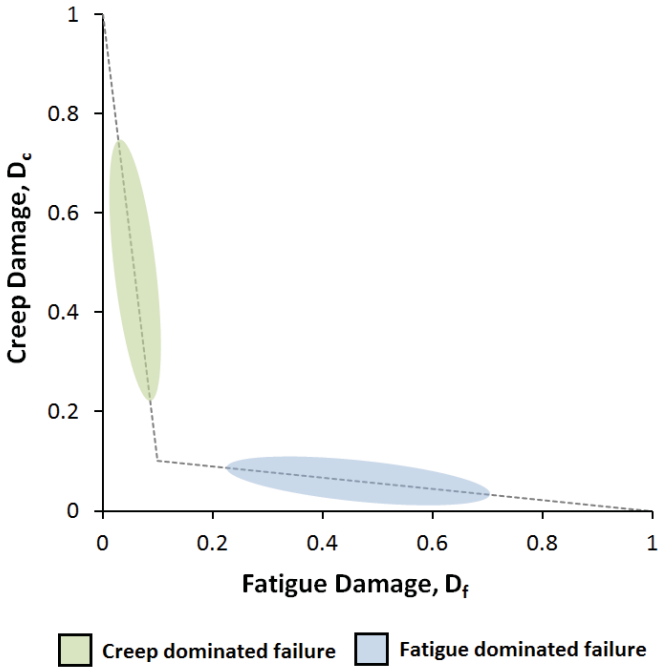

Fig. 2.1: Creep-Fatigue interaction diagram highlighting the creep-dominant and fatigue-dominant regimes.

Traditional strain-controlled tests cannot produce creep-dominated failure due to the rapid stress-relaxation of Alloy 617 at high temperatures. Therefore, force-controlled loading waveform

must be investigated as a means for generating greater creep damage. Additionally, existing creep-fatigue tests for Alloy 617 at 950C, do not show a trend when plotted on an interaction diagram. This is due to unrealistic values of creep damage fraction resulting from the time fraction rule. Exploration of loading waveforms with force-controlled hold periods can directly induce creep damage and therefore act as validation check for the widely used time fraction rule.

Developing a computational model that incorporates the underlying physics of the plastic deformation on IN 617 at high temperature, which can lead to the ability to capture the response in cyclic and creep loading, and ultimately, life prediction capability is of significant interest.IN 617 is a solid solution strengthened nickel-based alloy with coarse Cr and Mo carbides as well as small amount of Ti carbonitrides [159]. γ' phase also exists at relatively low temperatures, but becomes unstable above 650℃ [117, 72]. Tensile tests of IN 617 at various temperatures and strain ranges have been studied and it generally exhibits strong temperature and strain rate dependence [166, 139], as well as orientation (between loading direction and sample rolling direction) dependence [124]. Strain controlled fatigue and creep-fatigue tests of IN 617 at 850℃ and 950℃ have been experimentally studied by several researchers over various strain ranges and hold times [5, 164, 8, 163]. Wright et al. [164] found that under fatigue loading at 850℃, IN 617 deforms by a plastic flow mechanism and shows cyclic hardening, while at 950℃ the alloy exhibits softening induced by solute-drag creep. Introduction of a tensile hold in the creep-fatigue tests significantly decreases the fatigue life compared to that under pure fatigue loading. Microstructure examinations showed failure is controlled by intergranular fracture under creep-fatigue loading, while transgranular cracking dominates when subjected to pure fatigue loads [8]. Further, the microstructure is marked by the formation of dislocation substructures during creep-fatigue testing, which influences the dislocation density and motion within grains [7]. The sensitivity of fatigue and creep-fatigue deformation and failure mechanisms to environmental (e.g., temperature) conditions points to the influence of microstructure on the life of this alloy.

A few viscoplastic constitutive models [52, 137, 126] based on the phenomenological constitutive theories of Robinson [140] and Chaboche [83] have been developed to capture the cyclic response of IN 617 at high temperatures. Chen et al. [5] utilized frequency-modified tensile hysteresis energy to predict the low cycle fatigue and creep-fatigue life of IN 617. While these phenomenological models are successful in capturing the stress-strain loops, they do not provide a direct account of microstructural heterogeneities and their interactions, which affect the overall long term behavior. Crystal plasticity finite element method (CPFE) is an alternative modeling approach, which is based on full resolution of the representative microstructure of the material. Since its inception [133, 134], CPFE has been developed into a robust numerical strategy to capture the grain level anisotropic

deformation of metals and alloys at various loading conditions (see, e.g., Roters et al. [141] for an extensive review). Under the assumption that slip is the dominant carrier of plastic deformation, stress is resolved onto individual slip systems inherent to the lattice structure of the material, which drives dislocation glide and the accumulation of plastic strain. More recent investigations incorporated dislocation climb mechanisms [112], as well as deformation twinning [97] into the CPFE framework to study the high temperature behavior of alloys. A number of numerical investigations employed CPFE to study the cyclic response of various alloys, either to capture the stress-strain response, crack initiation or failure life prediction [170, 171, 160, 67]. Simulations of the cyclic behavior of nickel-based alloys at intermediate and high temperatures have been performed in Refs. [77, 78, 115], which demonstrated the capability of CPFE to capture hysteresis loops as well as the stress relaxation phenomenon.

Experimental studies by Benz et al. [73], Kim et al. [101, 103], Lillo and Wright [113], Lillo et al. [114], Martino et al. [120], Roy et al. [143], and Wright et al. [162] recently investigated the behavior of IN 617 subjected to creep loads at high temperatures under various levels of applied stresses. Experimental observations of microstructures using optical microscopy show significant atomic mobility and creep deformation even at relatively low stresses. As observed in experimental creep curves [72, 73, 101, 102, 143], a relatively short primary and secondary creep regime is followed by a long tertiary creep regime. In particular, a well-defined secondary creep was not observed. A rapid rise in creep rate caused by an increase in mobile dislocation density can reduce or exclude the secondary creep stage. This is known as sigmoidal creep behavior, and has been observed in Nickel-based alloys [156].

A primary mechanism for creep strains is dislocation climb resulting in a power law creep behavior of metals at high temperatures [125]. Prior experimental observations performed on creep deformation of IN 617 indicate that the minimum creep exponent typically lies between 5-7 within the 850-950°C temperature range [73, 103, 25]. This range indicates the presence of combined dislocation glide and climb [98], typically observed for class II alloys.

Dislocation climb that results from the interactions between dislocations and local non-equilibrium concentrations of point defects at high temperature contributes significantly to the irreversible deformation under creep loads [110, 111]. Therefore, it is necessary to include dislocation climb mechanism into a microstructure model to capture the viscoplastic deformation under high temperature loading conditions. Lebensohn et al. [110] extended their visco-plastic self-consistent (VPSC) formulation to consider coupled glide-climb mechanism and arrived at improved predictions of the behavior of olivine polycrystalline aggregates. Geers et al. [87] proposed an extended strain gradient crystal plasticity model by incorporating the effects of dislocation climb into the plastic strain

evolution in the context of strain gradient plasticity. The coupled glide-climb theory was verified through analysis of dislocation interactions in either bypassing of an elastic precipitate or destruction of dislocation pile-ups at the mesoscale. Huang et al. [95] investigated the influence of dislocation climb on the grain size dependent response and its underlying mechanisms. Other investigations (e.g., [91, 167]) employed discrete dislocation dynamics framework to study single crystal Ni-based superalloys. Vacancy diffusion-induced dislocation climb was found to be critical to describe the strain rate effect on the early plastic behavior of high-temperature and low-stress creep of Ni-based superalloys.

Post-mortem microstructural examinations by Kim et al. [101, 102] revealed that the creep damage and fracture in IN 617 is predominantly intergranular. Creep damage and ultimate rupture have been linked to the formation, growth and coalescence of grain boundary cavities, in addition to oxidation and other mechanisms. The recent experimental study by Tahir et al. [40] also confirms that damage caused by creep is of intergranular in nature.

Some recent numerical investigations employed combined CPFE-CZM approach to model damage behavior at individual grain boundaries in plastically deforming metals [82, 149, 150, 108]. Simonovski and Cizelj [149, 150] demonstrated the initiation and evolution states of the intergranular cracking using cohesive zone in 3D polycrystalline aggregates for AISI 304 stainless steel. In the work of Kupka and coworkers [108] for an Aluminum-Lithium alloy, a fracture analysis is performed using cohesive zone modeling of the grain boundary, which allows for a mechanism independent description of the fracture process. Gonzalez et al. [89] adopted a CPFE model that embedded isotropic cohesive elements at grain boundaries to examine the effect of elevated grain boundary stresses on fracture behavior. While creep fracture phenomenon observed in experiments [68, 99] were numerically modeled by Onck and van der Giessen [127, 128] for a polycrystalline material at the microscale, a combination of CPFE and CZM has not been used, to the best of the authors' knowledge, in capturing creep deformation and simulating the formation and growth of cavities in polycrystalline aggregates.

In this project, creep-fatigue tests are performed with novel loading waveforms; damage features in failed test specimens are quantified and analyzed; two life-prediction methodologies, one empirical and the other based on constitutive response, are proposed; and a computational microstructure model is developed to capture creep deformation and failure behavior in Alloy 617 operating in high temperature environments. The microstructure model is based on an isothermal, large deformation CPFE formulation and idealizes the deformation in the crystal lattice as collective glide and climb of dislocations and damage in grain boundaries using cohesive zone model. In general, the project framework is as follows:

- Propose novel test procedures to generate creep-dominated creep-fatigue interaction with the introduction of force-controlled tensile hold periods.
- To qualitatively and quantitatively distinguish between creep and fatigue dominated damage in failed creep-fatigue test specimens using Scanning Electron Microscopy (SEM), Electron Backscatter Diffraction (EBSD), Energy Dispersive Spectroscopy (EDS) and optical profilometry.
- Propose a life prediction methodology based on the findings from micro-scale damage analysis.
- Obtain an improved life-prediction by modeling the constitutive response of the material under creep-fatigue cycling using a unified viscoplastic model with damage.
- Develop a CPFE framework considering dislocation glide only with a focus on a new flow rule to characterize the solute-drag creep effects to capture the first cycle response of the fatigue and creep-fatigue tests.
- Incorporate dislocation climb model to accurately capture creep deformations particularly at stress levels significantly less than yield.
- Combine proposed CPFE model with cohesive modeling at grain boundaries to capture intergranular fracture. The model is employed to study the hysteresis response under fatigue and creep-fatigue loading, and fracture under creep and creep-fatigue conditions.

3. NEW CREEP-FATIGUE EXPERIMENTAL TESTING METHOD

3.1 INTRODUCTION

Several experimental studies have been conducted in the past to investigate the creep-fatigue behavior of Alloy 617 at elevated temperatures. Rao et al.[16] conducted strain-controlled creep-fatigue tests on Alloy 617 at 950°C in a helium environment to determine the effect of strain rate, hold time, and hold condition (i.e., tension or compression hold) on the creep-fatigue lives. They concluded that introducing a hold period at peak strain reduced the cycle life and that a tension hold was more damaging than either a compression hold or a combination of tension and compression hold. They also observed that tests with short tensile hold periods produced transgranular cracks whereas tests with tensile hold periods longer than 10 min produced intergranular cracks. Fatigue dominated failures are typically accompanied by transgranular cracking whereas creep dominated failures are accompanied by intergranular cracking and creep cavitation [17]. However, Cabet et al.[17] carried out strain-controlled creep-fatigue tests on Alloy 617 at 950°C in air and observed intergranular cracking but no grain boundary cavitation, even with hold times as long as 1800s with a strain range of 0.6%. This suggests that generating creep-dominant creep-fatigue testing data will be very difficult using purely strain-controlled testing, which is due to the very rapid stress relaxation for materials at high temperatures. For component design against creep-fatigue, the classical strain-based testing method will be insufficient to provide enough data to construct the damage diagram (see Fig. 1.1).

The ASTM standard for creep-fatigue testing E2714-13 provides examples of strain-controlled loading profile with a hold at peak strain and force-controlled loading profile with a hold at peak stress. For Alloy 617, it is known that tensile hold periods are more damaging than compressive hold periods [16,18]. Moreover, for a purely strain-controlled loading profile, the stress during the hold period becomes steady after the initial rapid stress relaxation. Therefore, after a certain threshold value, a longer hold time does not produce more creep damage. To solve this problem, Fournier et al. [19] conducted tests with a force-controlled hold period on 9Cr-1Mo martensitic steel at 550°C. They observed that fatigue life was reduced but the creep damage remained low. Simpson et al. [6] suggested that, for Alloy 617 at 950°C, creep-dominant damage may be produced by a loading profile similar to one used by Fournier et al. [19], but there is no experimental evidence to support this hypothesis. In addition, TFR does not fully account for the dependence of life on the type of loading waveform so it can be inaccurate when applied to unconventional creep-fatigue loading [10,11]. Thus, any new testing method for generating creep fatigue data must be carefully investigated with respect to the TFR methodology.

Based on the above brief review and discussion, the objective of this study is to experimentally explore the possible creep-fatigue testing procedures for generating creep-dominant failure, which will aid in the construction of a damage interaction diagram for creep-fatigue design. Several non-traditional creep-fatigue loading profiles, such as stress-controlled, hybrid control with specified hold time, hybrid control with specified

hold strain, and cyclic ratcheting are investigated and compared for their suitability for producing creep-dominant damage.

3.2 EXPERIMENTAL PROCEDURE

An MTS servo-hydraulic load frame equipped with a high temperature furnace was used to conduct the creep-fatigue tests. The specimens of Alloy 617 were standard round-section specimens with tangentially blending fillets and button-head ends with a gage length of 20mm and gage diameter of 7.5mm. The long axis of the specimen was parallel to the rolling direction. All tests were performed at constant temperature of 950°C using a furnace that consisted of three pairs of silicon-carbide heating elements. Temperature control was achieved with K-type thermocouples wrapped on to the specimen using silica wick. Four thermocouples were used: two on the grips and two the specimen shoulders. The temperature difference along the gage length was controlled to be less than 10°C for all tests. Strain measurement was achieved by an air-cooled high-temperature extensometer with ceramic extension rods which maintained contact with the gage length of the specimen. The maximum range for the extensometer was 24% strain so for tests with larger total strain - e.g. due to ratcheting – the extensometer had to be reset within the test. A strain rate of 1×10^{-3}/s was used for all strain-controlled ramps. A hand pump was used to apply a pressure of 200 psi to the grips. It was observed that applying a higher pressure caused damage to the grips and specimen at 950°C. The experimental setup is shown in Fig. 3.1.

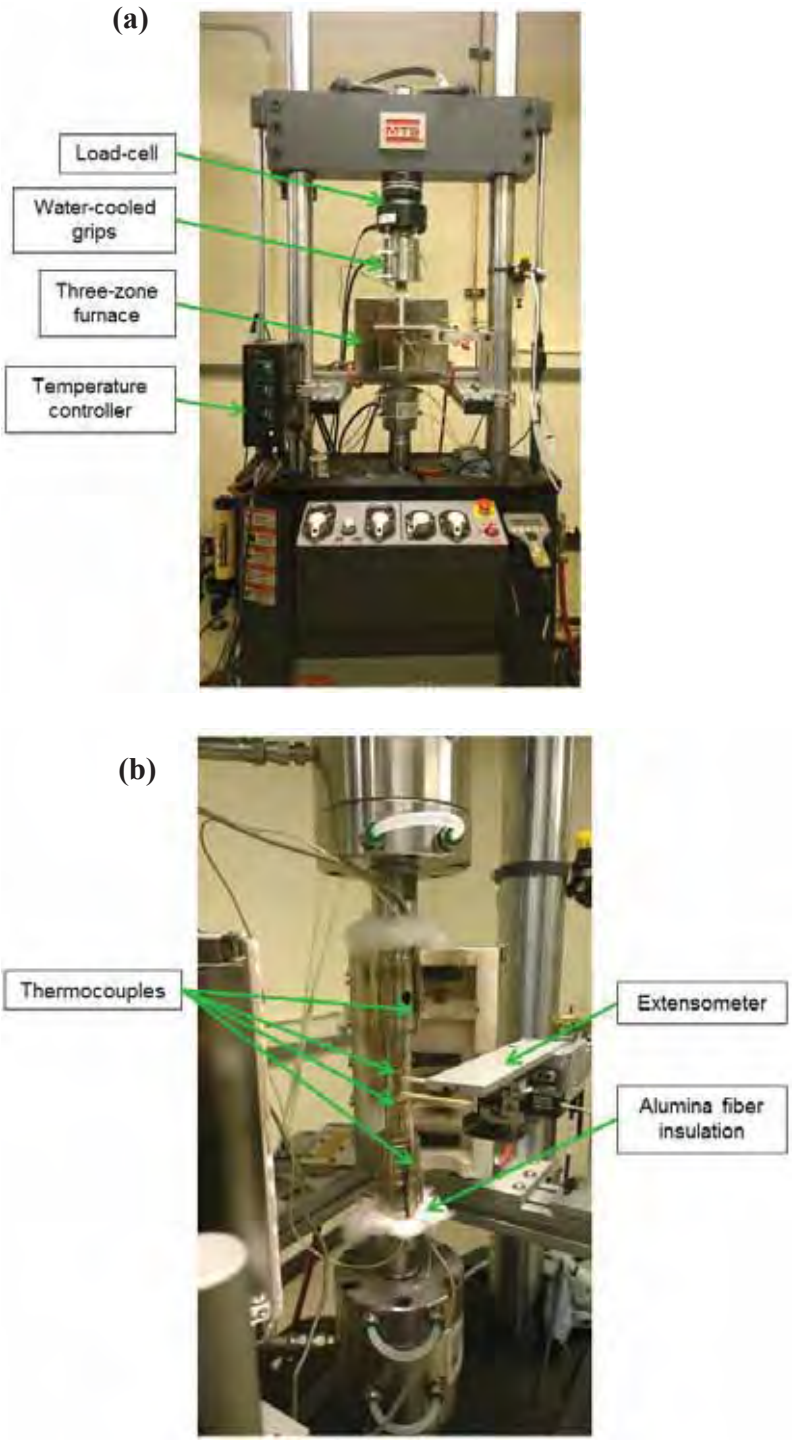

Fig. 3.1 – (a) Load frame with high-temperature system; (b) Test specimen installed between grips.

Traditional strain-controlled fatigue stress-relaxation testing of Alloy 617 at 950°C cannot populate the creep-dominant part of the creep-fatigue interaction diagram [6]. Hence, loading waveforms with force-controlled hold must be applied to generate creep-dominant damage. New loading waveforms were implemented to study creep-fatigue interaction in the creep-dominant regime. These waveforms can be classified as: (i) purely force-controlled; (ii) hybrid-control with stress hold at peak strain; (iii) hybrid-control with an intermediate stress hold and (iv) hybrid-control with ratcheting and intermediate stress hold. The term 'hybrid' here, refers to a combination of stress and strain control. The end-of-test criterion for the force-controlled tests was complete rupture whereas for all other tests it was a 50% drop in maximum tensile stress. In these tests, creep strain $\varepsilon_{c,}$ is defined as the strain accumulated during the hold period [19]; fatigue strain range, $\Delta\varepsilon_f$, is defined as the difference between the total strain range, $\Delta\varepsilon_t$, and creep strain. To prevent large data sets, cycle data was collected every 5 or 10 cycles, depending on the expected cycle life of the given test. The loading profiles discussed here were not available in the standard MTS fatigue database, custom loading profiles were programmed in MTS Multipurpose Elite software. Hybrid control requires a switch from a strain-controlled ramp to a force-controlled hold for each cycle. This was achieved in the software by running a force limit detector in parallel with the strain ramp command. The following sections will explain each of the tests in detail.

3.2.1 Purely Force-Controlled Test

The idea behind using force-control is to replace the stress-relaxation part of the traditional strain-controlled loading waveform with creep deformation induced by a

force-controlled hold. The entire test was performed in force-control. Loading and unloading ramps were executed at 1000 N/s, whereas the peak stress was held constant for a fixed time of 30s per cycle as shown in Fig. 3.2(a). The strain amplitude increased with cycles due to softening. The mean strain also increased indicating ratcheting. Fig. 3.2(b) shows the ratcheting behavior between first, mid and last cycles. The ratcheting, in this case, is a consequence of completely reversing the force instead of the strain. Three tests were conducted with stress amplitudes of 40, 55 and 70 MPa respectively. In all three tests, the creep damage fraction, D_c, was greater than unity and fatigue damage fraction, D_f, was close to zero. These fractions suggest highly creep-dominant damage and therefore, an absence of creep-fatigue interaction. It was observed that applying a waveform with higher stress amplitude does not lead to an increase in the fatigue fraction. Applying shorter hold periods may cause a reduction in D_c and an increase in D_f. However, using hold periods less than 30s to produce creep-dominant damage is not recommended because the creep damage incurred during the hold period may be less than the creep damage during the loading and unloading parts of the cycle.

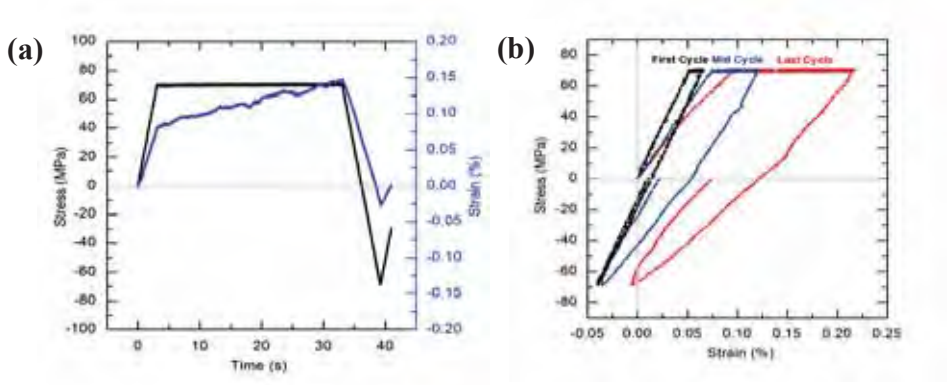

Fig. 3.2 – (a) Applied stress profile and corresponding strain response for one cycle; (b) Stress-strain curves for first, mid and last cycle showing ratcheting. The initial strain is changed to zero to compare the cycles

3.2.2 Hybrid-Control with Stress Hold at Peak Strain

A hybrid-control test, similar to the one conducted by Fournier et al [19] for steels, was investigated for Alloy 617. For the test shown in Fig. 3.3(a), strain is ramped at a rate of 1×10^{-3}/s to 0.45% first. Following this, the control is switched from strain to force and the corresponding force is held constant until the strain reaches 0.75%. Next, strain is reversed to -0.45% in strain control and then this cycle is repeated. In this loading waveform, complete reversal of strain prevents cyclic ratcheting. The peak stress is held constant up to a fixed strain level, the hold time increases with cycles due to softening as shown in Fig. 3.3(b). The sudden increase in stress during the compressive part of the last cycle, seen in Fig. 3.3(a), indicates crack closure. The holding stress in this type of loading waveform can be larger than yield stress. This can lead to creep power law breakdown [20] during the hold period, which is not representative of the operating conditions of an IHX. Additionally, the holding stress corresponding to the

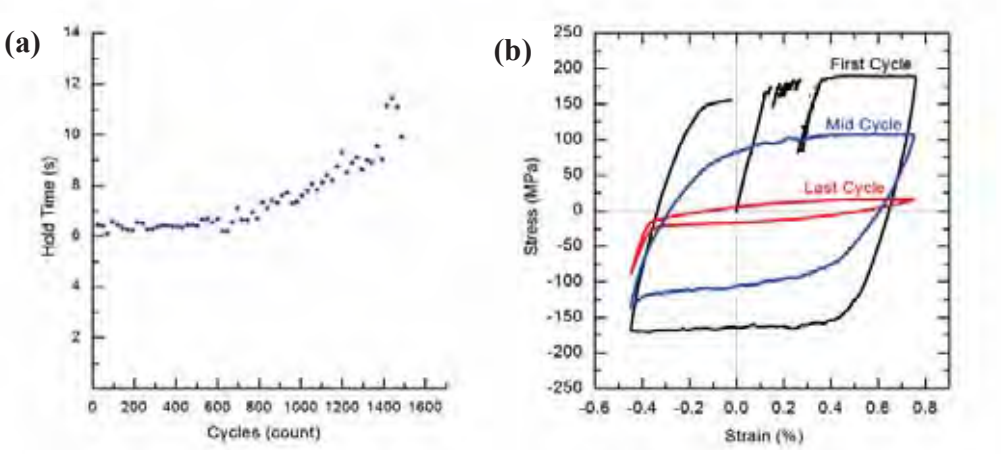

Fig. 3.3 – (a) Stress strain curves for first, mid and last cycle; (b) Increase in hold time with cycles due to softening.

peak strain reduces every cycle due to cyclic softening. This makes the calculation of creep damage fraction cumbersome.

3.2.3 Hybrid-Control with Hold at Intermediate Stress

In time fraction approach, the creep fraction can be varied by changing the hold time and hold stress, whereas the fatigue fraction can be varied by changing the fatigue strain range. A loading profile in which the stress is held constant at an intermediate stress level instead of the stress corresponding to peak strain can allow more flexible control over the creep and fatigue fractions in a test. Moreover, the stress hold does not have to be above the yield stress for the material. This type of loading waveform is also closer to actual service conditions of a heat exchanger where a transient period produces peak stresses, but steady state operation results in intermediate stress levels [21]. Fig. 3.4(a) shows an example of such a loading waveform. The strain is ramped up at a rate of $1x10^{-3}$/s to 0.4%. Following this, strain is reduced until stress is 85MPa and the control is switched from strain to force. Next, the corresponding force is held constant for 10s and the strain is reversed to -0.4% in strain control. This cycle is repeated until failure. Creep hold time per cycle is fixed, the creep strain per cycle increases due to softening as indicated by Fig. 3.4(b).

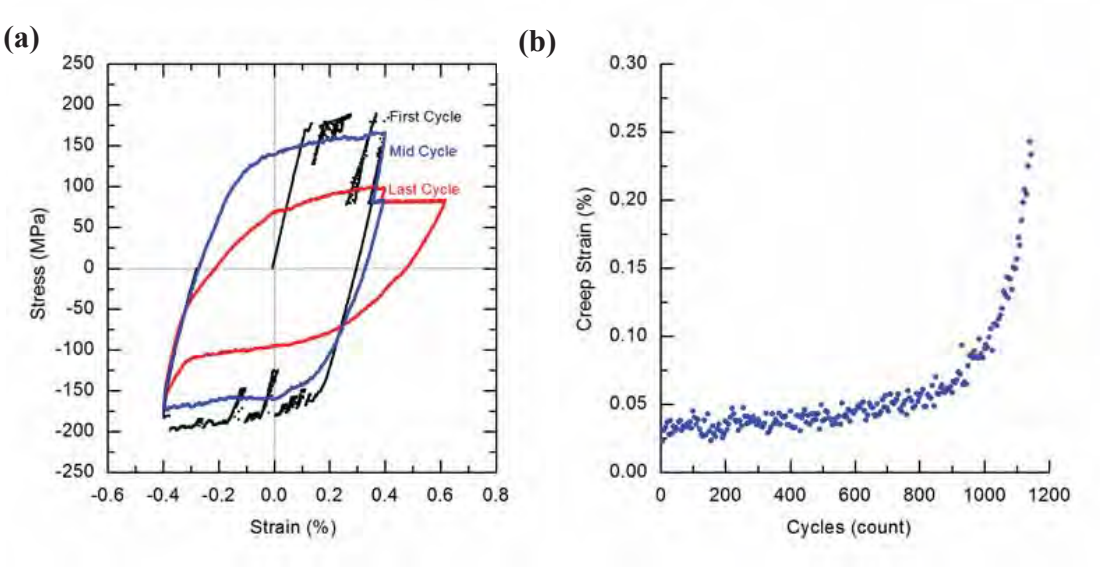

Fig. 3.4 – (a) Stress-strain curve for loading waveform with a 10s hold at 85 MPa; (b) Creep strain increasing with cycles for a fixed hold time of 10s.

In the above loading waveform, stress is held constant for a fixed time each cycle. Another variation of this loading profile is one in which stress is held constant up to a fixed strain each cycle. Fig. 3.5(a) shows a loading waveform with a hold at intermediate stress until a fixed strain of 0.2% is accumulated. Creep strain per cycle is fixed, the hold time per cycle decreases with cycles as indicated by Fig. 3.5(b). Unlike the fixed hold time test, where $\Sigma t_h = n.t_h$, the variation of hold time with cycles must be known to find creep damage fraction in this case.

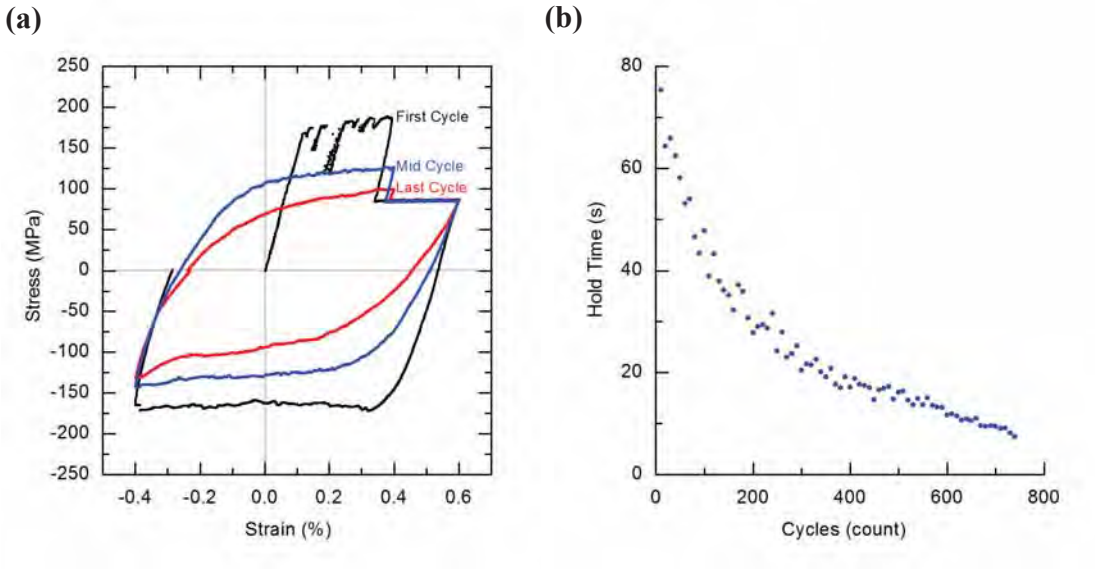

Fig. 3.5 – (a) Stress-strain curve for loading waveform with an 85 MPa stress held constant up to a strain of 0.2%; (b) Hold time decreasing with cycles for a fixed creep strain of 0.2%.

In the aforementioned tests, the value of creep damage fraction was greater than unity. A possible explanation for this result can be the complete reversal of fatigue strain amplitude, which prohibits the accumulation of creep strain with increasing cycles.

3.2.4 Hybrid-Control with Ratcheting and Intermediate Stress Hold

In hybrid-control tests, the fatigue strain range $\Delta\varepsilon_f$ is completely reversed so the creep strain cannot accumulate with cycles. In contrast, for force-controlled tests the creep strain can accumulate with cycles due to ratcheting. The hybrid-controlled loading profile can be modified in such a way that the peak and valley strains increment by a fixed amount each cycle as shown in Fig. 3.6. Since the total strain to failure is approximately 50% and each cycle increments the peak strain by x%, the cycles to failure, *n*, for these tests can be controlled by changing the strain increment, *x*. Therefore,

the fatigue fraction can be treated as a control variable, whereas the creep fraction is the response. It was hypothesized that controlling the fatigue fraction would help in achieving a value of creep fraction that is less than unity.

In this test strain was ramped up at a rate of $1x10^{-3}$/s to 0.4%; strain is reduced until the stress is 85MPa; stress is maintained at 85MPa in force-control until the strain reaches 0.6%; strain is reversed to -0.2% in strain control; Strain is ramped up to 0.6% and the steps are repeated. This leads to a fatigue strain range of 0.8% and a creep strain of 0.2% per cycle.

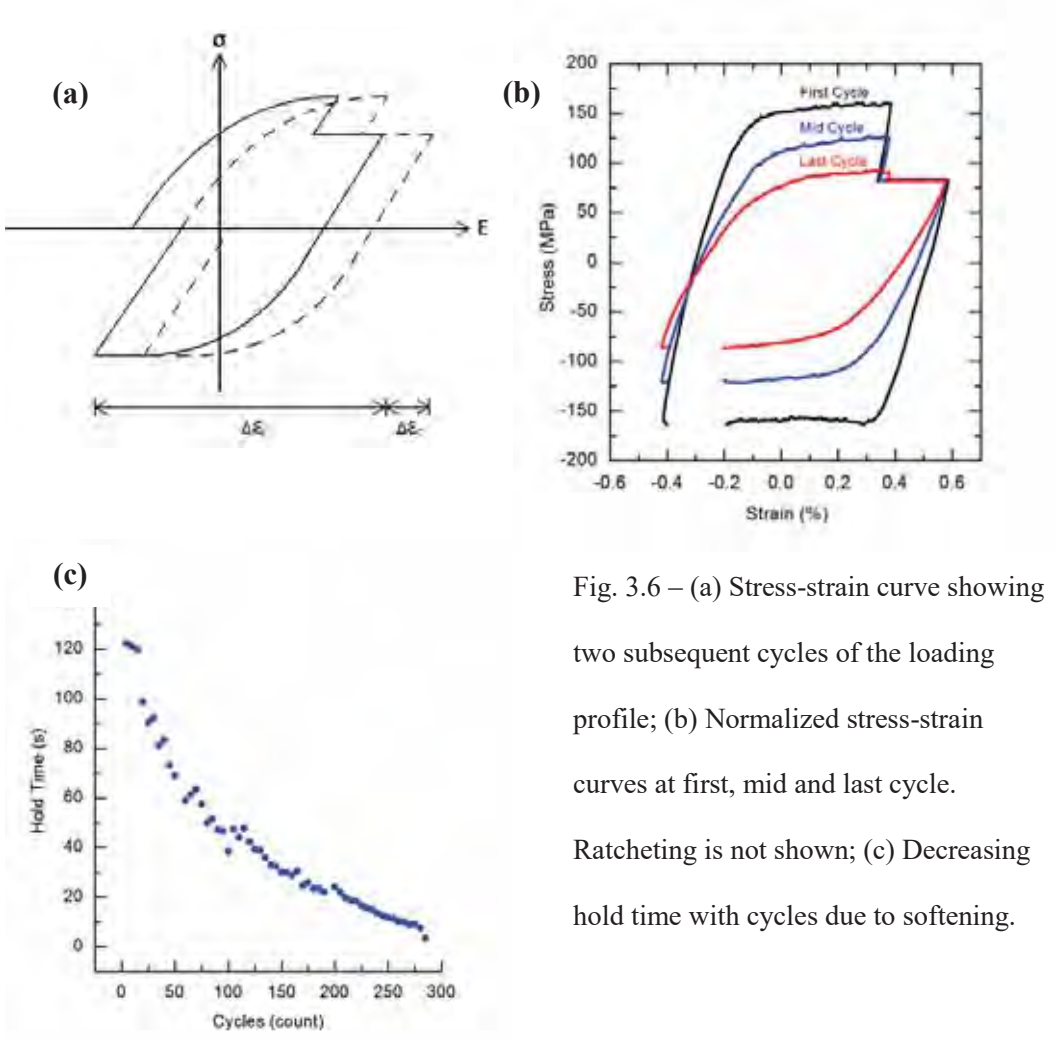

Fig. 3.6 – (a) Stress-strain curve showing two subsequent cycles of the loading profile; (b) Normalized stress-strain curves at first, mid and last cycle. Ratcheting is not shown; (c) Decreasing hold time with cycles due to softening.

In this loading profile, creep fraction is very large due to the ratcheting, which indicates that this loading waveform may not be suitable for producing creep-dominant creep-fatigue interaction data. Thus, this loading profile has similar limitations as purely stress-controlled testing.

3.3 RESULTS AND DISCUSSION

A summary of different types of loading profiles is shown in Table 2.1, each with their unique pros and cons. Some tests are fully strain-reversed and some are fully stress-reversed. For the objective of this study, the hybrid control test with intermediate stress hold (either for a constant time or to a constant strain) is considered to be the optimal testing procedure due to: 1) its flexibility in generating the full range of test runs with varying contributions of creep and fatigue damage by changing the creep holding stress, hold time (or creep strain) and fatigue strain range; 2) absence of ratcheting damage; 3) its creep holding stress being less than the yield stress which is a realistic loading state for the power plant.

Testing profiles	Fully reversed strain	Fully reversed stress	Cyclic ratcheting	Creep-Fatigue Interaction	Comments
Purely strain-control with stress relaxation	Yes	No	No	Fatigue-dominant only	
Purely force-control	No	Yes	Yes	Creep-dominant only	
Hybrid-control with stress hold at peak strain	Yes	No	Yes	Creep-dominant only	Creep power law breakdown; not representative of operating conditions
Hybrid-control with intermediate stress hold	Yes	No	No	Full range of creep fatigue contributions	More representative of operating conditions
Hybrid control with ratcheting and intermediate stress hold	No	Yes	Yes	Creep-dominant only	Large ratcheting damage in addition to creep/fatigue

Table. 3.1 – Comparison of creep-fatigue loading waveforms and their capacity to generate the full range of creep-fatigue interaction.

Thus, additional tests were performed using the hybrid-control loading waveform with a hold at intermediate stress. The test results are summarized in Table 3.2. Creep damage fractions were calculated using the time fraction approach and fatigue damage fractions were calculated as cycle fractions as shown in Eq. 1.

#	Fatigue Strain Range %	Fatigue Stress Range MPa	Holding Stress MPa	Hold Time s	Creep Strain %	Cycles to Failure	Comments
1	0.80	-	85	10	-	1145	Fixed Hold Time
2	0.80	-	85	120	-	200	
3	0.80	-	85	150	-	150	
4	0.80	-	85	180	-	180	
5	0.80	-	85	900	-	33	
6	0.60	-	100	900	-	12	
7	0.60	-	100	180	-	94	
8	0.60	-	100	30	-	480	
9	0.80	-	85	-	0.20	850	Fixed Creep Strain
10	0.80	-	85	-	0.30	560	
11	0.80	-	70	-	0.20	600	
12	0.80	-	70	-	0.30	340	
13	1.00	-	85	-	0.20	630	
14	1.00	-	85	-	0.30	450	
15	-	80	40	30	-	15000	Force-Controlled Tests
16	-	110	55	30	-	7886	
17	-	140	70	30	-	1470	
18	0.90	-	Peak	-	0.30	690	Hold at Peak Strain
19	0.80	-	85	-	0.20	251	Ratcheting by 0.2%
20	0.80	-	-	-	-	1670	Pure Fatigue
21	-	-	85	-	-	11200s	Pure Creep

Table 3.2 – Summary of test results

The results are presented on creep-fatigue interaction diagram in Fig. 3.7. In traditional strain-controlled creep-fatigue testing for Alloy 617, the fatigue damage fraction (usually between 0.3 and 0.7) is larger than the creep fraction (usually in the range of 0-0.2). For the proposed testing profiles, the results are very different. The tests have large creep fraction (ranging from 1.5 to 4.5) and a relatively small fatigue fraction

(mostly falling between 0 and 0.5). A creep fraction larger than unity has been reported in the literature for steels [14,21,22]. It is also interesting to note that, using the new testing profiles, creep fraction does not increase monotonically with increasing hold time. This contradicts the common expectation that a longer hold time will lead to higher creep damage fraction. The absence of a clear trend combined with large values of creep fraction mean that damage summation and time fraction approach are not sufficient for creep-fatigue life prediction for this new loading profile. A detailed explanation requires further experiments and analysis. The authors suspect this phenomena is due to the following reasons: (i) existing life prediction models with time fraction approach are more suitable for strain-controlled loading waveforms; (ii) creep-fatigue interaction is strongly dependent on the type of loading waveform used [21] so different loading waveforms may follow different interaction curves; (iii) the definition of creep damage fraction as a ratio of cyclic hold time and creep rupture time is not appropriate since creep strain in creep-fatigue tests does not accumulate monotonically (i.e., in the case of creep rupture testing) with cycles due to the strain reversal. The above statements would imply that a new life-prediction methodology must be proposed to accurately predict life for both strain-controlled and hybrid-controlled loading profiles.

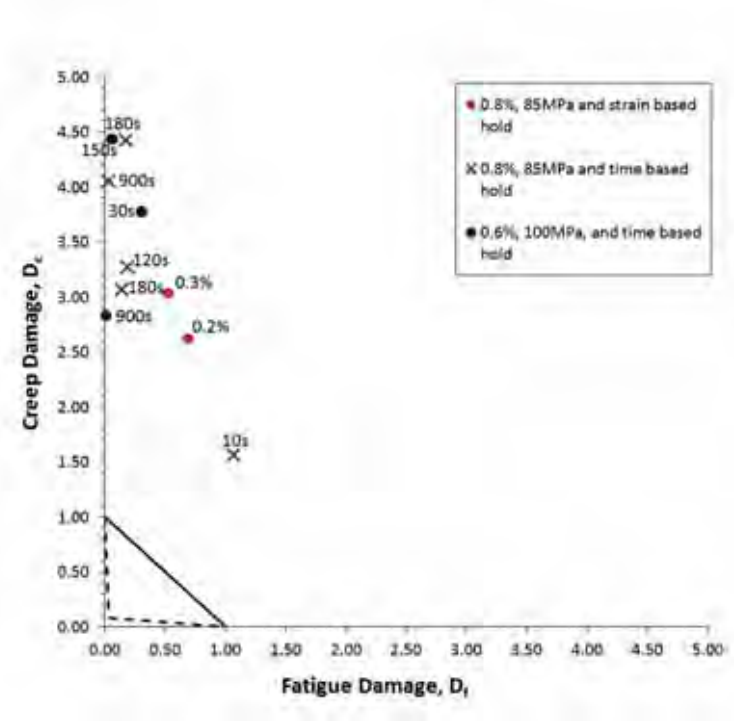

Fig. 3.7 – Creep-fatigue damage interaction diagram for hybrid-control tests with hold at intermediate stress.

3.4 CONCLUSION

A new testing profile for generating creep-dominant creep-fatigue interaction is proposed in this paper and it is fundamentally different from the traditional strain-controlled fatigue-stress relaxation tests. The major conclusions from this experimental study are:

- Pure force-controlled tests only produced extremely ‘creep-dominant’ interaction for Alloy 617 at 950°C and did not produce data in the regime of creep-fatigue interaction;

- When Alloy 617 was subjected to novel loading waveforms - with a combination of force and strain control at 950°C, the creep damage fraction as estimated by the time fraction rule was greater than unity;
- Experimental results from the new loading profiles did not show clear and monotonic trends on the creep-fatigue damage interaction diagram;
- Classical creep-fatigue life prediction models are based on strain-controlled tests and cannot be extended to non-standard loading waveforms.

The damage interaction diagram based on time fraction rule - currently suggested by Boiler and Pressure Vessel Code [23] – is not valid for creep-fatigue life prediction under unconventional loading waveforms. Hence, further experiments and analytical study are required to develop a new creep-fatigue damage interaction diagram for design purposes. The new diagram must work for the proposed loading waveforms as well as the traditional strain-controlled testing. Moreover, a mechanism investigation of microstructural damage evolution may be conducted to reveal any correlations between local damage features and the applied loading waveforms. A life prediction model which utilizes a damage interaction diagram based on micro-scale damage evolution mechanisms will be valuable for a complete understanding of the proposed testing profiles and creep-fatigue failure of Alloy 617 at elevated temperatures.

4. IMAGE-BASED CREEP-FATIGUE DAMAGE MECHANISM INVESTIGATION

4.1 INTRODUCTION

Creep-fatigue interaction can be explained microstructurally as a combined effect of creep and fatigue damage, where creep mainly produces internal voids while fatigue generates surface cracks [1]. Alloy 617 contains M_6C and $M_{23}C_6$ type carbides, where $Cr_{23}C_6$ constitutes a large portion of the grain boundary and twin boundary precipitates [24]. These precipitates provide creep resistance by preventing grain boundary sliding, and they also act as void nucleation sites. Under creep-fatigue conditions, multiple voids initiate and coalesce along the grain boundaries and eventually interact with surface cracks to accelerate intergranular crack growth [16]. Alloy 617 is also known to form a layer of Cr_2O_3 on the surface of test specimens in air at elevated temperatures and the thickness of this oxide layer is a function of time and temperature [25]. Underneath the surface oxide layer is a sub-layer consisting mainly of Al_2O_3 precipitates [8] and a decarburized region due to the oxidation of chromium carbides [26]. Surface cracks are typically flanked by a Cr rich oxide layer [7]. Dynamic recrystallization[25] and precipitate redistribution[27] have also been studied for Alloy 617 at temperatures of 800-1000°C. Studies on microstructural damage induced in Alloy 617 under strain-controlled creep-fatigue loading at 950°C observe large amounts of grain-boundary cracking but negligible cavitation, especially for longer hold times [8,16]. The absence of creep voids coupled with internal grain boundary cracking [8] indicates that purely strain-controlled loading causes fatigue-dominated failure for Alloy 617 at 950°C. This can be explained

by rapid stress relaxation of Alloy 617 at high temperatures which implies that increasing hold time will not increase the creep damage fraction in the strain-controlled testing [6,7]. This study employs a loading profile with force-controlled hold periods [28] to generate a larger proportion of creep damage, thereby allowing tests to cover the entire range from fatigue dominated to creep dominated failure.

Fatigue life at elevated temperatures is influenced by strain rate, hold time, type of hold – stress or strain, and type of loading waveform [1,21]. Existing creep-fatigue design curves for Alloy 617 are derived from tests with strain-controlled loading profiles [7,9]. These design curves are based on damage summation rule using the time fraction approach, which is inadequate for life prediction of Alloy 617, regardless of the loading profile (i.e. strain-controlled or force-controlled hold periods) [6,28]. Moreover, the widely used damage diagram (D-diagram) is a phenomenological representation of macro level testing data. An accurate D-diagram should be directly supported by the underlying microstructural damage mechanisms, which is currently lacking in the open literature. Thus, there is a need for a creep-fatigue life prediction methodology that is informed by an analysis of microstructural damage features. The objective of this study is to qualitatively and quantitatively investigate the microstructural failure mechanisms using imaging analysis. The imaging analysis results are compared with the macro-level loading parameters, both from classical creep-fatigue damage summation rule suggested by the ASME Boiler and Pressure Vessel Code [9] and a newly proposed approach based on correlational analysis.

The paper is organized as follows. First, the experimental testing procedure for the new testing profile is discussed along with testing matrix, and specimen preparation. Next, qualitative imaging interpretation is given for the damage features observed and their relationship with loading conditions. A quantitative statistical analysis is performed to extract the fatigue crack length distribution and interval void density distribution information. The statistical information is then compared with the classical time fraction approach for life prediction suggested in ASME codes. Following this, the same testing procedure is applied to a set of interrupted test specimens and time-dependent micro-scale damage evolution is investigated. Finally, some conclusions and future work are drawn based on the proposed study.

4.2 EXPERIMENTAL TESTING AND IMAGING ANALYSIS

4.2.1 Testing Setup and Procedure

Creep-fatigue tests were carried out on a servo-hydraulic load frame equipped with a three-zone furnace. Furnace temperature was maintained at 950°C for the duration of each test. The test specimens had a circular cross-section, button-head ends, and tangentially blended fillets between the test section and ends, in accordance with ASTM 2714-13. The specimen had a gage length of 20mm and reduced section diameter of 7.5mm. The temperature difference along the gage length was maintained below 10°C with the aid of four thermocouples wrapped on to the specimen. Strain was measured by an extensometer with ceramic extension rods that remained in contact with the specimen during the test.

The loading profile for the tests was different from the classical strain-controlled stress relaxation testing. Fig. 4.1 shows the creep-fatigue loading waveform [28] that was used for the tests. The ramps are strain-controlled at a constant rate of $1x10^{-3}$/s, whereas the hold is force-controlled. Combinations of fatigue strain range, holding stress, and hold time were applied to generate varying proportions of creep and fatigue damage. In this study, the testing matrix was designed by varying the fatigue strain range (0.6% and 0.8%), holding stress (85 MPa and 100 MPa), and holding time (30 s, 180 s and 900 s).

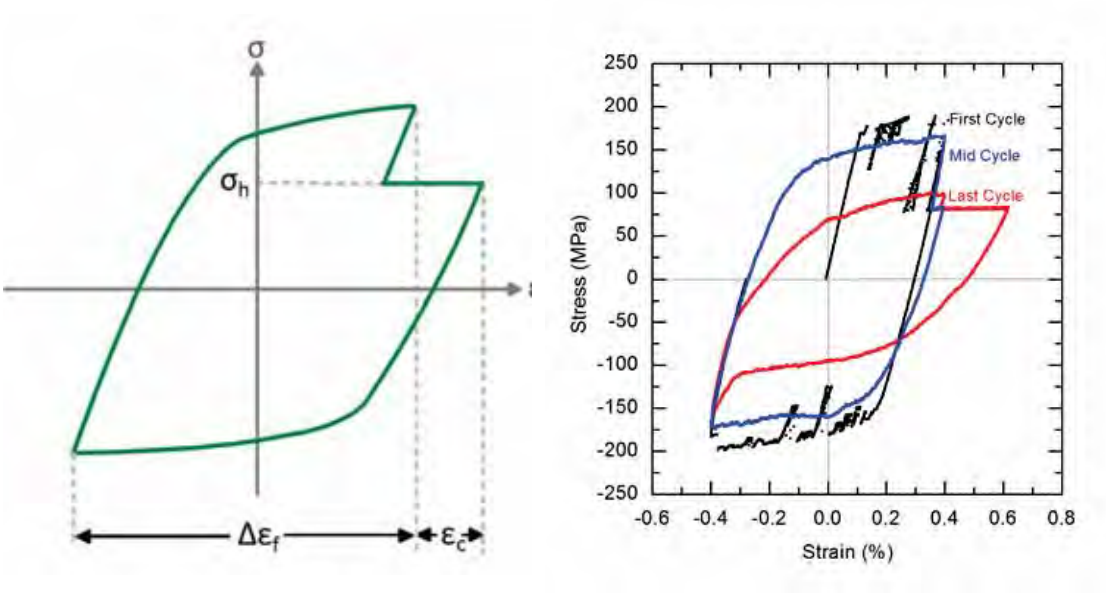

Fig. 4.1 – (a) A schematic of the loading waveform; (b) Loading waveform for first, mid and last cycle for a test with 0.8% fatigue strain range and a 10s hold at 85 MPa;

Ruptured test specimens were split in half along the longitudinal axis using Electric Discharge Machining (EDM). The flat side of the sectioned specimens was initially ground with silicon carbide grit papers ranging from 240 to 1200 grit and subsequently polished with 1 micron polycrystalline diamond suspension on a polishing

pad. The specimens were then examined under Scanning Electron Microscope (SEM) to obtain qualitative and quantitative information about creep-fatigue damage.

4.2.2 Qualitative Image Analysis for Mechanism Investigation

Qualitative image analysis of failure patterns, microstructural damage features, grain structures, and elemental analysis were performed. The failure surfaces were investigated first. There are generally two distinct failure patterns observed in the test specimens. One pattern is associated with significant necking and cup-shape failure surface. The failure surface is very rough indicating ductile rupture. This failure pattern usually occurs with longer hold time and lower fatigue cycles. Another pattern is associated with less necking and relatively flat failure surface. The fracture surface is relatively smooth and shows classical failure characteristics of brittle fatigue fracture. This failure pattern usually occurs with shorter hold time and higher fatigue cycles. Fig. 4.2 shows tests specimens with the abovementioned failure patterns. This observation strongly suggests that there are at least two failure modes in this testing: one is creep rupture-dominated and the other is fatigue fracture-dominated.

(a) (b) (c)

Fig. 4.2 – Optical images of the sectioned test specimens for 0.8% fatigue strain range and 85 MPa holding stress with (a) 30 s holding time; (b) 180 s holding time; (c) 900 s holding time.

Following this, the SEM images for all failure specimens are taken and observations focused on the internal voids and surface cracks. The representative results are shown below with respect to different holding time. Fig. 4.3 shows the 900 s hold time test resulted in creep dominated failure as evidenced by large voids which showed signs of coalescence. Surface cracks are shorter and tend to link with the sub-surface voids (Figs. 4.3(a) and 4.3(b)). Many internal voids are initiated and are linked together to eventually break the specimen. Fig. 4.4 shows the 180 s hold time test which also produced both voids and cracks, but there was minimal interaction between them. The average crack length is longer than that observed for 900 s hold and the average void density is smaller than that observed in 900 s hold (quantitative statistical analysis will be shown later). Fig. 4.5 shows the 30s hold time test, which resulted in fatigue dominated failure indicated by the long surface cracks, some internal cracks and no voids (or the

voids are smaller than the current resolution allows i.e. diameter > 1~2 μm). The long surface cracks appear to show a mix of inter-granular and trans-granular crack growth. In general, the surface cracks become more straight and perpendicular to the applied loading direction in 900 s hold test than that in the 30 s hold test (see Figs. 4.3-4.5). This observation suggests that the fatigue crack propagation tends to be more trans-granular when the holding time decreased. This can be explained by the weakening of grain boundaries by the creep voids. As most internal voids lie on the grain boundaries, significant creep damage will make the fatigue crack propagate along the weakened grain boundaries. If the grain boundary is not weakened significantly (i.e., lower hold time and creep damage), the fatigue crack will propagate as trans-granular cracks.

The crack surfaces were oxidized (see Fig. 4.5(c) and 6(d)) which is due to the long exposure time of fatigue crack surfaces under high temperature conditions. EDS results will be shown later to confirm the oxidization by elemental analysis. Grain boundary cracks in the interior of the specimen were only observed in fatigue dominated case and it is known that strain-controlled creep-fatigue testing on Alloy 617 at 950°C tends to generate interior grain boundary cracks instead of large voids [8]. This implies that most strain-controlled creep-fatigue tests lie in the fatigue dominated failure regime.

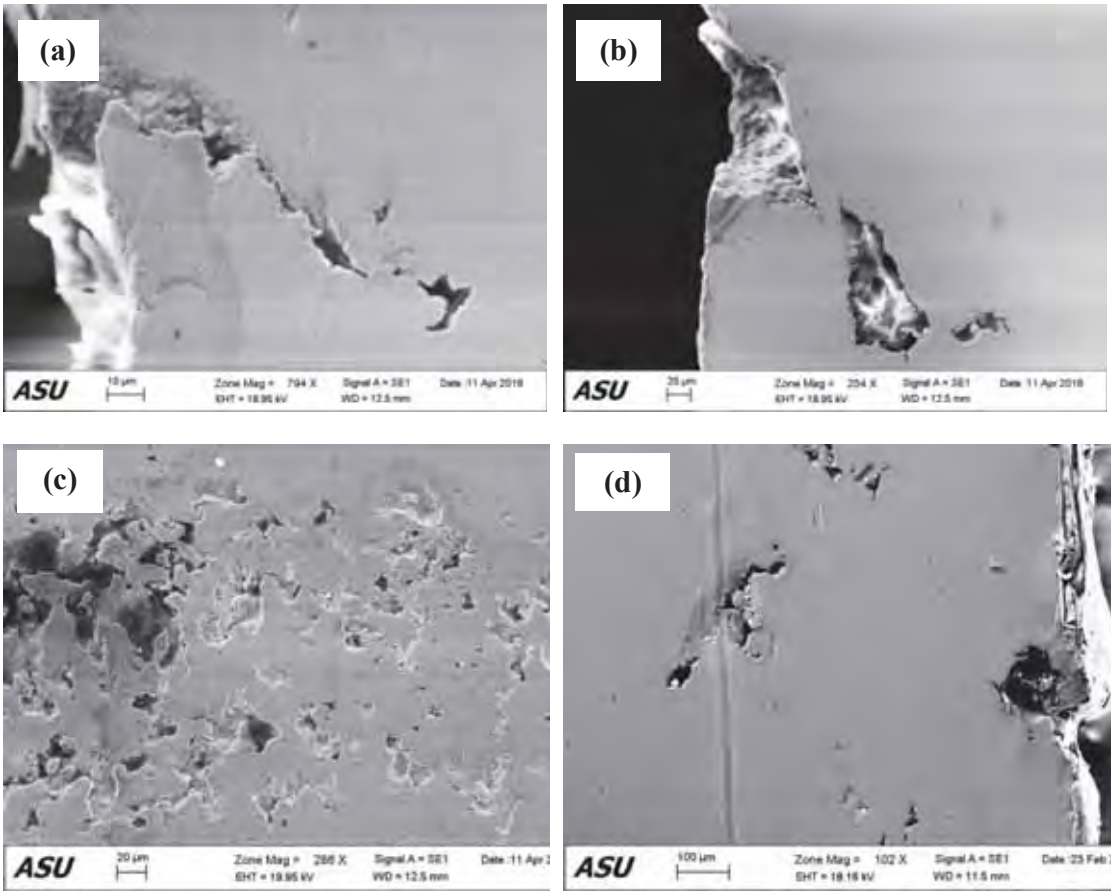

Fig. 4.3 – Test specimen with creep dominated failure (i.e. 900 s hold) shows (a), (b) linkage of surface cracks with sub-surface voids; (c) , (d) extensive void coalescence near fracture surface.

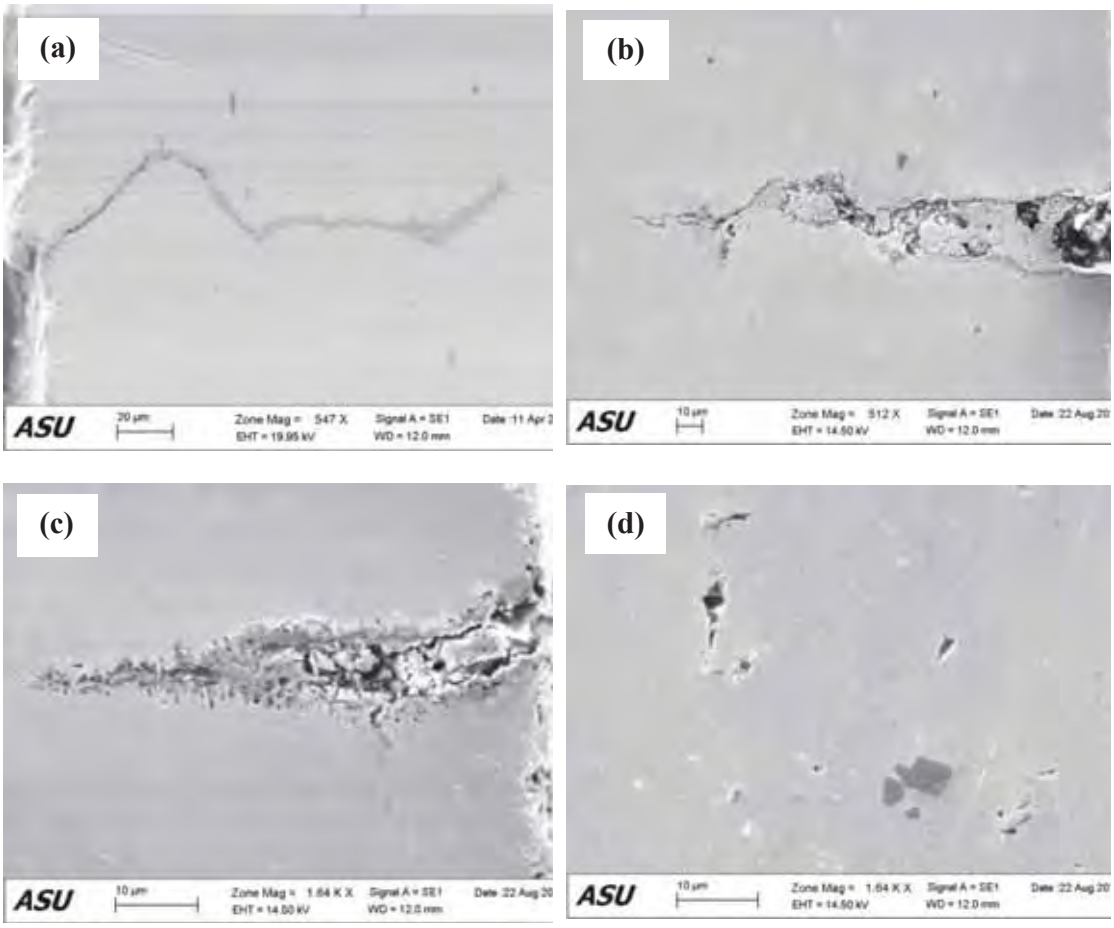

Fig. 4.4 – Test specimen with creep-fatigue interaction failure (i.e. 180 s hold) shows (a) mixed inter- and trans-granular crack growth (b), (c) transgranular cracks and (d) voids concentrated near the specimen surface.

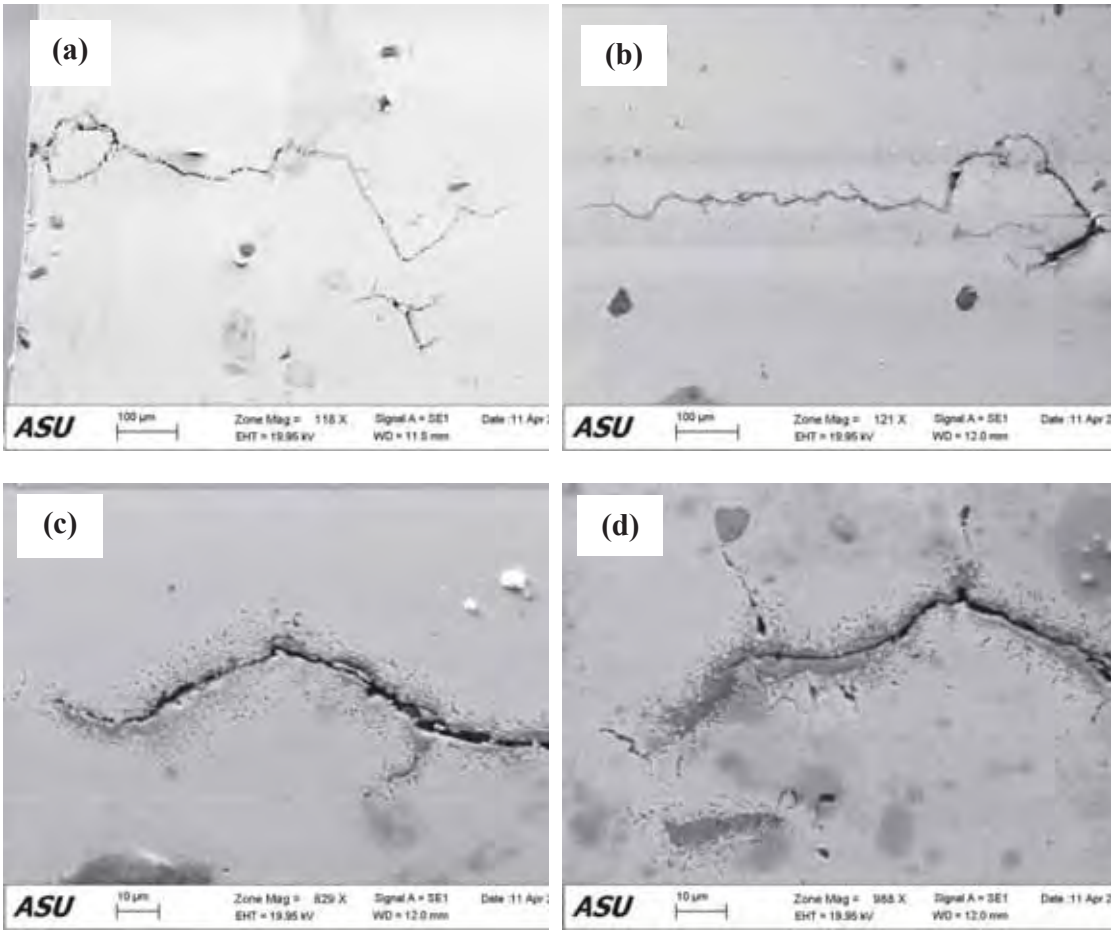

Fig. 4.5 – Test specimen with fatigue dominated failure (i.e. 30 s hold) shows (a), (b) long intergranular cracks; (c), (d) thin o layer flanking the cracks and grain boundaries ahead of the crack tip.

Next, Electron Backscatter Diffraction (EBSD) was used on a specimen with creep dominated failure to identify the grain structure with respect to damage. It is observed that most internal voids are on the grain boundaries. An example is shown in Fig. 4.6. SEM images were obtained to identify the region of interest (ROI) with voids. The EBSD images for the ROI were then compared / overlapped with the SEM images. It is clear that the voids were generated at the grain boundaries (GB), especially near triple

junctions and GBs with high misorientation angles. The voids tend to grow along the GB and link with the neighboring GB voids.

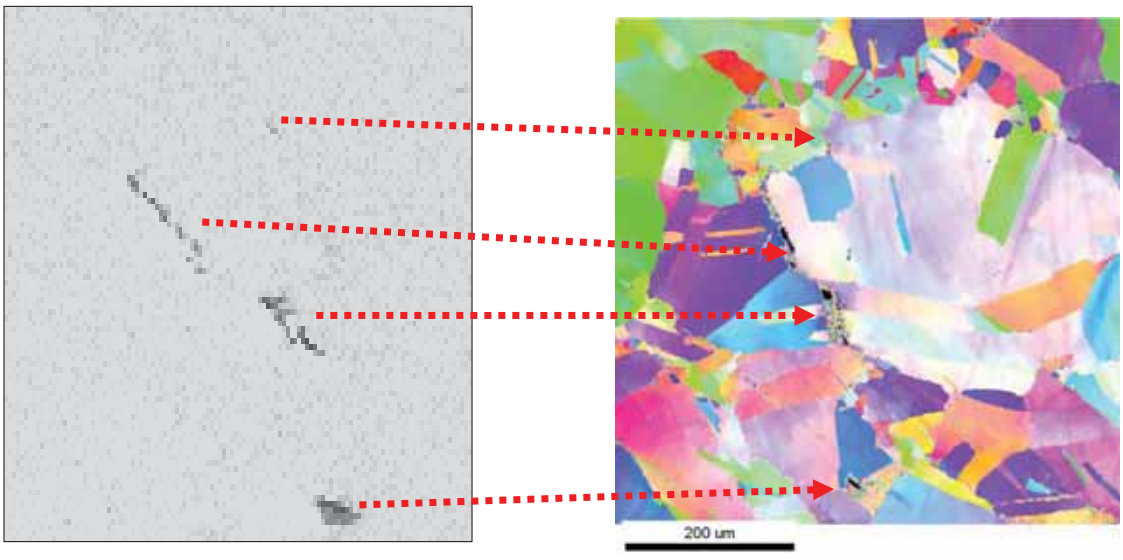

Fig. 4.6 – SEM and EBSD imaging for internal voids of failed specimen

Following this, Energy Dispersive Spectroscopy (EDS) was used to identify the elements near the fatigue cracks. Fig. 4.7 show an EDS phase map for a test specimen with 0.6% fatigue strain range, 100 MPa holding stress, and 30 s hold time. This condition represents fatigue dominated failure for current loading profile. The crack surfaces were flanked by an external layer of chromium oxide and an internal layer of aluminum oxide. The precipitates were titanium nitride. In contrast to the fatigue dominated test specimen, the creep dominated specimen showed blunt cracks with no oxidation layer. This indicates that creep dominated specimens developed surface cracks near the end of the cycle life, whereas fatigue dominated specimens developed surface

cracks early on, allowing sufficient time for the exposed surfaces to oxidize. The EDS composition map is shown in Fig. 4.7.

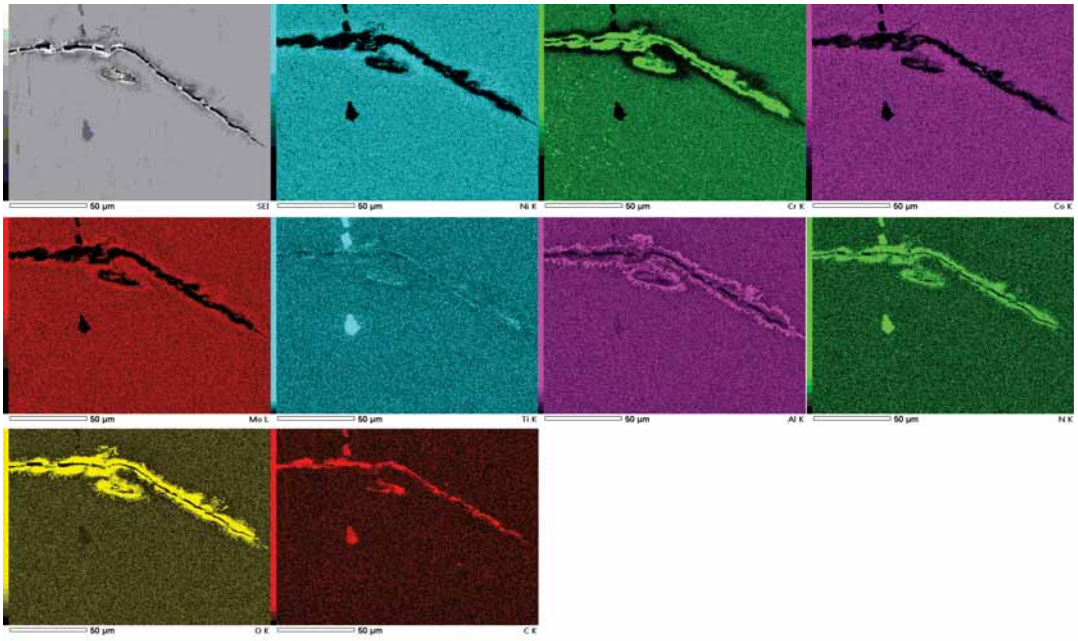

Fig. 4.7 – EDS phase maps for surface crack on a test specimen with fatigue dominated failure

Fig. 4.8 compares the relation between cycle life and hold time for hybrid-control and strain control tests. In traditional strain-controlled creep-fatigue tests, increasing the hold time does not lead to increase in creep damage, due to rapid stress relaxation of Alloy 617, as shown in Fig. 4.8(b). However, hybrid-control tests show a reduction in cycle life with increase in hold time, as shown in Fig. 4.8(a). Generating creep dominated damage is one of the main advantages of using a hybrid-control loading profile. Micro-scale image analysis provides physical evidence for this behavior. Specimens undergoing hybrid-control loading show that longer hold time does leads to more creep damage as

characterized by void initiation and coalescence at grain boundaries whereas shorter hold time leads to fatigue dominated damage as represented by oxidation-assisted crack growth at exposed outer surfaces.

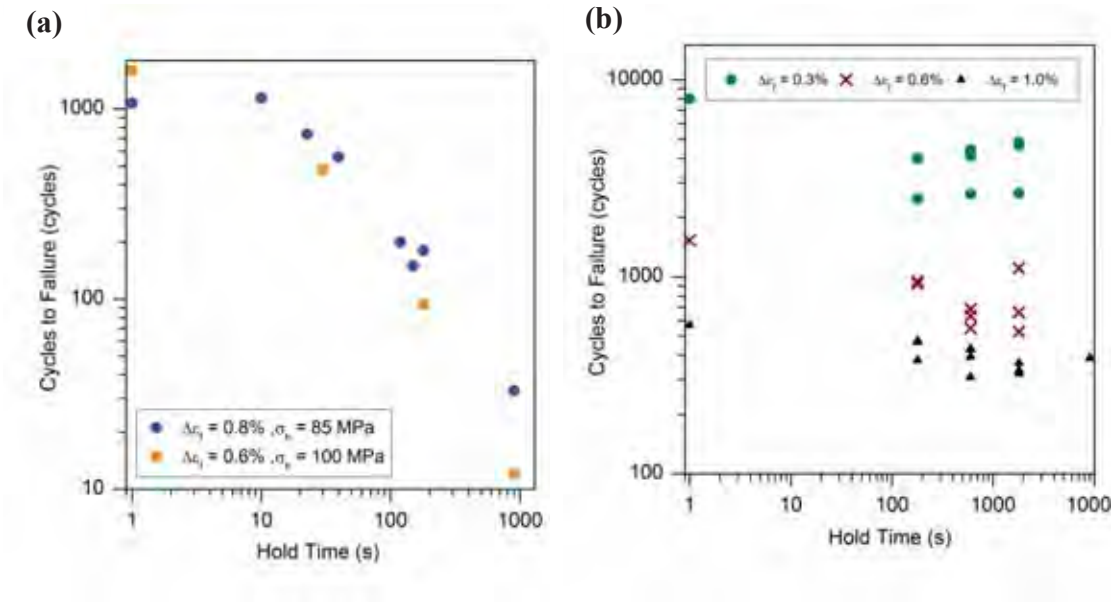

Fig. 4.8 – Relation between cycle life and hold time for (a) hybrid-control tests; (b) strain-control tests [29].

4.2.3 Digital imaging measurements and statistical data analysis

Above discussion was interpretation of imaging for experimental observations of a new testing profile that is capable of producing creep dominated failure. It provides insights into the damage mechanisms involved, but does not provide quantitative measurements for future life prediction models and design curves. Thus, this section focuses on digital imaging measurements and statistical data analysis to achieve this goal.

The focus is on the following metrics: surface crack length, number of voids, and void area / area fraction.

The new hybrid-control creep-fatigue tests covering a range of creep and fatigue fractions were used for image-based damage analysis in SEM. The length of each surface crack along the gage length of the specimen was measured in SEM to provide an estimate of fatigue damage. Fig. 4.9 shows the tail of an empirical cumulative distribution function of the crack lengths from three tests with a fatigue strain range of 0.6%, a holding stress of 100 MPa and hold times of 30, 180, and 900s, respectively. The distribution of crack lengths less than 200μm was almost identical for the three tests. However, the 10% percentile curves for cracks with lengths greater than 200μm showed significant differences between creep dominated and fatigue dominated failure modes. In this case, 30s hold time represents fatigue dominated failure whereas a 900s hold time represents a creep dominated failure. The fatigue dominated case has much longer crack lengths compared to the creep dominated case. It should be noted that the mean crack length is not compared here as the failure is an extreme event and only the tail region (i.e., longest cracks in the specimen) affect the final failure. In the current investigation, the longest crack observed in the fatigue dominated specimen is about 10 times the length of the longest crack in the creep dominated case. The mean and standard deviation of the measured cracks are shown in Table. 4.1. It is observed that, not only the mean crack length, but also the standard deviation of the crack length increases as the hold time decreases.

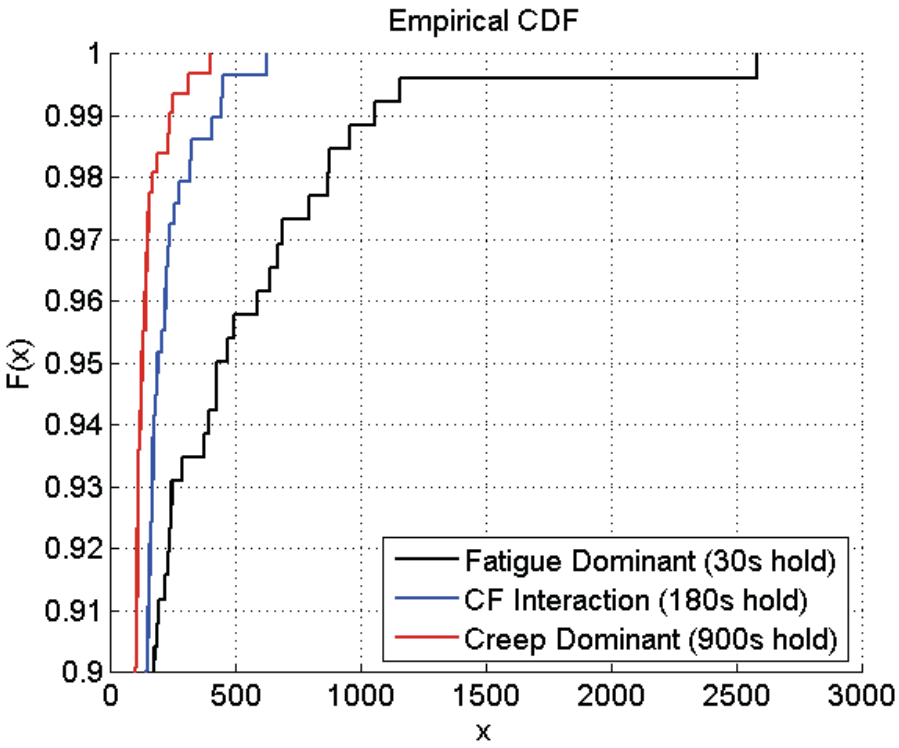

Fig. 4.9 – Empirical cumulative distribution function (F(x)) for length of surface cracks (x) during creep-fatigue tests with varying hold time

Hold Time, s	**Mean Crack Length (μm)**	**Standard Deviation (μm)**
30	94.05	230.62
180	69.06	76.30
900	51.59	47.80

Table. 4.1 – Mean crack length and standard deviation corresponding to different hold times

The next digital measurements were for the internal voids. Multiple SEM images were captured across the width of the specimen at distances of 1mm, 3mm and 5mm from the rupture surface, as shown in Fig. 4.10. The reason is that the internal void distribution is not uniform across the length of the specimen. Image analysis was performed to determine the ratio of area covered by voids to the total area in the image. This void area fraction was used as an indicator of creep damage in the sample. Fig. 4.10 summarizes the void damage in a test specimen with creep dominated failure i.e. 0.6% fatigue strain range, 100 MPa holding stress, and 900 s hold time. The results of image analysis for this particular sample are shown in Table 3.2. The area fraction of voids and average void size was highest near the rupture surface but the number of voids was lowest, indicating that final failure was caused by void coalescence. Only voids larger than 1 μm were analyzed. A similar analysis was performed on the fatigue dominated test specimen with 30 s hold time and creep-fatigue interaction test specimen with 180s hold time. No voids larger than 1 μm were detected on the fatigue dominated test specimen with 30 s hold time. For the creep-fatigue interaction specimen, voids were present but their average size and area fraction was less than the creep dominated specimen.

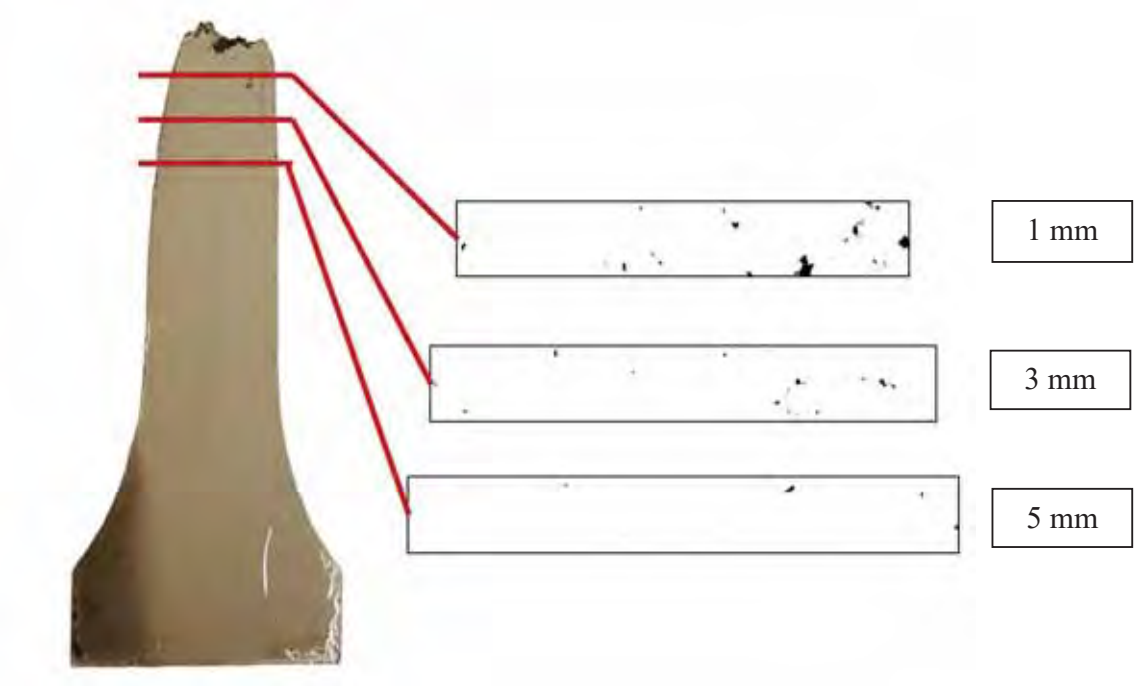

Fig. 4.10 – Analysis of voids on a sectioned half of the ruptured test specimen

Distance from Fracture Surface, mm	No. of Voids	Average Void Size, μm^2	Area Fraction of Voids, %
1 mm	56	1135.88	1.492
3 mm	86	206.96	0.373
5 mm	100	104.24	0.207

Table. 4.2 – Variation in number, size and area fraction for voids at fixed distances from the rupture surface

4.3 CORRELATIONAL ANALYSIS FOR IMAGING MEASUREMENT AND MECHANICAL DAMAGE PARAMETERS

As mentioned in the introduction, one benefit for the rigorous quantitative imaging analysis is that it can provide a statistical correlation with the external damage parameters. Thus, the micro-scale damage features and macro-level damage parameters can be linked. This section focuses on this objective. For the micro-scale damage features, the crack length and void area fraction are selected. For the macro-level damage model, the widely used ASME damage summation rule with time fraction approach is applied. The damage parameters are fatigue fraction (i.e., number of cycles to failure in creep-fatigue testing normalized by the corresponding pure fatigue failure cycles) and creep fraction (summation of hold time normalized by the creep rupture time). It is expected that, if the model is correct, a correlation between the micro-scale features and damage parameters can be identified. The following analyses are done for fatigue and creep correlation, respectively.

If fatigue damage is considered as initiation and propagation of surface cracks and creep damage is considered as initiation, growth, and linkage of voids, then creep-fatigue interaction diagram based on these damage features can provide useful insights for the purpose of developing microstructure-informed creep-fatigue life prediction models. Tests were performed with varying fatigue strain range, holding stress, hold time, and type of hold to generate creep-fatigue interaction. The type of hold refers to whether the force-controlled hold during each cycle was for a fixed time period or up to a fixed strain value. Fig. 4.11 shows a significant variation in crack lengths across different tests for

cracks longer than 200μm. Specimens with larger fatigue damage fraction have longer cracks indicating that crack growth is the primary damage mechanism for fatigue dominated failure. This hypothesis is further supported by the linear increase in mean and standard deviation of crack lengths with increasing fatigue damage fraction, as shown in Fig. 4.12. The fatigue damage fraction was slightly larger than unity for the 10s hold test. This implies that a 10s hold time test is similar to a pure fatigue test and that the 10s hold is not enough to induce creep damage. It is interesting to note that the test with force-controlled hold up to a fixed strain (green circle in plot) does not show significant variation from the linear trend of mean and standard deviation of crack lengths. This analysis indicates that the fatigue fraction is a good candidate for the development of creep-fatigue models as it closely related to the micro-scale damage (crack length and its variance).

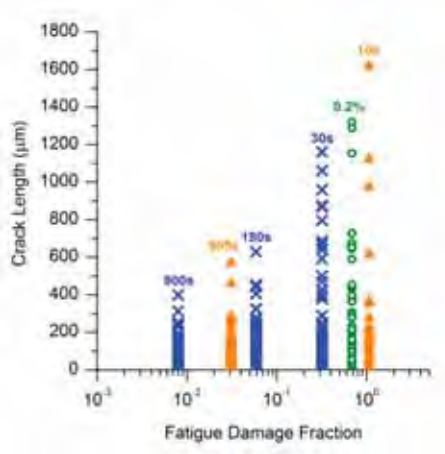

	Fatigue Strain Range (%)	Holding Stress (MPa)	Type of Hold
X	0.6	100	time
▲	0.8	85	time
O	0.8	85	strain limit

Fig. 4.11 – Variation in distribution of crack lengths with fatigue damage fraction. Error bars represent standard deviation.

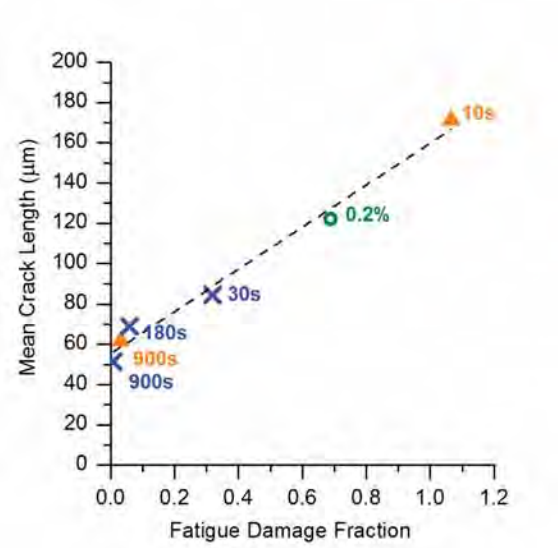

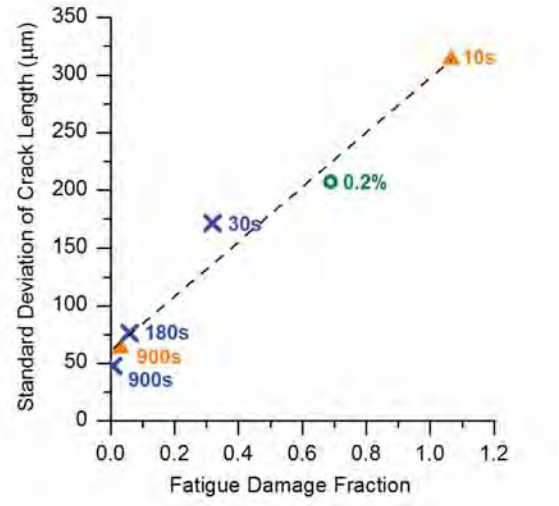

	Fatigue Strain Range (%)	Holding Stress (MPa)	Type of Hold
X	0.6	100	time
▲	0.8	85	time
O	0.8	85	strain limit

Fig. 4.12 – Mean and standard deviation of crack length increase with increasing fatigue damage fraction

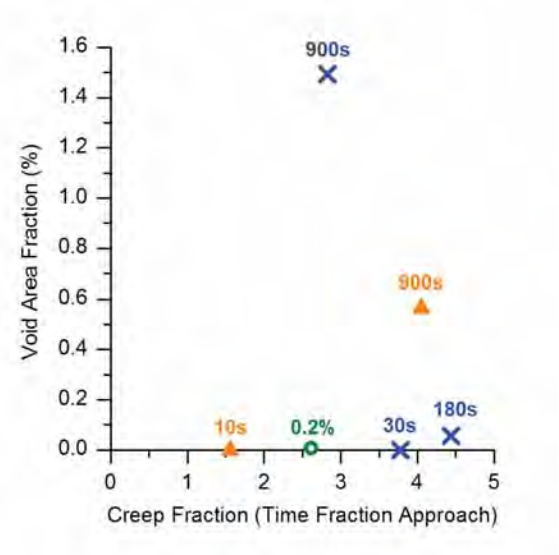

Fig. 4.13 – Relation between void area fraction 1mm below the rupture surface and creep damage fraction using time fraction approach

Next, the correlation is done for the internal void area fraction and creep time fraction. Since the internal voids are not uniformly distributed across the specimen length, the void area fraction was calculated at 1mm distance from the rupture surface, as described in the previous section. Fig. 4.13 illustrates that there is no relation between void area fraction and creep damage fraction calculated using the classical time fraction approach. It is also interesting to note that the 900 s hold (blue circle) has less “creep damage fraction” compared to the 30 s and 180 s hold. This is contrary to expectation and evidence provided by imaging analysis described earlier. This suggests that the widely used time fraction approach for calculation of creep damage is not a good candidate for

the creep-fatigue life prediction as it does not correlate well with the damage features; in particular the void area fraction.

Creep-fatigue interaction in steels is traditionally represented by a bilinear trend curve on an interaction diagram that is based on linear damage summation rule and time fraction approach[21,30]. Fatigue damage is represented as a cycle fraction and creep damage is represented as time fraction. Although, the time fraction approach is employed in nuclear component design codes, namely, ASME BPVC Section III Subsection NH[9] and RCC-MR[11], this approach has several limitations[19,31]. Moreover, elevated temperature strain controlled testing of Alloy 617 fails to produce a clear trend on an interaction diagram due to irregular values of creep damage fraction [5,28]. Further theoretical and experimental study is required to find another parameter that is best correlated with the observed internal voids. The current study only investigates a simple alternative mechanical parameter, called effective creep time fraction. The basic idea is briefly discussed here. For the investigated hybrid control loading profile, the total creep strain will monotonically increase from cycle to cycle due to the softening. Thus, the hold time can be divided into two parts: one part is to recover the creep strain happens in the previous cycle and the other part is to increase the creep strain to a new high level. The second part is referred to as the effective hold time and it indicates the time is “effective” in causing monotonic creep strain increment. The summation of this part of hold time for all cycles can be normalized by the creep rupture time and is defined as the effective creep fraction. Fig. 4.14 shows that the observed internal void area fraction has a very good correlation with the effective time fraction definition. It also shows that the creep

damage fraction increases as the hold time increases unlike the contradictory results from the classical time fraction approach.

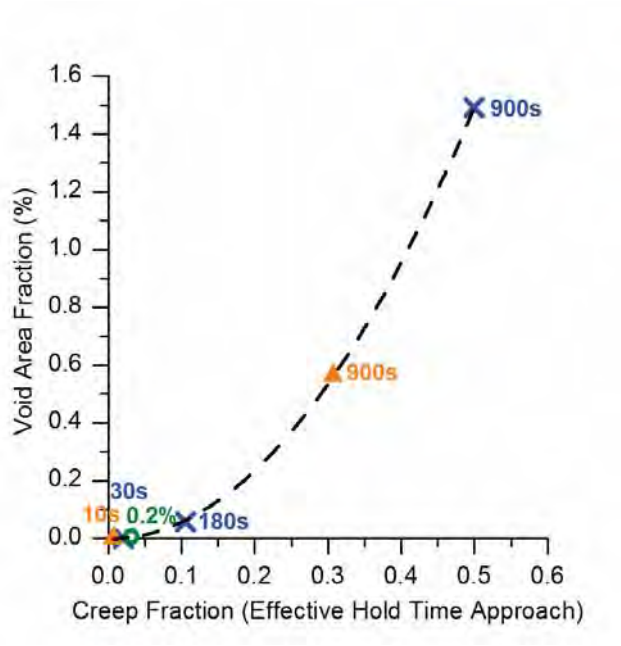

Fig. 4.14 – Correlation between void area fraction and effective hold time creep fraction

Another way to represent the correlational analysis is shown below using the concept of the D diagram. In the D diagram, x-axis represents the fatigue damage and y-axis represents the creep damage. Fig. 4.15 (a) constructs the "D" diagram using the microstructurally observed crack length and void area fraction. Both mean and 90% quantile curves are shown. The micro-scale imaging analysis gives a clear bilinear trend, representing the two distinct failure modes, i.e., creep dominated and fatigue dominated. Fig. 4.15 (b) shows that D diagram using the damage parameters: fatigue fraction and the effective creep fraction. The trend is very similar to the micro-scale imaging results as it also shows a clear bilinear trend. Thus, these two parameters may be used for future life

prediction model development as a strong correlation with microstructural damage features is obtained.

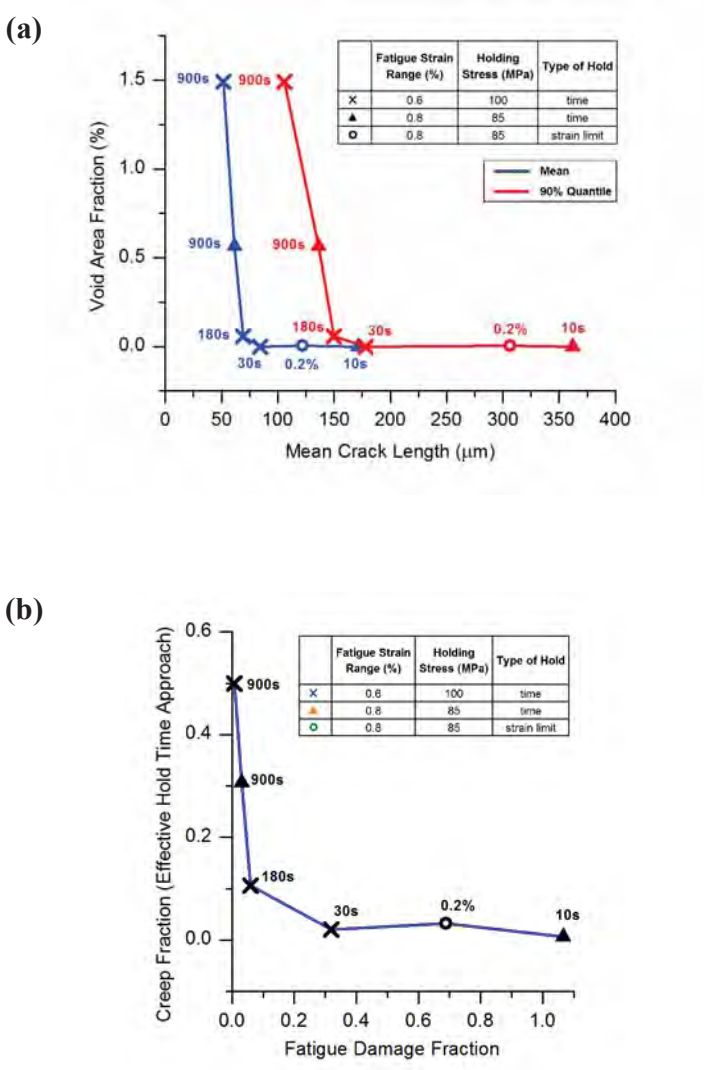

Fig. 4.15 –D diagram construction using micro-scale imaging results and damage parameters (a) Damage interaction diagram based on microstructure; (b) Damage interaction diagram based on effective hold time approach.

4.4 INTERRUPTED TESTING

Interrupted tests were conducted to investigate damage evolution. A creep-dominant creep-fatigue test with 0.6% fatigue strain range, 100 MPa holding stress and 900s hold time was selected for interrupted testing. An initial test was allowed to run till failure to determine the cycle life. The test was then repeated three times and stopped at 25%, 50%, and 75% of the cycle life respectively. Fig. 4.16 shows that the peak and valley stresses for the interrupted tests do not show a significant variation from the initial test.

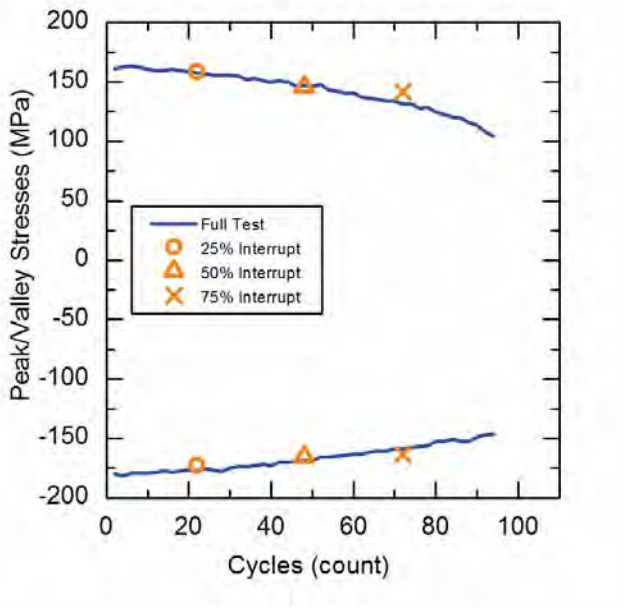

Fig. 4.16 – Peak and valley stresses for interrupted tests

The interrupted test specimens were sectioned along the gage length, polished, and observed under SEM. The length of each surface crack on the gage length was measured. A Kolmogorov-Smirnov test for goodness of fit indicated that a kernel distribution provided the best fit for the crack length data, as shown in Fig. 4.17. Table. 3.3 shows that

the mean crack length as well as the standard deviation of the crack lengths increases with cycles. The exponential increase in standard deviation during the first three quarters of the cycle life can be explained by the initiation of new cracks. The relatively smaller increase in standard deviation during the final quarter indicates that new cracks initiated at a slower rate during this period.

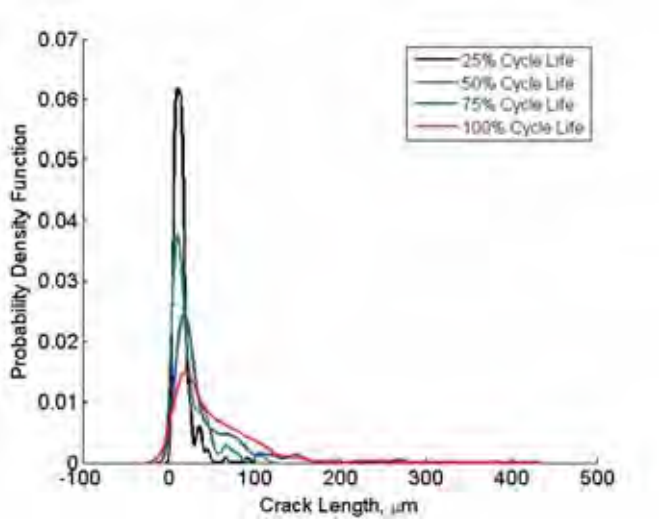

Fig. 4.17 – Probability density function of crack lengths at different interrupts

	Mean Crack Length, μm	Standard Deviation, μm
25% Cycle Life	15.40	10.30
50% Cycle Life	23.16	21.06
75% Cycle Life	43.54	44.25
100% Cycle Life	51.59	47.80

Table. 4.3 – Mean crack length and standard deviation at different interrupts

The total number of micro-voids on the gage section of the test specimen was much higher than the number of surface cracks and there was a significant variation in void damage along the gage length. Therefore, an accurate representation of void damage required capturing a large number of high-magnification images covering the entire gage length of the specimen. Since, such a task was beyond the scope of this study, the void damage was studied qualitatively by imaging localized regions of high void density on each specimen and comparing amongst the interrupted tests. Void density was found to be highest near the specimen surface. This can be attributed to oxidation on the surface of the test specimen and consequent decarburization of grain boundary carbides located near the surface. A large increase in mean void size and void area fraction was observed in the last quarter of the cycle life indicating that most of the void growth and coalescence occurred towards the end of the cycle life. This information combined with the crack length analysis shows that, for a creep-dominant test, the damage mechanism changes from crack initiation and growth to void growth and coalescence during the last quarter of the life.

4.5 CONCLUSION

Hybrid-control testing can generate creep dominated failure. Image-analysis confirms that, unlike the classical strain-controlled testing, the new hybrid control testing profile can increase the creep damage by increasing the hold time under force-control. Qualitative image analysis shows that there are two distinct failure modes in the investigated testing cases: ductile creep dominated failure with long hold time and brittle fatigue dominated failure with short hold time. The fatigue crack length correlates well with the cycle number ratios but the void area fraction does not correlate well with the

classical time fraction used by ASME code. An effective hold time approach (i.e. only considering the part of the hold time when net creep strain increase happens) correlates well with the observed void area fraction and provides an alternative way to formulate the damage interaction diagram. These conclusions currently apply to creep-fatigue interaction in Alloy 617 at 950˚C under force-controlled hold periods. A similar analysis can be performed on tests with strain-controlled hold periods, to confirm their inadequacy for generating significant creep damage. Further work may also include the development of a life prediction model, similar to the effective hold time approach, which mimics the bilinear damage curve obtained through micro-scale image analysis.

5. AN EFFECTIVE TIME FRACTION APPROACH FOR CREEP-FATIGUE LIFE PREDICTION

5.1 INTRODUCTION

Accurate life prediction and design methods are critical to ensuring structural integrity and reliability. Nuclear component design codes such ASME-NH [23], RCC-MR [11], and R5 Procedure [12] suggest linear summation of fatigue and creep damage for life prediction. ASME-NH and RCC-MR use a time fraction rule [18,32], where creep damage is represented by a time fraction whereas the R5 Procedure uses a ductility exhaustion concept [33,34], where creep damage is represented by a strain fraction. The parameter that controls creep damage in time fraction approach is stress whereas in ductility exhaustion it is inelastic strain [13,35]. Comparative studies on steels and alloys showed that the time fraction rule underestimates the creep damage leading to non-conservative prediction, whereas the ductility exhaustion approach overestimates the creep damage leading to over-conservative life prediction [13,35]. Another widely studied evaluation method is strain range partitioning [36], which divides the inelastic strain range into three components. This approach requires collecting considerable amount of hysteresis data with specialized loading waveforms [10]. Many other creep-fatigue evaluation methods are available in literature [10,13,31,35,37], but few are simple enough to be considered in design codes [38]. The focus of this study is the time fraction approach, which is preferred by design codes due to its simplicity. Thus, the discussions and comparisons in this paper are aimed at developing a more accurate time fraction approach.

The time fraction approach requires a complete set of creep-fatigue test data for calibration and validation. In open literature, most high temperature creep-fatigue tests are performed using strain-controlled loading waveforms (i.e., fixed strain during hold period leading to stress relaxation). For Alloy 617 at very high temperatures, the rapid stress relaxation generally leads to fatigue dominated damage and therefore makes it difficult to fully calibrate the damage diagram using the time fraction approach [6,13]. Thus, in the current study, a full range of creep-fatigue test data (i.e., both fatigue dominated and creep dominated) at 850°C and 950°C is collected through a newly developed hybrid-controlled loading profile with force-controlled hold periods [28]. Moreover, the experimental data, when plotted using the classical time fraction rule suggested by the draft code case for Alloy 617 [9], shows a significant scatter [39] and non-physical trends (e.g., values of creep damage fraction exceeding unity) [28]. The authors have performed extensive image-based damage analysis and correlational study using scanning electron microscopy of failed creep-fatigue test specimens [40]. It was observed that the microstructural damage features (e.g., microstructural void density) did not correlate with the classical time fraction calculation of creep damage. This observation suggests that other mechanical parameters should be explored to correlate with microstructural damage features and to predict the creep-fatigue life under such loading conditions.

In view of the above discussion, this paper proposes a new life prediction model for calculating creep damage in the particular case of Alloy 617 at temperatures above 850°C. The paper is organized as follows. First, the new experimental procedure for the

hybrid-control creep-fatigue loading [28] and the results of imaging analysis[40] are reviewed and discussed. New tests at 850°C are presented to demonstrate the effect of temperature on the proposed model. Following this, a detailed derivation of the proposed effective time fraction approach is provided for both hybrid-controlled and strain-controlled testing. A comparison with the classical time fraction approach is also given. Next, both in-house data for the hybrid-controlled testing and literature data for the strain-controlled testing are used to demonstrate and validate the proposed life-prediction methodology. Finally, some conclusions are drawn and future work proposed based on the results. The main novelties of the proposed study are: 1) provide a quantitative mechanical model for life prediction using the hybrid-controlled testing profile [28] and evidence from image-based analysis [40]; 2) provide a unified approach for the life prediction using both hybrid-controlled testing and classical strain-controlled testing; 3) check the applicability of the proposed method at both 850°C and 950°C using newly generated experimental data.

5.2 EXPERIMENTAL PROCEDURE AND IMAGING ANALYSIS RESULTS

The authors have developed a new hybrid-controlled testing profile for creep-fatigue testing of Alloy 617 at 950°C [28] and performed imaging analysis for the statistical analysis of micro-scale damage features [40]. Only a brief review of these techniques is given here for the completeness of this study. Detailed discussion and results can be found in the referred articles. Additional experimental testing results at 850°C are

presented in this study in order to demonstrate the proposed model at different temperatures.

The creep-fatigue tests in this study were run on an MTS servo-hydraulic load frame with a three-zone furnace. The Alloy 617 specimens were machined from a block of raw material such that the rolling direction was parallel to the loading axis of the specimen. The specimens had a round section with button-head ends and tangentially blended fillets at the gage section, in accordance with ASTM 2714-13. The specimen gage length was 20mm and gage section diameter was 7.5 mm.

All tests were performed in air at a constant temperature of either 850˚C or 950˚C. The temperature difference along the gage length was maintained below 10˚C with the help of four thermocouples that were wrapped on to the specimen at different locations. A contact extensometer with ceramic extension rods was used for strain measurement at the gage length. Fig. 5.1 (a) and (b) show the commonly used strain-controlled loading profile where the test specimen undergoes stress relaxation during the hold period. In this study, a hybrid-control loading profile [28] was applied, similar to the one shown in Fig. 5.1 (c) and (d). The loading and unloading was strain controlled at a rate of $1x10^{-3}$ /s, whereas the hold period was force-controlled at a predetermined intermediate stress level.

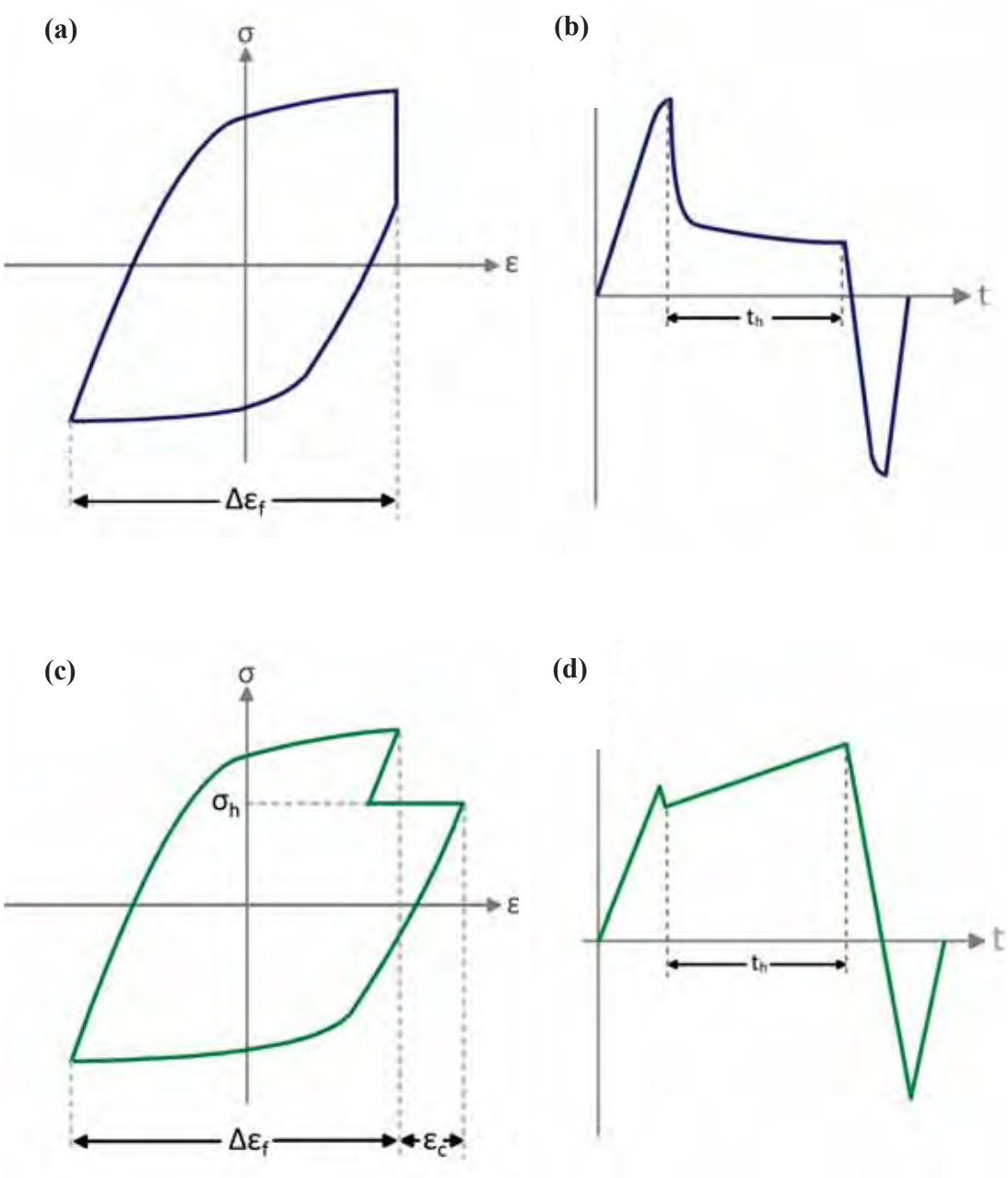

Fig. 5.1 (a), (b) – Traditional strain-controlled creep-fatigue loading profile; (c), (d) Hybrid-control loading profile.

In hybrid controlled tests, increasing the hold time causes a significant reduction in cycle life. This is contrary to strain controlled tests, where increasing the hold time beyond a certain threshold does not lead to any decrease in cycle life. The hybrid-control loading profile produces creep deformation instead of stress-relaxation during the hold period, thereby avoiding the saturation effect of increasing hold time on cycle life that is observed in strain-controlled testing. Moreover, in hybrid control loading profile, the stress at which creep occurs does not have to be the peak stress. Therefore, hybrid control loading waveforms can produce a variety of test data ranging from fatigue-dominated to creep-dominated interaction. In this study, the creep-fatigue interaction was varied by changing the fatigue strain range, (0.6% and 0.8%), holding stress (85 MPa and 100 MPa), and holding time (30 s, 180 s and 900 s). The 950°C creep-fatigue test data have been presented in [28]. Additional tests at 850°C were performed for this study. Fig. 5.2 shows the hysteresis curves, cyclic softening, and cyclic creep strain behavior for an 850°C test with 1.0% fatigue strain range, 100 MPa holding stress, and a 180s hold time. 850°C tests require longer hold periods than 950°C tests to produce the same amount of creep damage, as measured by effective time fraction approach. 850°C tests with hold periods of up to 10 hours were performed.

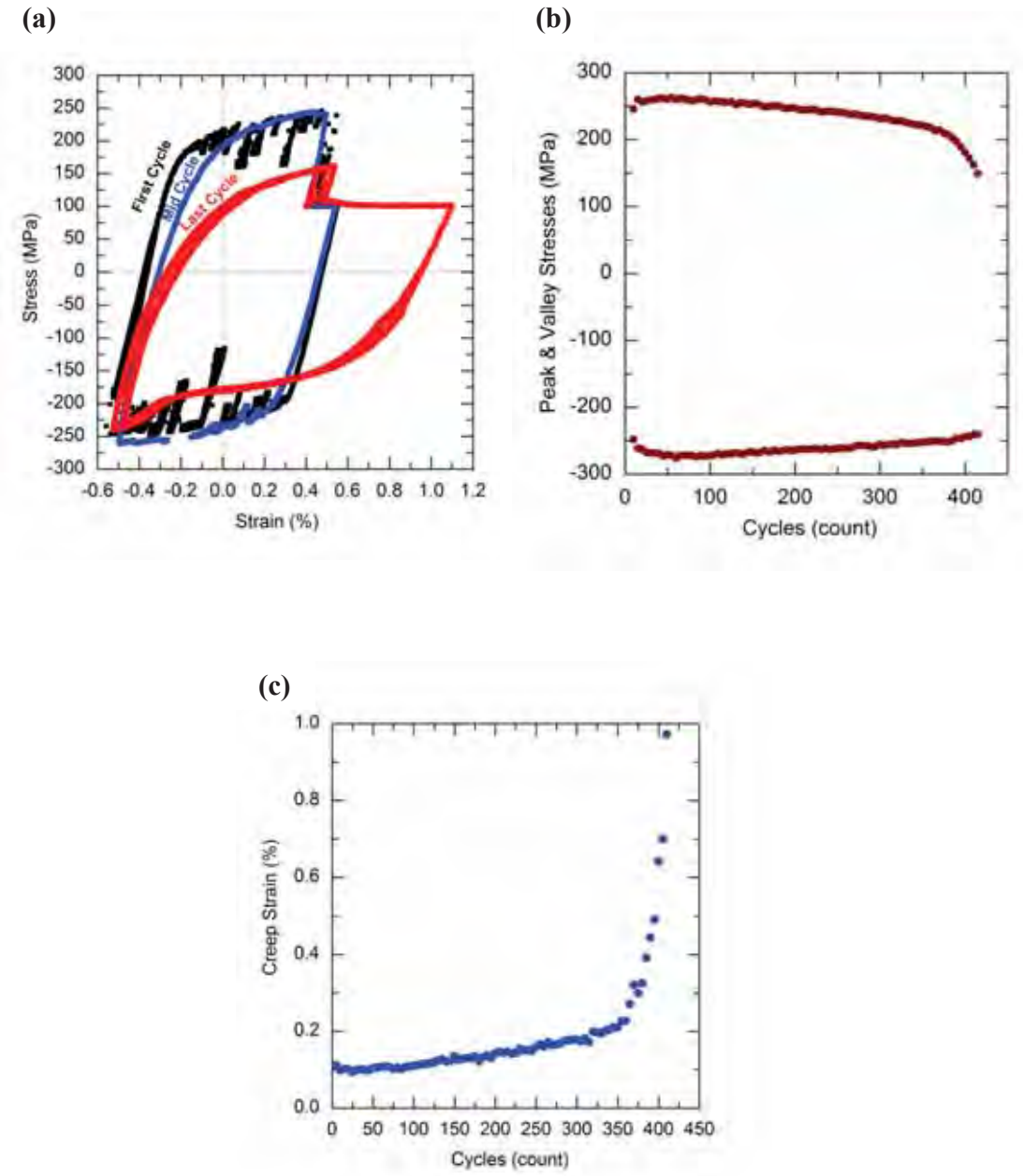

Fig. 5.2 – Test data from an 850°C test with 1.0% fatigue strain range, 100 MPa holding stress, and 180s hold time (a) Stress-strain curves from first, mid and last cycles and (b) Peak tensile and compressive stresses plotted against cycle count show cyclic softening; (c) Creep strain during the hold periods increases with cycles.

The new hybrid-controlled testing can produce data for creep dominated failure and is suitable for calibrating the entire damage interaction curve in the time fraction approach. Since the loading profile is very different from the classical strain-controlled testing, it was not clear how the micro-scale damage features related to the macro-level mechanical damage indicators (i.e., creep time fraction and fatigue cycle fraction). Thus, the authors performed an image-based analysis and statistical study to quantify the different micro-scale damage features of the failed specimens. Only the key results are shown here as they relate to the proposed life prediction model. Typical images for specimens with creep dominated failure and specimens with fatigue dominate failure are shown in Fig. 5.3(a) and Fig. 5.3(b), respectively. It was observed that creep dominated failure is characterized by a large number of internal voids and short and blunt surface cracks. On the contrary, fatigue dominated failure has minimal internal voids and long surface cracks. Thus, the internal void density and surface crack length are the representative micro-scale damage features for creep and fatigue, respectively. Extensive measurements were performed using a scanning electron microscope to quantify these two types of damage features for many different loading levels and hold periods. The quantified features were plotted against classical time fraction approach parameters to check for a correlation. The mean crack length vs. the fatigue damage fraction (i.e., n/N) is shown in Fig. 5.4(a). A good correlation was observed, suggesting that the fatigue cycle ratio is a reasonable indicator of fatigue damage. The void area fraction vs. the creep fraction in the classical time fraction approach (i.e., hold time/creep rupture time) is shown in Fig. 5.4(b). Different colors are used for different holding stress level and/or fatigue strain

range. There is a poor correlation between void fraction and classical time fraction, suggesting that the classical time fraction is not a reasonable indicator of creep damage. Thus, alternative mechanical parameters should be proposed and developed to better correlate with the micro-void density. The key challenge is how to define such a mechanical parameter and how to calculate this for arbitrary loading profiles for life prediction. This is the main motivation of the proposed study and is illustrated in detail in the next section.

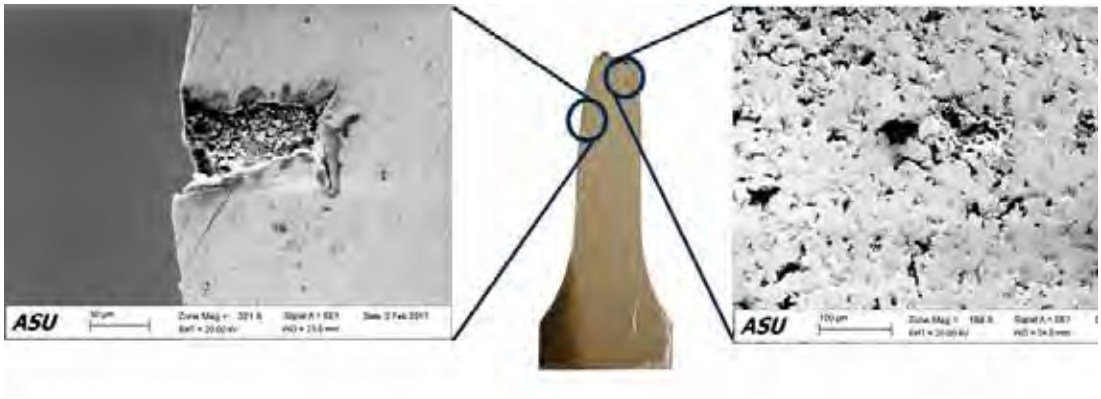

(a)

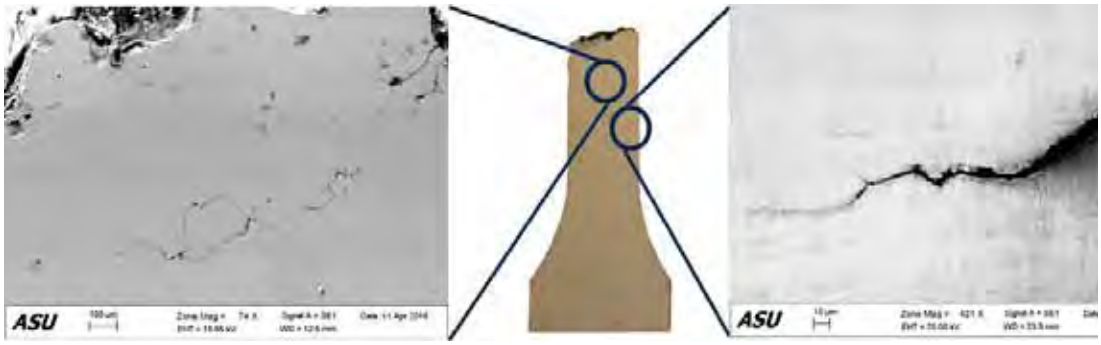

(b)

Fig. 5.3 (a) – Failed specimen with creep dominated failure shows short surface cracks and large internal voids and (b) – failed specimen with fatigue dominated failure shows minimal internal voids and long surface cracks.

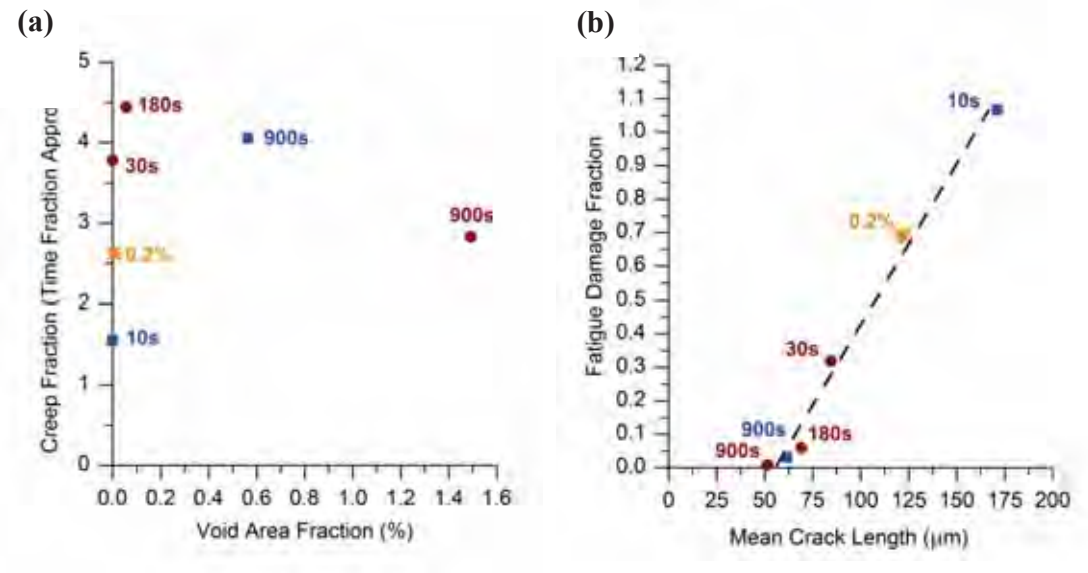

	Fatigue Strain Range (%)	Holding Stress (MPa)	Type of Hold Period
●	0.6	100	time limit
■	0.8	85	time limit
✱	0.8	85	strain limit

Fig. 5.4 (a) – Correlation between classical creep time fraction and area fraction of voids on the failed specimen; (b) – Correlation between fatigue cycle fraction and mean length of surface cracks on failed specimens.

5.3 PROPOSED LIFE PREDICTION MODEL

This section develops the proposed life prediction model. The classical time fraction approach is briefly reviewed, as it provides the basis for the proposed life prediction methodology. Following this, the basic hypothesis and derivation of the effective time

fraction approach is shown based on the hybrid-controlled testing profile. Next, the model is extended to strain-controlled testing profile as well, which aims to unify the proposed concept to arbitrary loading waveforms. Details are shown below.

5.3.1 Review of the Time Fraction Rule

Linear summation of fatigue cycle fraction (D_f) and creep time fraction (D_c) in the classical time fraction approach can be stated as [22]:

$$\sum_i \left(\frac{N_{cf}}{N_f}\right)_i + \sum_j \left(\frac{t_h}{T_r}\right)_j \leq D \qquad (1)$$

where, N_{cf} is the cycle life in the creep-fatigue testing, N_f is the cycle life in pure fatigue testing at the same strain level, t_h is the tensile hold time, T_r is time to rupture in pure creep testing. D is a material dependent parameter. Creep-fatigue interaction is known to follow a bilinear trend line on a damage interaction diagram for some steels [21,30,39].

In the case of Alloy 617 at 800-1000˚C, use of the time fraction rule to calculate creep damage results in large scatter and absence of a trend on the creep-fatigue interaction diagram [5,9,39]. There are several reasons for the absence of a trend on the interaction diagram: (i) Rapid stress relaxation of Alloy 617 at high temperatures means that increasing the hold time does not necessarily lead to a decrease in cycle life. After the initial phase of rapid stress relaxation, maintaining the strain hold for a longer period of time does not lead to an increase in creep strain. This is also known as the saturation effect of hold time on creep damage [7]; (ii) The time fraction rule assumes that the entire hold time is involved in irreversible creep deformation. For this to be true, the creep time

fraction cannot be larger than unity [13]. On the contrary, creep fractions larger than unity have been reported for several metals [5,14,21,22,31,35]; (iii) Creep-fatigue tests are traditionally conducted in strain-control where there is stress relaxation during the hold time, instead of creep deformation. The creep time fraction, in which hold time is normalized by creep rupture time, then assumes that steady-state creep behavior and stress relaxation response are mechanistically equivalent.

5.3.2 Effective Time Fraction Approach – Hybrid-Controlled Testing

As illustrated in the previous section, image analysis shows that the classical time fraction parameter for calculation for creep damage does not show a good correlation with the micro-scale damage features. Further evidence for this hypothesis is obtained when the experimental data are plotted on a damage diagram using the classical time fraction approach. This damage diagram is shown in Fig. 5.5. The data shows a large scatter with most of the creep fractions exceeding unity. This confirms that the classical time fraction approach is not appropriate for the creep-fatigue life prediction, at least for the hybrid-controlled testing data. The creep damage fraction should, in principle, be less than unity for the creep-fatigue testing with an extreme value of unity being achieved for pure creep rupture testing. This observation indicates that the classical time fraction calculation for creep damage ‘overestimates’ the creep damage by using the entire duration of the hold time. In other words, only a portion of the hold time contributes to the creep damage so the calculation of the creep damage should only count this ‘effective’ portion of the hold time. For this reason, the proposed approach is called the effective time fraction approach.

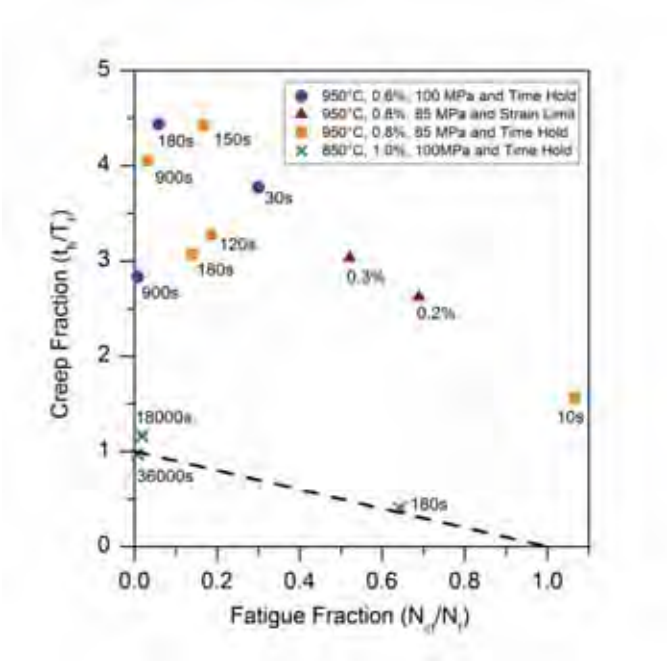

Fig. 5.5 – Damage interaction diagram using time fraction rule for hybrid-controlled creep-fatigue tests.

A hypothesis is proposed based on the above observations: the effective hold time corresponds to the time spent for the net creep strain increment compared to the last cycle. In hybrid-controlled testing, cyclic softening is observed and the creep strain rate during the hold time increases with cycles. The effective time fraction approach assumes that after the first cycle, only a fraction of the hold time is involved in the net creep deformation. This fraction, called effective hold time (t_{eh}), is part of the hold time during which a net increase of creep strain occurs with respect to the previous cycle. The schematic in Fig. 5.6 shows the application of the effective time fraction approach to the first three cycles of a creep-fatigue test with fixed hold time per cycle. Given that hold time is fixed, effective hold time for each cycle is the time spent to increase the creep

strain from the creep strain in the previous cycle. It can be calculated by considering the increase in creep strain rate with each cycle as:

$$\sum t_{eh} = \sum_{k=0}^{N_{cf}-1} \left(\frac{\dot{\varepsilon}_{k+1} - \dot{\varepsilon}_k}{\dot{\varepsilon}_{k+1}}\right)\left(t_{h(k+1)}\right) \tag{2}$$

where, $\dot{\varepsilon}_k$ represents the creep strain rate in cycle number k. The linear summation of creep and fatigue damage then becomes:

$$\sum_i \left(\frac{N_{cf}}{N_f}\right)_i + \sum_j \left(\frac{t_{eh}}{T_r}\right)_j \leq D \tag{3}$$

where, the first term is the fatigue damage fraction and the second term is the effective creep damage fraction.

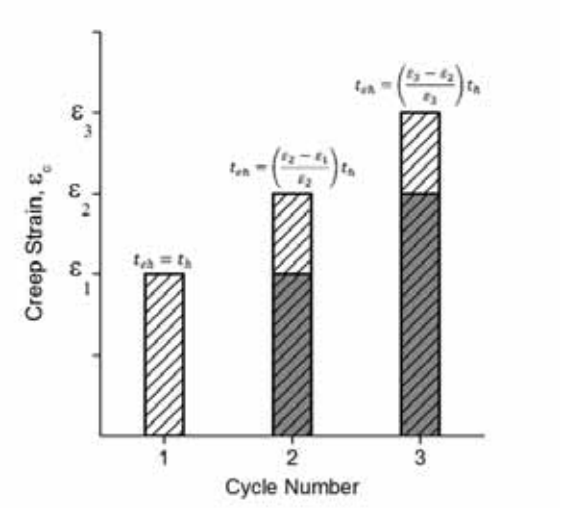

Fig. 5.6 – Schematic showing first three cycles of a creep-fatigue test. White shaded area represents the strain accumulated during the effective hold time.

For tests with fixed hold time per cycle, Eq. (2) can be simplified as:

$$\sum t_{eh} = t_h \left(\sum_{k=0}^{n-1} \left(\frac{\varepsilon_{(k+1)} - \varepsilon_{(k)}}{\varepsilon_{(k+1)}} \right) \right) \tag{4}$$

Similarly, for tests with fixed creep strain per cycle, Eq. (2) can be simplified as:

$$\sum t_{eh} = \sum_{k=0}^{n-1} \left| t_{h(k)} - t_{h(k+1)} \right| \left(\frac{t_{h(k+1)}}{t_{h(k)}} \right) \tag{5}$$

In hybrid-control tests, the stress is constant during the hold time so the effective creep damage fraction (D_{ec}) is:

$$D_{ec} = \frac{\sum_{k=1}^{N_{cf}} (t_{eh})}{T_r} \tag{6}$$

The inputs required for this calculation are: creep strain rate/creep strain as a function of cycles, and creep rupture time. For tests with fixed hold time per cycle, the creep strain (ε_c) is approximated as:

$$\varepsilon_c = c_1 e^{c_2 \left(\frac{k}{N_{cf}} \right)} \tag{7}$$

where, $c_1$and c_2 are fitting constants for the creep strain vs normalized cycles curve. An average curve between creep strain rate and normalized cycles is shown in Fig. 5.7 for multiple hybrid-control tests. Substituting Eq. (7) into Eq. (4) and simplifying gives:

$$\sum_{k=1}^{N_{cf}} t_{eh} = N_{cf}\left(1 - e^{-\frac{c_2}{N_{cf}}}\right) \tag{8}$$

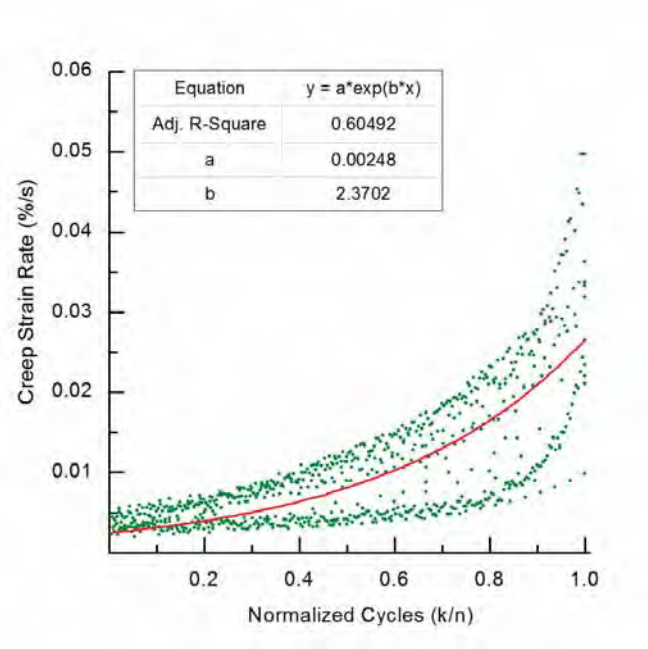

Fig. 5.7 – Exponential relation between creep strain rate and normalized cycles. Green dots represent creep strain rate vs cycles data from multiple hybrid-control tests.

Thus, for hybrid-control tests with a fixed hold time per cycle, the linear damage summation rule of Eq. (1) becomes:

$$\sum_i \left(\frac{N_{cf}}{N_f}\right)_i + \sum_j \left(\frac{N_{cf}\left(1 - e^{-\frac{c_2}{N_{cf}}}\right)}{T_r}\right)_j \leq D \qquad (9)$$

where, N_{cf} is the unknown. N_f is from the fatigue strain-life curve. T_r is the creep rupture time from the creep Larson-Miller plot. c_2 is from the creep strain vs normalized cycles curve fit and D is from the creep-fatigue interaction diagram for the given material and temperature.

5.3.3 Effective Time Fraction Approach – Strain-Controlled Testing

This section extends the effective hold time concept to the classical strain-controlled test using literature test data. The hybrid-control loading profile has a force-controlled hold period so the net creep increment can be extracted directly from the hysteresis curve. However, for strain-controlled tests, which have stress relaxation during the hold period, the net creep increment per cycle must be calculated. In the strain-controlled tests, the stress relaxation data can be fitted by [30]:

$$\sigma = \frac{\sigma_0(N)}{e^{b_1 t^{b_2}}} \qquad (10)$$

where, $\sigma_0(N)$ is the peak stress for cycle N. t is the time from start of the hold period. b_1 and b_2 are fitting constants for the stress relaxation curve. The peak stress drops as a function of cycles due to the cyclic softening and damage accumulation. In the proposed study, it is approximated as:

$$\sigma_0(N) = a_1N^4 + a_2N^3 + a_3N^2 + a_4N + a_5 \tag{11}$$

where, a_{1-5} are fitting constants. Total strain (ε_t), which is constant for each cycle, can be decomposed as:

$$\varepsilon_t = \varepsilon_e + \varepsilon_p + \varepsilon_c \tag{12}$$

where, $\varepsilon_e$is the tensile elastic strain. ε_p is the tensile plastic strain. ε_c is the creep strain. Rearranging Eq. (12) and substituting Eq. (10):

$$\varepsilon_c = \varepsilon_t - \varepsilon_p - \frac{\sigma_0(N)}{Ee^{b_1 t^{b_2}}} \tag{13}$$

For Cycle 1:

$$t' = 0 \tag{14}$$

$$t_{eh}(N = 1) = t_h - t' = t_h \tag{15}$$

$$\varepsilon_c(t = t_h, N = 1) = \varepsilon_t - \varepsilon_p - \frac{\sigma_0(1)}{Ee^{b_1 {t_h}^{b_2}}} \tag{16}$$

where, t' is defined as the time in current cycle when the creep strain equals the creep strain in the previous cycle.

For Cycle 2:

At $t = t'$, the creep strain in current cycle equals the creep strain in previous cycle, i.e.

$$\varepsilon_c(t', 2) = \varepsilon_c(t_h, 1) \tag{17}$$

$$\varepsilon_t - \varepsilon_p - \frac{\sigma_0(2)}{E e^{b_1 {t'}^{b_2}}} = \varepsilon_t - \varepsilon_p - \frac{\sigma_0(1)}{E e^{b_1 {t_h}^{b_2}}} \tag{18}$$

Assuming that the plastic strain and Young's modulus do not change significantly for consecutive cycles, Eq (18) becomes:

$$\ln\left(\frac{e^{b_1 {t_h}^{b_2}}}{e^{b_1 {t'}^{b_2}}}\right) = \ln\left(\frac{\sigma_0(1)}{\sigma_0(2)}\right) \tag{19}$$

$$b_1 {t_h}^{b_2} - b_1 {t'}^{b_2} = \ln\left(\frac{\sigma_0(1)}{\sigma_0(2)}\right) \tag{20}$$

$$t' = \left[{t_h}^{b_2} - \frac{1}{b_1}\ln\left(\frac{\sigma_0(1)}{\sigma_0(2)}\right)\right]^{1/b_2} \tag{21}$$

Therefore, for Cycle N:

$$t'(N) = \left[\left(t'(N-1)\right)^{b_2} - \frac{1}{b_1}\ln\left(\frac{\sigma_0(N-1)}{\sigma_0(N)}\right)\right]^{1/b_2} \tag{22}$$

Effective creep damage fraction for the strain-controlled test is given by:

$$D_{ec} = \sum_{N=1}^{N_{cf}} \int_{t'(N)}^{t_h} \left(\frac{1}{T_r}\right) dt \tag{23}$$

Similar to the last section for the hybrid-controlled test, Eq. (23) and Eq. (3) provide the proposed life prediction for a strain-controlled test.

5.4 RESULTS AND DISCUSSION

This section demonstrates the application and validation of the proposed life prediction model to Alloy 617 at high temperatures. The model was first validated using the 950°C test data. Two types of data was used. The first type is the hybrid-controlled testing data reported in [28]. For each strain range (i.e. 0.6% and 0.8%), the hybrid-controlled tests used holding stresses of 85MPa or 100MPa and various hold times. The second type is strain-controlled test data reported in [29]. For each strain range (i.e. 0.3%, 0.6%, and 1.0%), the strain-controlled tests had hold times of 180s, 600s, or 1800s. The effective time fraction approach is used to plot the experimental data in Fig. 5.8. The x-axis is the fatigue cycle fraction and the y-axis is the effective time fraction for creep damage. A clear bilinear trend is observed and experimental data has considerably less scatter compared to the plot that used classical time fraction approach.

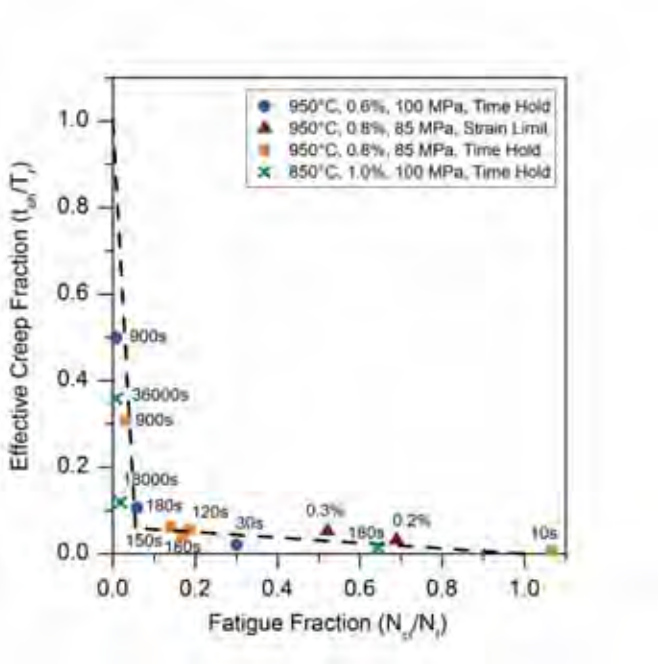

Fig. 5.8 – Damage interaction diagram using effective time fraction approach for hybrid-controlled creep-fatigue tests.

An intersection point of (D_f, D_{ec}) = (0.0542, 0.0595) was obtained by curve fitting the 950°C hybrid-controlled test data, as shown in Fig. 5.9(a). ASME draft code case for Alloy 617, which uses the classical time fraction rule, suggests (D_f, D_c) = (0.1, 0.1) as the intersection point for the bilinear damage envelope [9]. The values of the effective creep fraction were less than 0.005 for all strain-controlled tests, indicating minimal creep damage. The implication that strain-controlled tests are not capable of generating significant creep damage is supported by damage observations of failed test specimens, which only show intergranular fatigue cracks and no creep voids [8]. The life-prediction for all tests is shown in Fig. 5.9(b). The x-axis is the experimental observed life and the y-axis the predicted life using the effective time fraction model. Most data fall into the

scatter band with a life factor of 3. It should be noted that there is a systematic error associated with the strain-controlled testing data as all predicted lives are longer than the experimental lives. The reason for this behavior is not clear for now. The authors suspected that this is possibly due to additional damage mechanisms that exist in the strain-controlled CF testing, which are not included in the current formulation. Additional experimental and theoretical investigation is required to further explain this observation.

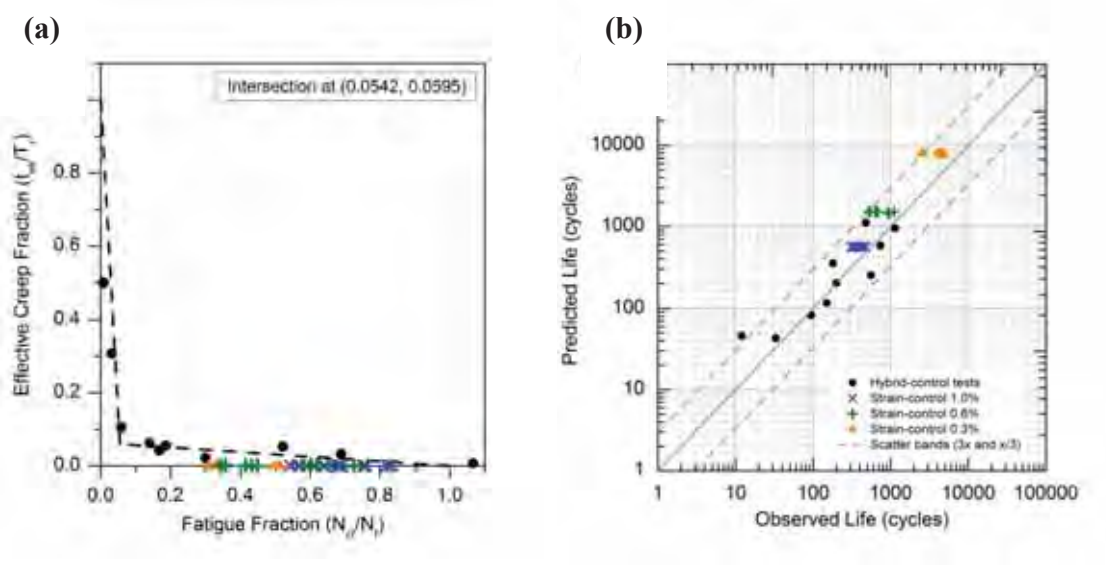

Fig. 5.9 – (a) Creep-fatigue interaction diagram and (b) life prediction using effective time fraction approach for strain-control [29] and hybrid-control tests at 950°C.

Additional hybrid-control tests were performed at 850°C to check the existence of a bilinear interaction trend as well as the applicability of the proposed life prediction model. Fig. 5.10(a) shows the bilinear trend at 850°C. In comparison to the 950°C data, the intersection point for 850°C data is closer to the origin of the interaction diagram. Fig.

5.10(b) shows again that the life-prediction for these tests also lies within a scatter band of 3. Due to the limited number of specimens available for testing at this temperature, only four data points are reported for the holding stress of 100 MPa with varying holding periods. Additional experiments at other holding stresses may be required for a more comprehensive evaluation.

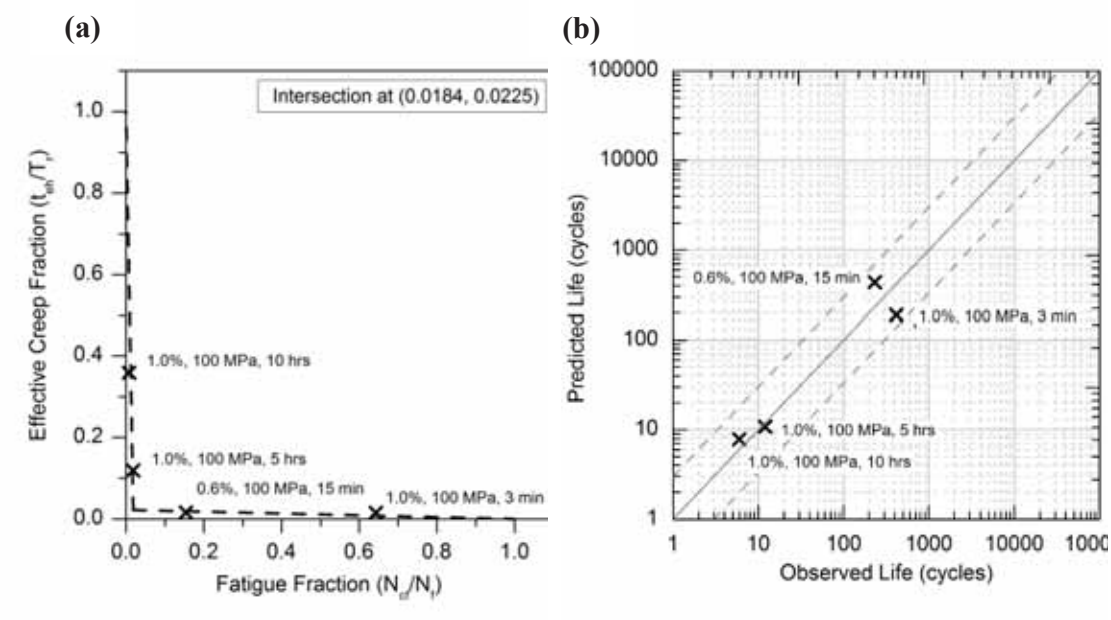

Fig. 5.10 – (a) Creep-fatigue interaction diagram with data labels indicating fatigue strain range, holding stress, and hold time; (b) life prediction using effective time fraction approach for hybrid-control tests at 850°C.

Physical evidence for the effective time fraction approach is provided by Fig. 5.11, where a correlation can be seen between effective time fraction for creep and the area fraction of voids on failed 950°C test specimens. Unlike the classical time fraction approach shown in Fig. 5.5, Fig. 5.11 shows that a larger effective creep fraction corresponds to larger void area fraction.

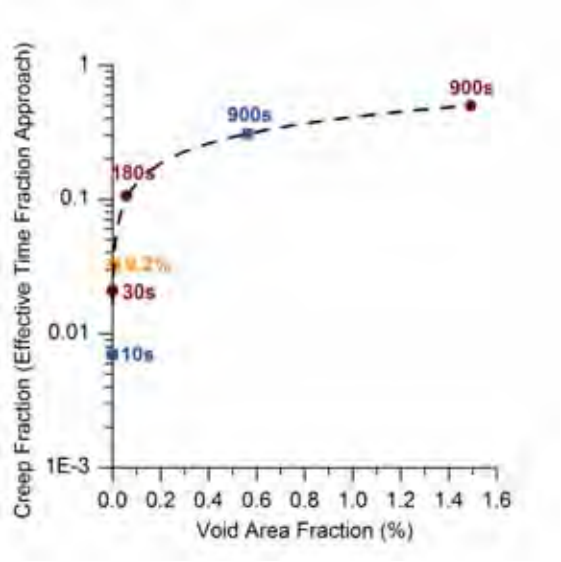

	Fatigue Strain Range (%)	Holding Stress (MPa)	Type of Hold Period
●	0.6	100	time limit
■	0.8	85	time limit
✱	0.8	85	strain limit

Fig. 5.11 – Correlation between effective time fraction for creep and area fraction of voids on the failed specimen;

5.5 CONCLUSION

An effective time fraction approach, that takes into account the increase in creep strain with cycles, is introduced within the framework of the widely used time fraction and damage summation rule. Several major conclusions can be drawn based on this study.

- Classical time fraction rule fails to correlate with the hybrid-controlled creep-fatigue test data and the creep fraction is usually larger than unity, which is not physically sound;

- The effective time fraction approach correlates well with experimental data with smaller scatter bands in life prediction;
- The damage diagram using the effective time fraction concept has a clear bilinear trend for the experimental data;
- A lower temperature will move the intersection point of the bilinear curve (in the effective time fraction approach) towards the origin of the damage interaction diagram.
- The proposed model shows a systematic error for strain-controlled testing although the scatter band is less than 3.

The proposed model relies on the hypothesis that only the time during the net creep strain increment is responsible for the creep damage. This is only tested for Alloy 617 at temperatures of 850°C and 950°C. Extension of this concept to other materials at high temperatures needs significant future research. Care must be taken when using the conclusions of this study to lower temperatures as the deformation mechanisms are different and stress relaxation behavior may not be as significant as Alloy 617 at high temperatures. Additional study is required to investigate the proposed model to strain-controlled experiments as the results suggest additional failure mechanisms may exist. The proposed model is a phenomenological model that is supported by observations of physical damage. Approaches based on damage mechanics and fracture mechanics may provide more physical insights into life prediction of hybrid-controlled and strain-controlled test data.

6. UNIFIED VISCOPLASTICITY MODELING FOR CREEP-FATIGUE LIFE PREDICTION

6.1 INTRODUCTION

Design codes for nuclear components typically adopt simple empirical models such as time fraction rule [32,41], ductility exhaustion [33], and strain range partitioning [36] to evaluate creep-fatigue life. The life assessment rules are calibrated by fitting experimental data from a large number of creep-fatigue tests. Running elevated temperature tests is time consuming and resource intensive. Moreover, the loading waveforms for such tests are not fully representative of the actual operating conditions of the components. Reliable life prediction for components under complex loading waveforms can be achieved by modeling the constitutive behavior of the material as well as the effects of microstructural damage. The stresses and strain rates during service conditions of the components are lower than what can be realistically achieved in creep-fatigue tests. Constitutive modeling of cyclic deformation provides a means for extrapolating the results of short-term tests to long-term operating conditions of the components.

Viscoplastic models are rate-dependent and therefore suitable for modeling the cyclic deformation of metals and alloys at elevated temperatures. The Chaboche unified viscoplastic model is used in literature to model a wide variety of materials [42–44], including Ni-base superalloys at elevated temperatures [45–50]. Carroll et al. [51] demonstrated the capability of the Chaboche model to simulate the creep-fatigue

response of Alloy 617 at 850 and 950°C. Sham et al. [52] used the Chaboche model to simulate low-stress long-term creep behavior of Alloy 617. This model employs mechanism-based internal state variables to capture various features of the stress-strain response including monotonic hardening, cyclic hardening and softening, Bauschinger effect and partially ratchetting [53]. The unified viscoplastic model makes use of internal state variables, e.g. back stress and drag stress [54], that are analogous to physical deformation mechanisms[55]. The back stress variable represents the interaction of moving dislocations with grain boundaries, whereas the drag stress variable represents the interaction of moving dislocations with precipitates or solute atoms. Since, plasticity and creep are governed by the same deformation mechanism i.e. movement of dislocations, the unified viscoplastic model represents the plastic and creep strains by a single variable known as inelastic strain.

In Alloy 617, creep damage is produced by nucleation and linkage of intergranular voids, whereas fatigue damage is caused by initiation and growth of oxidation-induced surface cracks [25,26,40,56–58]. The interaction between creep and fatigue damage mechanisms accelerates failure under creep-fatigue conditions. The effects of microscopic damage are incorporated into the macroscopic unified viscoplastic model with the introduction of internal damage variables [44,59–61]. Typically, the creep damage variable is a function of time and fatigue damage variable is a function of cycles. The simultaneous effect of creep and fatigue is modeled by linear or non-linear accumulation of creep and fatigue damage variables [44].

This study combines the unified viscoplastic model with a damage variable based on a model parameter to predict creep-fatigue life of Alloy 617 at 950°C for a non-standard loading waveform with strain-controlled ramps and force-controlled tensile hold periods. First, the details of the internal variables including model equations are provided. Following this, the optimization of model parameters and sensitivity of the model to changes in these parameters are discussed. Next, damage evolution equations based on the results of sensitivity analysis are introduced along with a damage interaction model based on creep and fatigue energy. The damage model is calibrated using creep-fatigue tests. Finally, life prediction results for creep-fatigue tests are compared with experimental data.

6.2 RESULTS AND DISCUSSION

6.2.1 Unified Viscoplastic Model

The uniaxial form of the unified viscoplastic model used in this study is adopted from Chaboche and Rousselier [42,62]. The total strain, ε, is decomposed into elastic, ε^e, and inelastic, ε^{in}, parts:

$$\varepsilon = \varepsilon^e + \varepsilon^{in} \tag{1}$$

The flow rule relates the inelastic strain rate, $\dot{\varepsilon}^{in}$, to the stress, σ, and internal variables i.e. back stress, χ, and drag stress, R.

$$\dot{\varepsilon}^{in} = \langle {}^{f}/_{Z} \rangle^n \, sgn(\sigma - \chi) \tag{2}$$

where,

$$sgn(x) = \begin{cases} 1, & x > 0 \\ 0, & x = 0 \\ -1, & x < 0 \end{cases} \qquad \text{and} \qquad \langle x \rangle = \begin{cases} x, & x \geq 0 \\ 0, & x < 0 \end{cases}$$

Consequently, the viscoplastic multiplier, $\dot{p}$, is defined as

$$\dot{p} = \left\langle \frac{f}{Z} \right\rangle^{n} \tag{3}$$

where, Z and n are viscous parameters responsible for rate dependence of the stress. The function, f, defines the elastic domain as

$$f(\sigma, \chi, R) = |\sigma - \chi| - R - \sigma_{Y0} \leq 0 \tag{4}$$

where, σ_{Y0} is the initial yield stress.

The back stress, χ_i , controls the direction-dependent Bauschinger effect. The evolution of the back stress follows the non-linear kinematic hardening rule of Armstrong and Frederick [63].

$$\dot{\chi}_i = C_i\left(a_i \dot{\varepsilon}^{in} - \chi_i \dot{p}\right) \tag{5}$$

where, C_i and a_i are constants, and i = 1, 2

The drag stress, R, controls the direction-independent cyclic hardening or softening, also known as isotropic hardening. The drag stress evolves as

$$\dot{R} = b(Q - R)\dot{p} \tag{6}$$

where, b and Q are constants.

The viscous overstress, $\dot{\sigma}_v$, is given by the Norton's power law equation for steady-state creep

$$\sigma_v = Z\dot{p}^{1/m} \tag{7}$$

The stress decomposition is as follows

$$\sigma = \chi + (R + \sigma_{Y0} + \sigma_v)sgn(\sigma - \chi) \tag{8}$$
$$= E(\varepsilon - \varepsilon^{in})$$

This form of the model requires 10 material parameters, namely, the Young's modulus, *E*; kinematic hardening parameters, a_1, a_2, C_1, C_2; isotropic hardening parameters, *b* and *Q*; viscous parameters, *Z* and *m*; and the initial yield stress, σ_{Y0}.

6.2.2 Calibration of Model Parameters

The system of ordinary differential equations from the unified viscoplastic model was solved in Matlab using the 'Ode45' solver which uses an explicit Runge-Kutta method. The parameters were then optimized relative to an experimental stress-strain curve, using the 'fminsearch' function in Matlab. The strain-controlled loading and unloading parts were optimized first by comparing the stresses. Subsequently, the stress-controlled tensile hold period was optimized by comparing the strains. Initial estimates for the material parameters were taken from [64]. Table 6.1. shows the initial and optimized model

parameters.

	E (GPa)	σ_{y0} (MPa)	b	Q (MPa)	a_1 (MPa)	C_1	a_2 (MPa)	C_2	Z (MPa $s^{1/m}$)	m
Initial parameters	139	30	28.6	27.4	80	7112	116	929	170	10
Optimized parameters	124	19.4	43.7	-43.9	-394	1650	700	1583	706	3.69

Table 6.1. Initial and optimized model parameters for Alloy 617 at 950°C

6.2.3 Damage Model

The hybrid-control creep-fatigue loading waveform is particularly suitable of generating varying proportions of creep and fatigue damage. Unlike the traditional strain-controlled creep-fatigue loading, where strain hold periods cause stress relaxation, the hybrid-control loading profile employs stress-controlled hold periods to generate creep deformation. Under such loading conditions, the two main indicators of damage are: (i) the decrease in peak stress with cycles; and (ii) the increase in creep strain with cycles. Therefore, the sensitivity of these indicators to changes in model parameters were analyzed. Since, the strain range for the fatigue cycle is fixed, the changes in creep strain can be represented by peak strain. Fig. 6.1(a) and (b) show a sensitivity analyses for peak stress and peak strain respectively, for a single cycle by changing one model parameter at time.

The sensitivity analysis shows that both peak stress and peak strain are most sensitive to the viscous parameter, ‘m’. Additionally, reducing ‘m’ can simultaneously cause a drop in peak stress and a rise in creep strain. Although the model is also sensitive to parameters Z, a_1, and a_2; the parameter ‘m’ is selected to represent the damage due to its

physical importance as the power in the Norton law equation, which relates applied stress to the secondary creep strain rate.

(a)

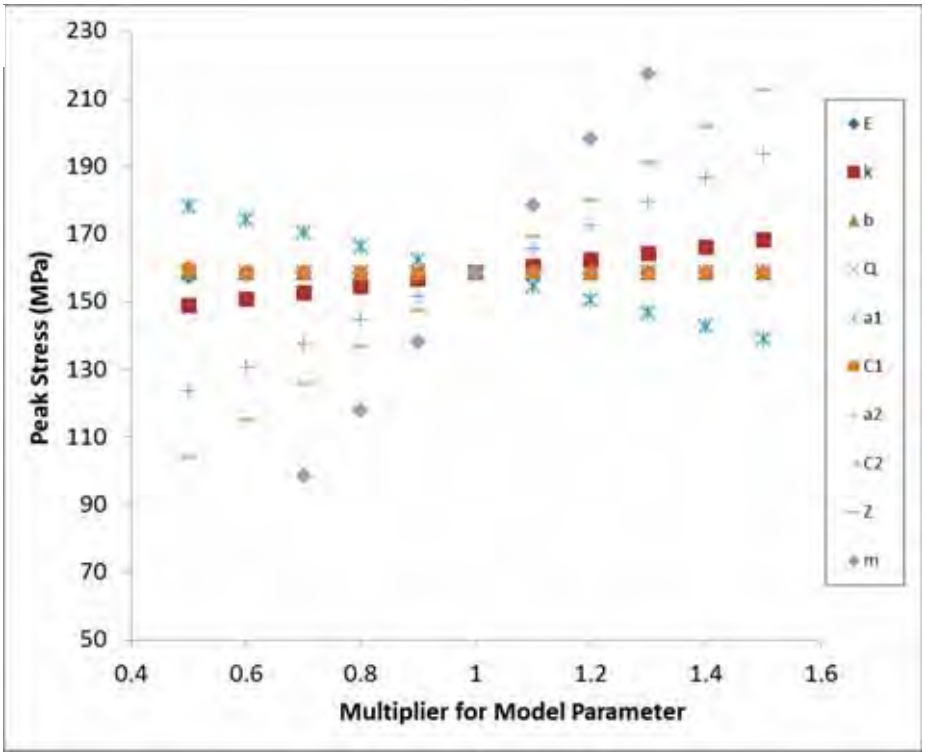

(b)

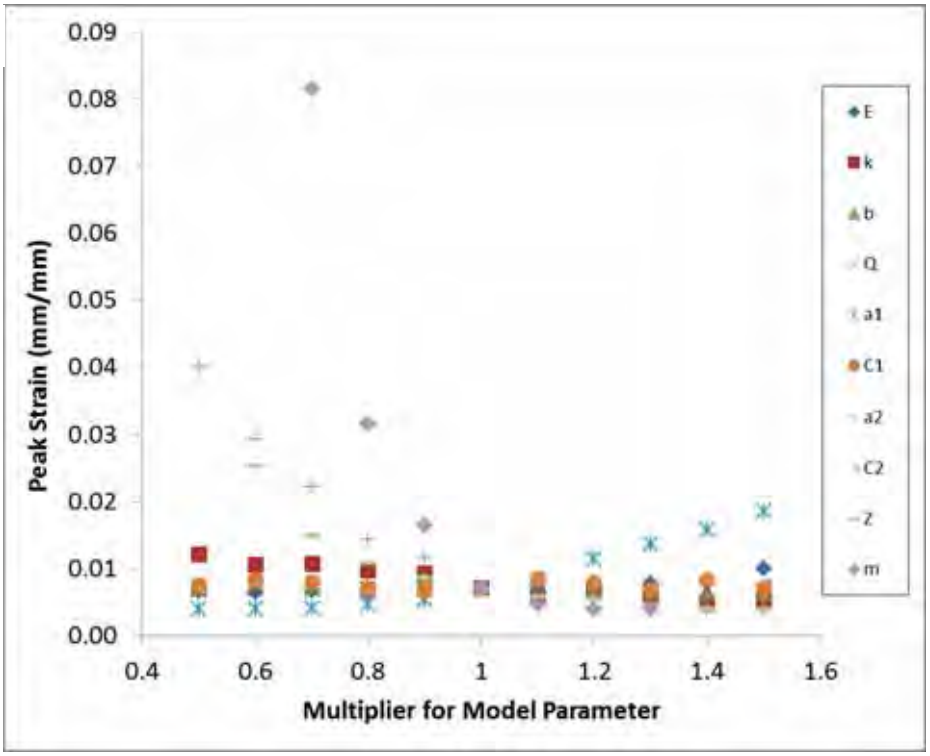

Fig. 6.1 – Sensitivity of (a) peak stress and (b) peak strain to changes in model parameters.

Next, the experimental hysteresis data from a hybrid-control creep-fatigue test was combined with the sensitivity analysis results to obtain the degradation of Young's modulus, E, and viscous parameter, m, as decreasing functions of cycles, n. The model equations were then solved in Matlab to find the accumulated fatigue energy, ΣE_f, and cyclic creep energy, E_c. The model was then fitted with creep-fatigue data from multiple tests to find a creep-fatigue interaction relation (Eq. 9) when equivalent damage, D_{eq}, equals unity. Fig. 6.2 shows the result of this fitting.

$$D_{eq} = \left(\frac{\sum E_f}{\sum E_f^*}\right)^q + \left(\frac{E_c}{E_c^*}\right)^q = 1 \qquad (9)$$

Following this, the degradation of parameter ‘m’ in the simulation with damage function, D_{eq}, was found. Fig. 6.3 show this degradation. Fig. 6.4 shows the procedure followed for calibrating the damage model for parameter ‘m’. A similar procedure was followed for Young’s modulus, E. ΣE_f^* is the accumulated fatigue energy for a pure fatigue test and E_c^* is the creep energy from a pure creep test.

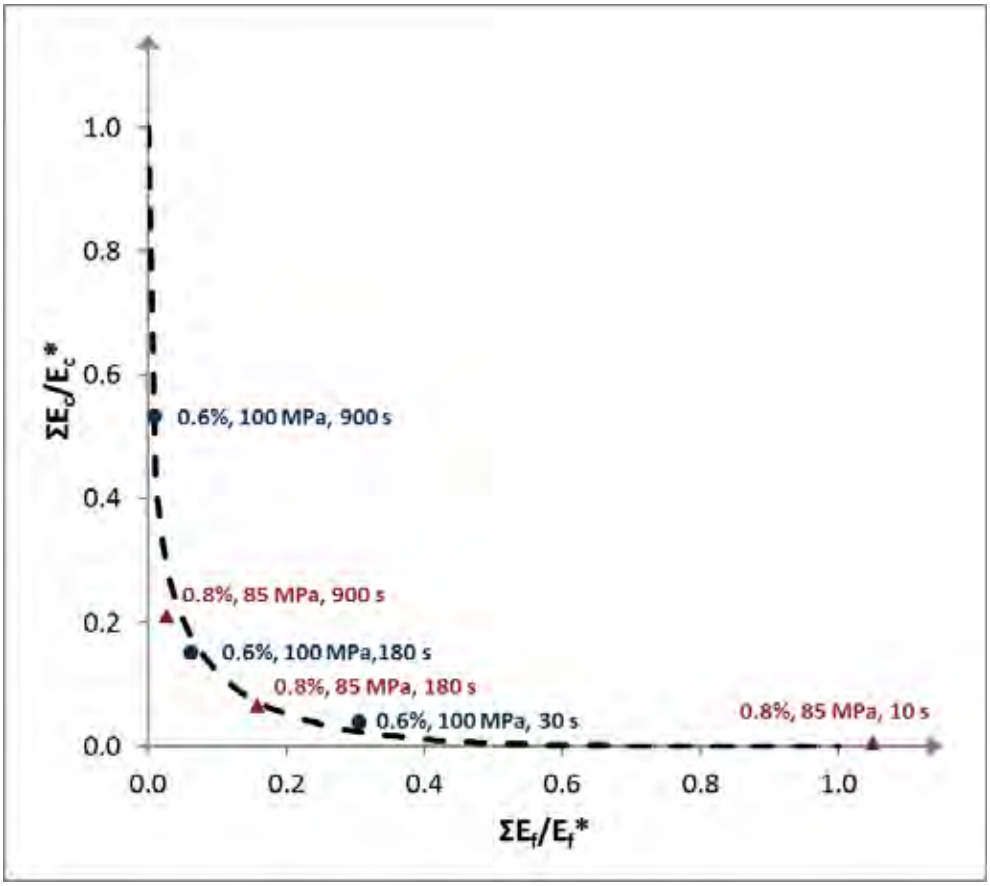

Fig. 6.2 – Damage interaction diagram to determine the exponent ‘q’ in damage interaction rule.

(a)

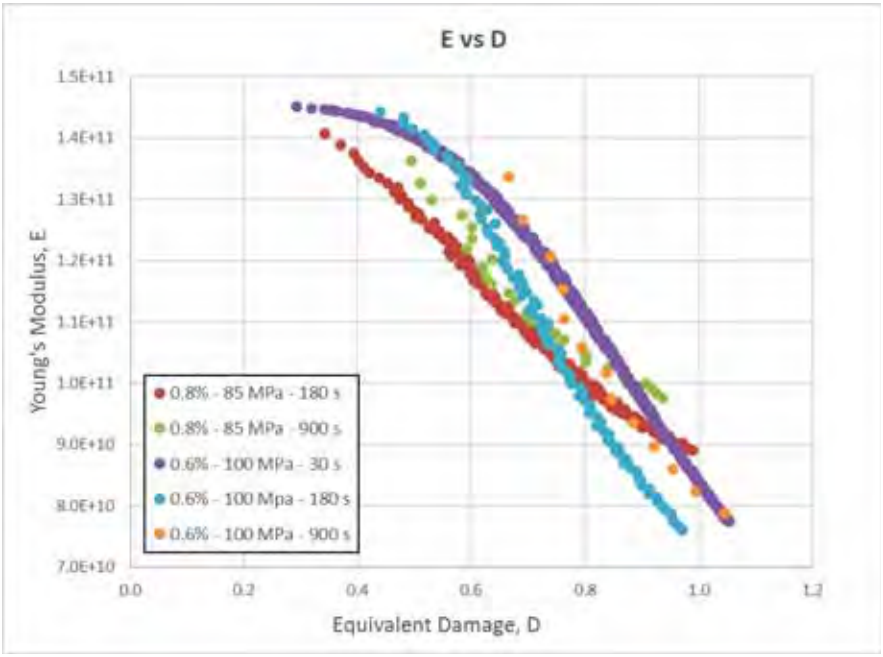

(b)

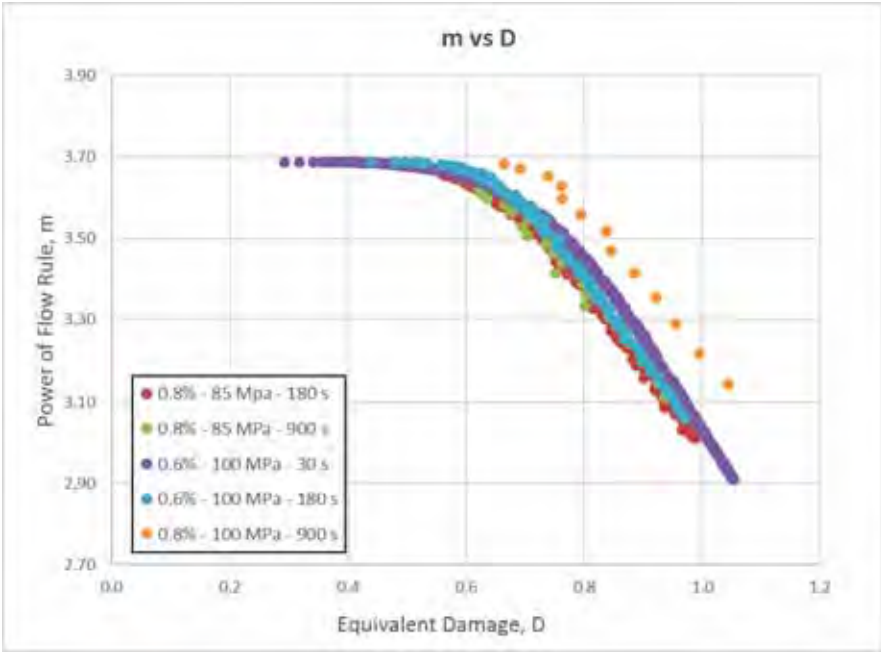

Fig. 6.3 – Degradation of model parameters (a)'m' and (b)'E' with equivalent damage, D_{eq} for multiple tests

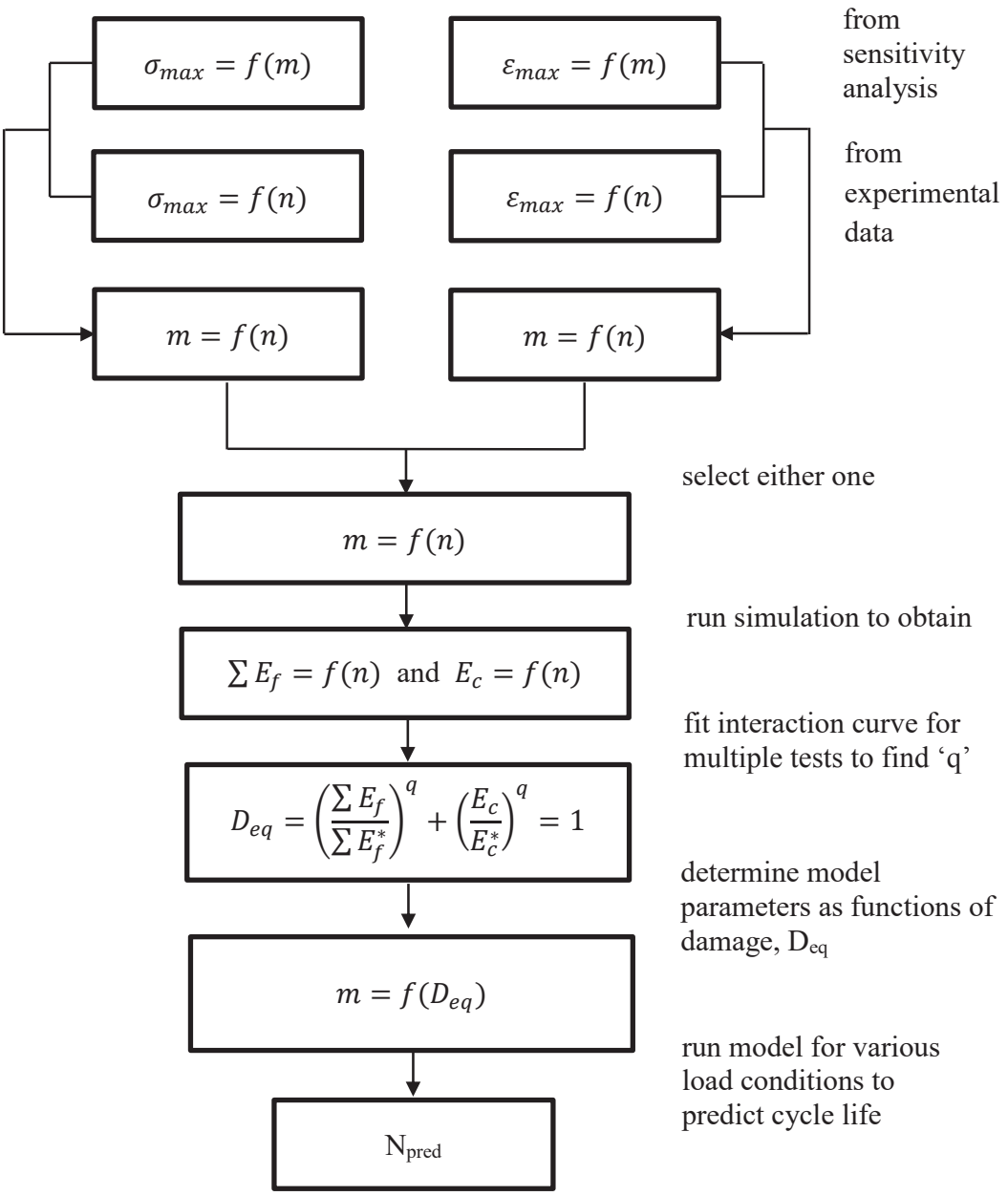

Fig. 6.4– A flowchart showing the development of the life-prediction rule for parameter 'm', from the experimental data and damage law.

6.2.4 Model validation and life prediction

Fig. 6.5 shows the final life-prediction for the tests. Predicted lives fall within a scatter band of 2. This is better than the effective time fraction approach.

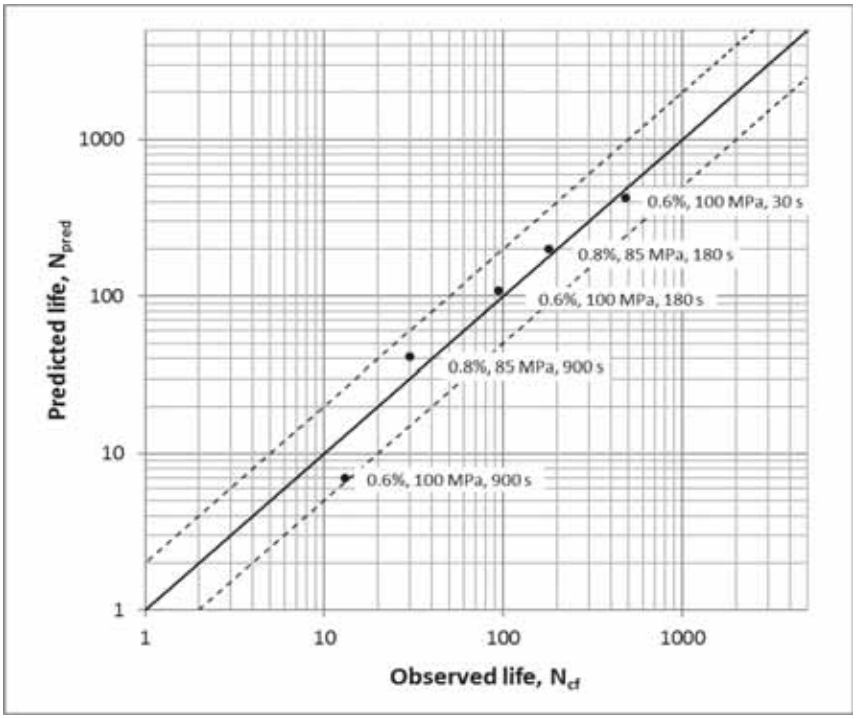

Fig. 6.5 – Predicted vs observed life for hybrid-control tests.

The viscoplastic model with damage was finally run to compare the stress-strain response, cyclic softening, and creep strain increase with experimental data. Fig. 6.6 shows the stress-strain curves for experiment and simulation for cycle 10, mid cycle and last cycle of a hybrid-control test with 0.8% strain range, 85 MPa holding stress, and a 180 s hold time. Fig. 6.7 shows the cyclic softening and peak strain increase behavior comparison.

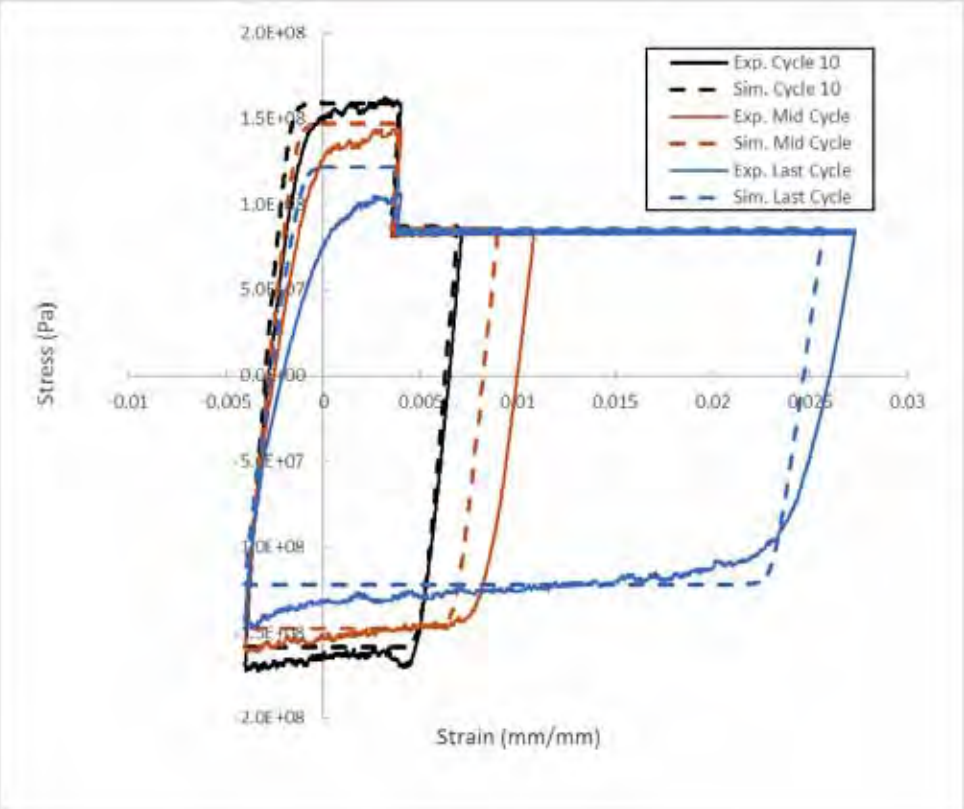

Fig. 6.6 – Stress-strain response for various cycles compared with experiment for a hybrid control test with 0.8% strain range, 85 MPa holding stress, and 180 s hold

(a)

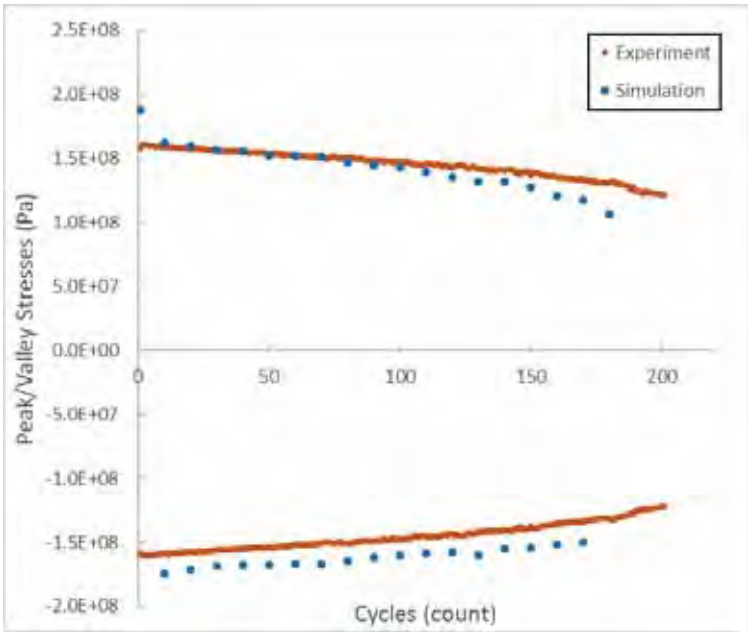

(b)

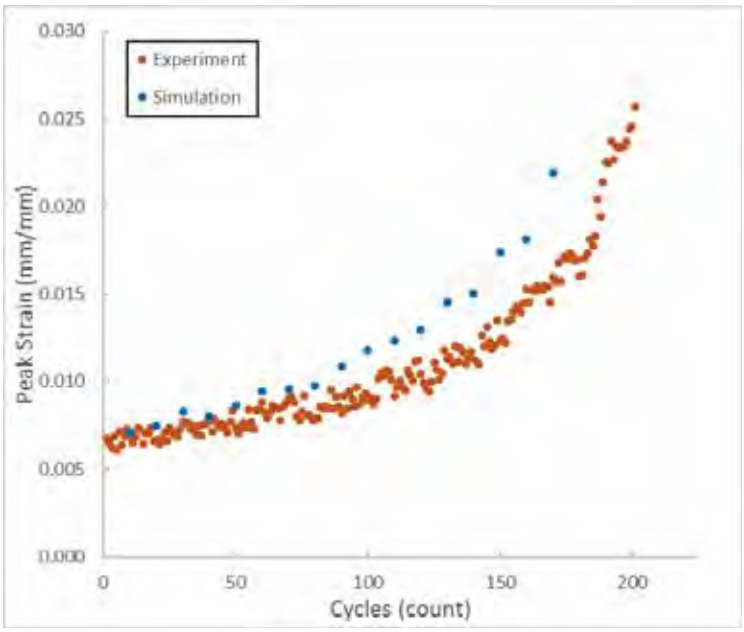

Fig. 6.7 – (a) Cyclic softening and (b) peak strain increase comparison between experiment and simulation.

6.3 CONCLUSION

A unified mechanics model for viscoplastic creep-fatigue deformation analysis and damage accumulation model is proposed. The constitutive law is modified by a damage rate model linked with the dissipation of hysteresis energy through cyclic fatigue deformation and creep deformation. Several major conclusions can be drawn. The constitutive law coupled with damage shows the cyclic softening behavior for both peak stress response and effective Young's modulus; the hysteresis energy related to fatigue deformation shows almost linear variation with respect to the number of cycles, while the hysteresis creep energy shows a power law increasing with respect to the number of cycles; a nonlinear damage accumulation law by taking the power of the fatigue energy and creep energy shows a good correlation with the final failure life. The current testing and simulation results suggest a power of ~1/3 as an estimate for the non-linear damage accumulation law. In general, the proposed methodology shows good agreement with the experimental data for both deformation response and life prediction.

7 Polycrystal Plasticity Modeling of IN 617 Subjected to Cyclic Loading at High Temperature

In this chapter, a crystal plasticity model is developed to idealize the fatigue and creep-fatigue cycles of IN 617 at high temperature environment. The CPFE model that incorporates isothermal deformation behavior of the alloy as well as the large deformation kinematics has been formulated, implemented and validated. The proposed CPFE model includes a new slip resistance evolution law that accounts for the solute-drag creep and can capture the transient softening effects observed under fatigue and creep-fatigue tests. Model parameters in the CPFE model are calibrated by employing a model calibration procedure that is based on Gaussian Process modeling to accelerate the process. Simulations were performed using polycrystal morphologies generated using experimental (i.e., EBSD) data along with the calibrated CPFE model. The simulation predictions were found to be in good agreement with all fatigue and creep-fatigue tests at different strain ranges and hold times. The proposed model, although calibrated for 950 ℃, is expected to apply within a range of temperature between approximately 900-1000 ℃. Within this range, the microstructure of IN 617 is largely free of γ' precipitates with a relatively stable microstructure [117, 72].

7.1 The crystal plasticity model

A comprehensive review of various crystal plasticity models is provided in Roters et al. [141]. Twinning and dislocation slip have been the most studied deformation mechanism in the context of crystal plasticity and implementation into CPFE framework is readily available. Mechanical twinning preferentially occurs in coarse-grained crystalline metals with low symmetry at low temperature and high strain rate [168, 85, 105, 69]. Furthermore, no significant deformation twining has been reported in the experimental literature for alloy 617 at high temperatures. While evidence of dislocation climb of IN 617 at temperatures between 850 and 1050℃ has been reported by Wen [161], it is also pointed out that dislocation glide is still the dominant deformation mechanism. On the other hand, dislocation climb modeling under the context of CPFE has been very recent [88, 112]. In this chapter, a simplifying assumption is made, where all plastic deformation is modeled as a consequence of dislocation glide. Full traction continuity is assumed along each grain boundary (i.e., the modeling is valid up to the onset of damage initiation). The large deformation formulation is based on the framework of Marin and Dawson [119, 118] and a brief overview of this framework is provided herein for completeness. The kinematic theory implemented in the current CPFE model falls within the theory of Taylor [158] and Hill and Rice [93].

Consider a body that occupies the reference domain $\mathbb{B}_0$ that corresponds to the initial state of

the polycrystal microstructure. The current domain is denoted by $\mathbb{B}$ as shown in Fig. 7.1. The motion of the body is described using the deformation map, $\boldsymbol{\phi}(\mathbf{X}, t)$:

$$\mathbf{x} = \boldsymbol{\phi}(\mathbf{X}, t); \quad \mathbf{X} \in \mathbb{B}_{\mathbf{0}}, \ \mathbf{x} \in \mathbb{B} \tag{2}$$

where, $\mathbf{x}$ and $\mathbf{X}$ denote the position vectors in the current and reference (initial) configurations, respectively. The displacement field, $\mathbf{u}(\mathbf{X}, t)$, is then expressed as:

$$\mathbf{u}(\mathbf{X}, t) = \boldsymbol{\phi}(\mathbf{X}, t) - \mathbf{X}; \quad \mathbf{X} \in \mathbb{B}_0 \tag{3}$$

The deformation gradient, $\mathbf{F} = \partial\boldsymbol{\phi}/\partial\mathbf{X}$, is expressed using the classical multiplicative split into elastic ($\mathbf{F}^e$) and plastic ($\mathbf{F}^p$) contributions as:

$$\mathbf{F} = \mathbf{F}^e \cdot \mathbf{F}^p \tag{4}$$

Polar decomposition of the elastic part of the deformation tensor into the left elastic stretch tensor, $\mathbf{V}^e$, and the orthogonal rotation tensor, $\mathbf{R}^e$ (i.e., $\det(\mathbf{R}^e) = 1$ and $\mathbf{R}^{e-1} = \mathbf{R}^{eT}$), allows Eq. (4) to be expanded as:

$$\mathbf{F} = \mathbf{V}^e \cdot \mathbf{F}^*, \quad \mathbf{F}^* = \mathbf{R}^e \cdot \mathbf{F}^p \tag{5}$$

in which, superscripts -1 and T denotes tensor inverse and transpose, respectively. The above decomposition allows the introduction of two intermediate configurations denoted as $\bar{\mathbb{B}}$ and $\widetilde{\mathbb{B}}$ between the original configuration, $\mathbb{B}_0$, and the current configuration, $\mathbb{B}$, as shown in Fig. 7.1. In what follows, an overbar or tilde indicates the value of a variable at the corresponding intermediate configuration. The current formulation operates in the intermediate configuration, $\widetilde{\mathbb{B}}$, obtained by elastically unloading from the current configuration, $\mathbb{B}$. $\mathbf{F}^p$ is related to the dislocations on crystallographic planes and $\mathbf{V}^e$ is a pure elastic stretching of the lattice, both of which do not change the crystal orientation. $\mathbf{R}^e$ defines the rotation and the reorientation of the grains. By this approach, it is straightforward to incorporate crystal elasticity to CPFE. This is in contrast to formulations based on a single intermediate configuration, where the behavior is often idealized as rigid viscoplastic.

Each slip system α is uniquely defined by its Schmid tensor $\mathbf{Z}^\alpha = \mathbf{m}^\alpha \otimes \mathbf{n}^\alpha$, where $\mathbf{n}^\alpha$ and $\mathbf{m}^\alpha$ are the unit vectors normal to the slip plane and along the slip direction, respectively. Since the lattice orientation is affected only by $\mathbf{R}^e$:

$$\bar{\mathbf{n}}^\alpha = \mathbf{n}_0^\alpha; \quad \bar{\mathbf{m}}^\alpha = \mathbf{m}_0^\alpha; \quad \mathbf{n}^\alpha = \tilde{\mathbf{n}}^\alpha; \quad \mathbf{m}^\alpha = \tilde{\mathbf{m}}^\alpha \tag{6}$$

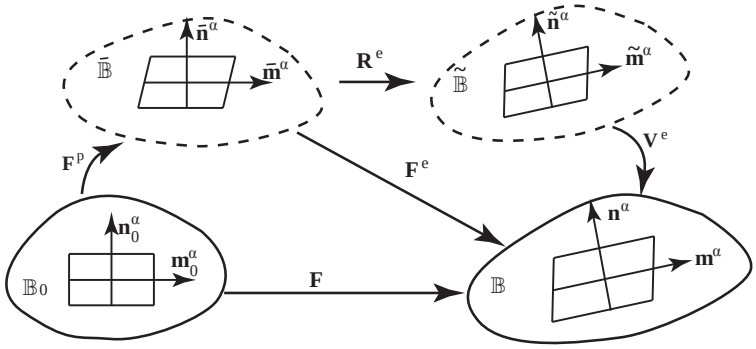

Fig. 7.1: Kinematics of the deformation.

The grain orientation is updated using the rotation tensor $\mathbf{R}^e$:

$$\tilde{\mathbf{n}}^\alpha = \mathbf{R}^e \cdot \bar{\mathbf{n}}^\alpha; \quad \tilde{\mathbf{m}}^\alpha = \mathbf{R}^e \cdot \bar{\mathbf{m}}^\alpha \tag{7}$$

which, describes the texture evolution during the deformation process.

The plastic velocity gradients $\bar{\mathbf{L}}^p$ and $\tilde{\mathbf{L}}^p$ in the intermediate configurations $\bar{\mathbb{B}}$ and $\widetilde{\mathbb{B}}$, respectively, are expressed as:

$$\bar{\mathbf{L}}^p = \dot{\mathbf{F}}^p \cdot \mathbf{F}^{p-1} = \sum_{\alpha=1}^{N} \dot{\gamma}^\alpha \bar{\mathbf{m}}^\alpha \otimes \bar{\mathbf{n}}^\alpha \tag{8}$$

$$\widetilde{\mathbf{L}}^p = \dot{\mathbf{F}}^* \cdot \mathbf{F}^{*-1} = \widetilde{\mathbf{\Omega}}^e + \mathbf{R}^e \cdot \bar{\mathbf{L}}^p \cdot \mathbf{R}^{eT} \tag{9}$$

where, $\widetilde{\mathbf{\Omega}}^e = \dot{\mathbf{R}}^e \cdot \mathbf{R}^{eT}$ denotes the spin of the lattice in configuration $\widetilde{\mathbb{B}}$, and possesses skew symmetry [71]. The velocity gradient $\mathbf{L}$ in the current configuration $\mathbb{B}$ is expressed as:

$$\mathbf{L} = \dot{\mathbf{F}} \cdot \mathbf{F}^{-1} = \dot{\mathbf{V}}^e \cdot \boldsymbol{V}^{e-1} + \boldsymbol{V}^e \cdot \widetilde{\mathbf{L}}^p \cdot \mathbf{V}^{e-1} \tag{10}$$

The velocity gradients $\mathbf{L}$, $\bar{\mathbf{L}}^p$ and $\widetilde{\mathbf{L}}^p$ are decomposed into their symmetric ($\mathbf{D}$, $\bar{\mathbf{D}}^p$, $\widetilde{\mathbf{D}}^p$) and skew ($\mathbf{W}$, $\bar{\mathbf{W}}^p$, $\widetilde{\mathbf{W}}^p$) components as:

$$\mathbf{L} = \mathbf{D} + \mathbf{W}, \quad \bar{\mathbf{L}}^p = \bar{\mathbf{D}}^p + \bar{\mathbf{W}}^p, \quad \widetilde{\mathbf{L}}^p = \widetilde{\mathbf{D}}^p + \widetilde{\mathbf{W}}^p \tag{11}$$

which, together with Eqs. (8) and (9), yields:

$$\bar{\mathbf{D}}^p = \sum_{\alpha=1}^{N} \dot{\gamma} \big(\bar{\mathbf{m}}^\alpha \otimes \bar{\mathbf{n}}^\alpha\big)_S, \quad \bar{\mathbf{W}}^p = \sum_{\alpha=1}^{N} \dot{\gamma} \big(\bar{\mathbf{m}}^\alpha \otimes \bar{\mathbf{n}}^\alpha\big)_A \tag{12}$$

$$\widetilde{\mathbf{D}}^p = \mathbf{R}^e \cdot \bar{\mathbf{D}}^p \cdot \mathbf{R}^e, \quad \widetilde{\mathbf{W}}^p = \widetilde{\mathbf{\Omega}}^e + \mathbf{R}^e \cdot \bar{\mathbf{W}}^p \cdot \mathbf{R}^{eT} \tag{13}$$

where, the subscripts S and A indicate the symmetric and skew (anti-symmetry) components, respectively (i.e., $(\cdot)_S = \big((\cdot) + (\cdot)^T\big)/2$; $(\cdot)_A = \big((\cdot) - (\cdot)^T\big)/2$).

The stress-strain relationship of the lattice is expressed as:

$$\widetilde{\mathbf{S}} = \widetilde{\mathbb{C}} : \widetilde{\mathbf{E}}^e \tag{14}$$

where, $\widetilde{\mathbb{C}}$ is the fourth order anisotropic crystal elasticity tensor, $\widetilde{\mathbf{S}}$ the 2nd Piola-Kirchhoff stress in $\widetilde{\mathbb{B}}$, and $\widetilde{\mathbf{E}}^e$ the Green strain tensor relative to $\widetilde{\mathbb{B}}$, which takes the form:

$$\widetilde{\mathbf{E}}^e = \frac{1}{2}(\mathbf{V}^{eT} \cdot \mathbf{V}^e - \mathbf{I}) \tag{15}$$

in which, $\mathbf{I}$ is the second order identity tensor. $\widetilde{\mathbf{S}}$ relates with the Cauchy stress, $\boldsymbol{\sigma}$, and Kirchhoff stress, $\boldsymbol{\tau}$, in the current configuration through the transformations [71]:

$$\widetilde{\mathbf{S}} = \mathbf{V}^{-e} \cdot \boldsymbol{\tau} \cdot \mathbf{V}^{-eT} = \det(\boldsymbol{V}^e)\mathbf{V}^{-e} \cdot \boldsymbol{\sigma} \cdot \mathbf{V}^{-eT} \tag{16}$$

The elastic lattice strains are generally orders of magnitude less than the plastic strains in many applications of interest, hence the small elastic strains assumption is adopted for simplicity [119, 118]:

$$\mathbf{V}^e = \mathbf{I} + \boldsymbol{\epsilon}^e, \quad ||\boldsymbol{\epsilon}^e|| \ll 1 \tag{17}$$

in which, $\boldsymbol{\epsilon}^e$ denotes elstic strains. Time differentiation and inverse operation yield:

$$\dot{\mathbf{V}}^e = \dot{\boldsymbol{\epsilon}}^e, \;\; \mathbf{V}^{e-1} = \mathbf{I} - \boldsymbol{\epsilon}^e \tag{18}$$

Substituting Eqs. (17) and (18) into Eq. (14)-(16), dropping high order terms of $\boldsymbol{\epsilon}^e$, and neglecting terms such as $(\bullet)\epsilon^e$ and $\epsilon^e(\bullet)$ in comparison to $(\bullet)$, the stress-strain relationship is expressed as:

$$\boldsymbol{\tau} = \widetilde{\mathbb{C}} : \boldsymbol{\epsilon}^e = \det(\mathbf{I} + \boldsymbol{\epsilon}^e)\boldsymbol{\sigma} \tag{19}$$

Following similar procedure and consider Eqs. (8) – (13) (see [118] for more details), the kinematic equation and the elasticity equation are expressed in a simplified form. Box 1 summarizes the system of equations for the CPFE model with the small elastic strain assumption, together with the plasticity relationships, flow rule, evolution equations, Schmid's law and texture evolution equations discussed below.

- Equilibrium:

$$\text{div}\boldsymbol{\sigma} = \mathbf{0}$$

- Boundary conditions.:

$$\boldsymbol{u}(\mathbf{x},t) = \bar{\boldsymbol{u}}(\mathbf{x},t),\ \mathbf{x} \in \Gamma^u;\quad \boldsymbol{\sigma}(\mathbf{x},t)\cdot\mathbf{n} = \bar{\mathbf{t}}(\mathbf{x},t),\ \mathbf{x} \in \Gamma^t$$
$$\Gamma^u \cup \Gamma^t = \partial\mathbb{B}_0,\ \Gamma^u \cap \Gamma^t = \varnothing$$

- Kinematics:

$$\mathbf{W} = \widetilde{\boldsymbol{\Omega}}^e + \widetilde{\mathbf{W}}^p,\ \ \widetilde{\boldsymbol{\Omega}}^e = \dot{\mathbf{R}}^e\mathbf{R}^{eT}$$
$$\mathbf{D} = \widetilde{\mathbf{D}}^p + \dot{\boldsymbol{\epsilon}}^e + \boldsymbol{\epsilon}^e\widetilde{\boldsymbol{\Omega}}^e - \widetilde{\boldsymbol{\Omega}}^e\boldsymbol{\epsilon}^e$$

- Elasticity:

$$\boldsymbol{\tau} = \widetilde{\mathbb{C}} : \boldsymbol{\epsilon}^e;\ \ \boldsymbol{\tau} = \det(\mathbf{I} + \boldsymbol{\epsilon}^e)\boldsymbol{\sigma}$$

- Plasticity:

$$\widetilde{\mathbf{W}}^p = \mathbf{R}^e\bar{\mathbf{W}}^p\mathbf{R}^{eT} = \sum_{\alpha=1}^{N}\dot{\gamma}^\alpha(\widetilde{\mathbf{Z}}^\alpha)_A$$
$$\widetilde{\mathbf{D}}^p = \mathbf{R}^e\bar{\mathbf{D}}^p\boldsymbol{R}^{eT} = \sum_{\alpha=1}^{N}\dot{\gamma}^\alpha(\widetilde{\boldsymbol{Z}}^\alpha)_S$$

- Flow rule:

$$\dot{\gamma}^\alpha = \dot{\gamma}_0\text{exp}\left\{-\frac{F_0}{k\theta}\left\langle 1 - \left\langle\frac{|\tau^\alpha - B^\alpha| - S^\alpha\mu/\mu_0}{\hat{\tau}_0\mu/\mu_0}\right\rangle^p\right\rangle^q\right\}\text{sgn}(\tau^\alpha - B^\alpha)$$

- Schmid's law:

$$\tau^\alpha = \boldsymbol{\tau} : \widetilde{\boldsymbol{Z}}^\alpha;\ \widetilde{\boldsymbol{Z}}^\alpha = \widetilde{\boldsymbol{m}}^\alpha \otimes \widetilde{\boldsymbol{n}}^\alpha$$

- Texture evolution:

$$\widetilde{\mathbf{m}} = \mathbf{R}^e\cdot\bar{\mathbf{m}}^\alpha;\ \ \widetilde{\mathbf{n}} = \mathbf{R}^e\cdot\bar{\mathbf{n}}^\alpha$$

- Evolution equations:

$$\dot{S}^\alpha = \left[h_S - d_D(S^\alpha - \bar{S}^\alpha)\right]|\dot{\gamma}^\alpha| - h_2(S^\alpha - S_0^\alpha)H\left(\dot{\gamma}_{\text{th}} - \textstyle\sum_{\alpha=1}^{n}|\dot{\gamma}^\alpha|\right)$$
$$\dot{B}^\alpha = [h_B - D^\alpha B^\alpha\text{sgn}(\dot{\gamma}^\alpha)]\dot{\gamma}^\alpha$$

Box 1: Summary of the CPFE model.

7.1.1 Flow rule and evolution equations

A number of flow rules have been used to model the kinematics of slip in alloys at high temperature [134, 77, 145, 116]. The one proposed by Busso to idealize the high temperature behavior of nickel-based alloys [77, 78, 115] is adopted in this study:

$$\dot{\gamma}^\alpha = \dot{\gamma}_0\text{exp}\left\{-\frac{F_0}{k\theta}\left\langle 1 - \left\langle\frac{|\tau^\alpha - B^\alpha| - S^\alpha\mu/\mu_0}{\hat{\tau}_0\mu/\mu_0}\right\rangle^p\right\rangle^q\right\}\text{sgn}(\tau^\alpha - B^\alpha) \tag{20}$$

where, k is the Boltzmann constant, θ the temperature in Kelvin, $\dot{\gamma}_0$ the reference shear strain rate, F_0 the activation energy, $\hat{\tau}_0$ the stress at which dislocations can be mobilized without the assistance

of thermal activation. p and q are two fitting parameters, μ and μ_0 the shear moduli at the current temperature and 0 K, respectively, S^α and B^α the slip resistance and backstress in the slip system α, respectively. $\langle\cdot\rangle$ denotes the Macaulay brackets (i.e., $< \cdot >= ((\cdot) + |\cdot|)/2$), sgn$(\cdot)$ is the sign function.

The starting point for the evolution equations for the slip resistance (S^α) and the backstress (B^α) for a nickel based alloy is [78, 115]:

$$\dot{S}^\alpha = \left[h_S - d_D(S^\alpha - S_0^\alpha)\right]|\dot{\gamma}^\alpha| \tag{21}$$

$$\dot{B}^\alpha = [h_B - D^\alpha B^\alpha \text{sgn}(\dot{\gamma}^\alpha)]\dot{\gamma}^\alpha \tag{22}$$

where, S_0^α is the initial slip resistance for slip system α, h_S and d_D are the hardening and dynamic recovery parameters for the slip resistance evolution; h_B and D^α are the hardening and dynamic recovery parameters for the backstress evolution, and D^α is expressed as [115]:

$$D^\alpha = \frac{h_B \mu_0}{S^\alpha}\left\{\frac{\mu_0'}{f} - \mu\right\}^{-1} \tag{23}$$

in which, μ_0' is the local slip shear modulus at 0 K and f is a parameter that accounts for the coupling between the internal slip variables as well as the statistical effects.

The slip evolution laws described in Eqs. (21) and (22) have been used to describe the hardening behavior of nickel-based alloys at different temperatures (see [134, 77, 115]). Fully reversed strain-controlled low cycle fatigue and creep-fatigue tests of IN 617 (with strain profile schematically illustrated in Fig. 7.2) were conducted at total strain ranges of 0.6–2.0% at 950℃. A distinct pattern of stress-strain behavior is observed under high-temperature fatigue and creep-fatigue loading (see Fig. 7.3), featured by: (1) an initial stress drop in the first cycle for both fatigue and creep-fatigue tests; (2) re-emergence of the softening behavior in creep-fatigue tests upon reloading (compression) following a strain hold, which is observed in all cycles until crack initiation. The evolution equations in Eqs. (21) and (22) do not capture this softening behavior.

The formation of an initial peak followed by an exponential decrease to a stable flow stress in IN 617 at high temperatures has been attributed to the solute-drag creep deformation mechanism [164]. Similar behavior has been observed in other alloys (e.g., class I and class A aluminum alloys) that exhibit solute-drag creep at elevated temperatures ([146, 157, 79]). Under pure fatigue, the phenomenon is restricted to the first cycle, whereas under creep-fatigue loading, the transient softening prior to steady state flow is persistent.

While the mechanism of solute-drag creep is known [157], its recurrence under creep-fatigue

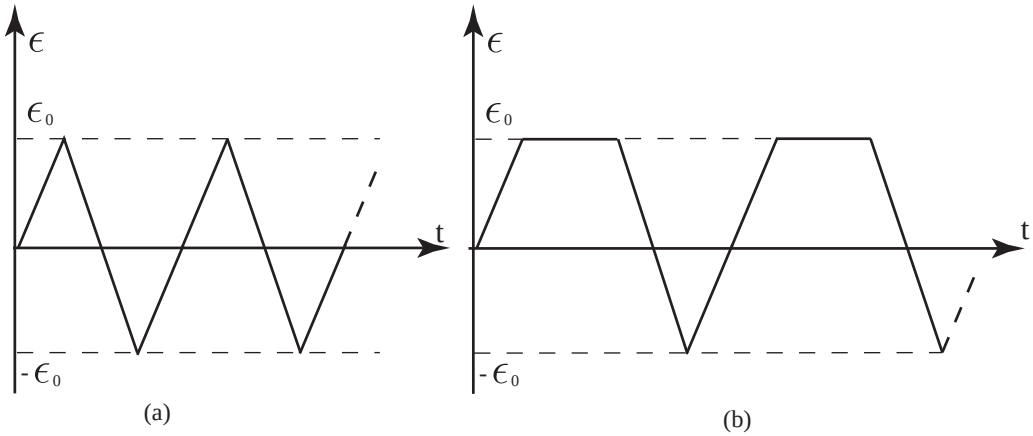

Fig. 7.2: Strain profiles: (a) fatigue test; (b) creep-fatigue test

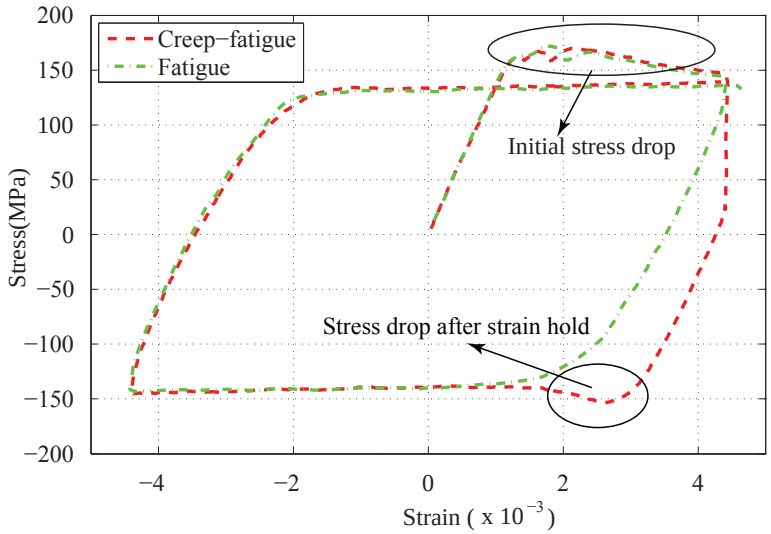

Fig. 7.3: Stress drop observed in the stress-strain curve.

loading has not been studied in detail to the best of the authors' knowledge. At elevated temperature and applied stress, the solutes hinder dislocation motion resulting in relatively high resistance to plastic flow. At a threshold stress, the dislocations overcome the energy barrier and begin dragging solute atoms, which consequently reduces the flow stress to a steady state. Under sudden load reversal, those solute atoms already dragged out of their equilibrium state do not contribute to the extra resistance observed in the initial loading. When subjected to a strain-hold with sufficiently long hold time, solutes return to an energetically minimum state. Hence, upon loading reversal, they contribute to added transient resistance to flow.

We model the above interactions by a new evolutsion law for the slip resistance given as:

$$\dot{S}^{\alpha} = \left[h_S - d_D(S^{\alpha} - \bar{S}^{\alpha})\right]|\dot{\gamma}^{\alpha}| - h_2(S^{\alpha} - S_0^{\alpha})H\left(\dot{\gamma}_{\text{th}} - \sum_{\alpha=1}^{n}|\dot{\gamma}^{\alpha}|\right) \tag{24}$$

where, $\dot{\gamma}_{\text{th}}$ is the threshold rate for static recovery, h_2 the rate of static recovery parameter, $\bar{S}^{\alpha}$ the steady state flow strength parameter. $H(\cdot)$ denotes the Heaviside function. The first part of the slip resistance evolution includes the steady state flow strength parameter, $\bar{S}^{\alpha}$, which is typically lower than S_0^{α} - the "initial" slip resistance. The initial slip resistance refers to the energetic configuration with stationary solutes prior to the onset of drag, and corresponds to the threshold stress mentioned above. The second part of the slip resistance evolution accounts for the recovery of strain softening in the form of static recovery. In the present model, the recovery initiation is possible only when dislocation motion reduces significantly, which is a necessary condition to stop the drag process. Considering the Orowan equation:

$$\dot{\gamma}^{\alpha} = \rho_M^{\alpha} b v^{\alpha} \tag{25}$$

in which, v^{α} is the average velocity of the mobile dislocations, ρ_M^{α} the density of mobile dislocations and b the length of Burgers vector. We employ the proportionality between the diffusion velocity and the slip rate in Eq. (25) to define the recovery term. When magnitude of slip (at all slip systems) drops below a threshold rate, $\dot{\gamma}_{\text{th}}$, static recovery initiates. The rate of recovery is controlled by h_2. At the asymptotic limit, the slip system strength reaches the initial slip system strength (i.e., configuration indistinguishable from the initial state).

The competition between the first and the second components of the strength evolution equation, which respectively forces a reduction and increase in the slip resistance is explained in the context of a simple example. Consider an arbitrary slip system, α, is subjected to a constant slip rate $\dot{\gamma}^{\alpha} = \dot{\bar{\gamma}} > \dot{\gamma}_{\text{th}}$ (with slip in all other slip systems constrained) until time t_1, followed by zero slip rate $\dot{\gamma}^{\alpha} = 0$ between times t_1 and t_2. The example is set to mimic loading followed by a subsequent strain hold. t_1 and t_2 are sufficiently long such that dynamic and static recovery processes are nearly

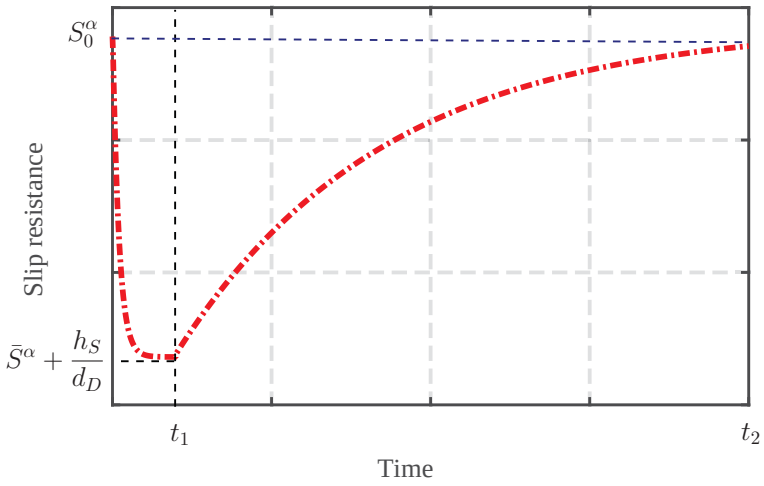

Fig. 7.4: Evolution of slip resistance under the prescribed slip rate.

completed, respectively. Under this prescribed loading condition, the evolution of slip resistance can be evaluated in closed form from Eq. (24) as:

$$S^\alpha = \begin{cases} \bar{S}^\alpha + \frac{1}{d_D}\left\{hs - [hs - d_D(S_0^\alpha - \bar{S}^\alpha)]\exp(-d_D|\dot{\gamma}_0^\alpha|t)\right\} & 0 \le t \le t_1 \\ S_0^\alpha - (S_0^\alpha - \bar{S}_\alpha - \frac{h_S}{d_D})\exp(-h_2(t-t_1)) & t_1 \le t \le t_2 \end{cases} \tag{26}$$

Equation (26) plotted in Fig. 7.4 shows an exponential decay of the slip resistance towards $\bar{S}^\alpha + h_S/dD$ followed by a recovery towards its initial value S_0^α.

7.1.2 Numerical smoothing for convergent stress update

Box 1 summarizes the system of nonlinear equations, which describes the mechanical response based on the crystal plasticity model described above. This system is discretized over the domain of a characteristic microstructure and evaluated numerically using the finite element method. The stress update at a material point within a grain is performed using an operator split method with a two-level staggering scheme as described in Refs. [119, 118]. In the first level, a Newton-Raphson method is used to solve for stress ($\boldsymbol{\tau}$), while rotations ($\boldsymbol{R}^e$), slip resistances (S^α) and backstress (B^α) are kept constant; In the second level, rotations, slip resistances and backstress are updated for a fixed stress calculated at the first level. Iterations between the two levels continue until changes in the cardinal unknowns (i.e., $\boldsymbol{\tau}$, S^α and B^α) within the increment drop below a threshold value (relative change of the norm is less than 1.0×10^{-4} in the current study). Convergence of the polycrystal plasticity equations summarized in Box 1 using the algorithms defined above is not guaranteed due to the discontinuity in the Jacobian introduced by the presence of Macaulay brackets in the

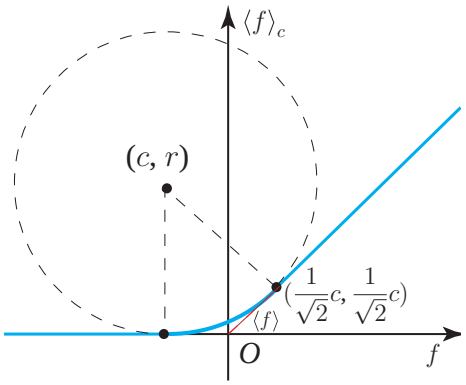

Fig. 7.5: "Smoothed" Macaulay bracket to eliminate Jacobian discontinuity and improve stress-update convergence.

flow rule. This discontinuity typically leads to the oscillation of the iterations without convergence. We employ a simple regularization of this problem, by replacing the Macaulay brackets with a C^1 continuous approximation. Let $\langle f\rangle_c$ be a C^1 continuous functional defined as (Fig. 7.5):

$$\langle f\rangle_c = \begin{cases} f & f > \frac{1}{\sqrt{2}}c \\ r - \sqrt{r^2 - f^2 + 2fc} & -c \le f \le \frac{1}{\sqrt{2}}c \\ 0 & f < -c \end{cases} \tag{27}$$

where, $r = (\tan\dfrac{3\pi}{8})c$ is the radius of the circle that is used for smoothing. At the limit of $c \to 0$, $\langle f\rangle_c$ approaches $\langle f\rangle$ and c constitutes the numerical regularization parameter. The Macaulay bracket in the slip evolution equation is then replaced with the continuous approximation. In the numerical simulations discussed below c is set to 0.001. By this approach, the system Jacobian remains well-defined and the numerical scheme is convergent for sufficiently small time step size. We note that the convergence is sub-quadratic due to the use of operator split in the evolution of the constitutive equations.

7.2 Model preparation

IN 617 is a solid solution strengthened alloy with face center cubic (FCC) lattice structure, with 12 octahedral $\{111\}\langle 110\rangle$ slip systems. In precipitate strengthened nickel alloys where the γ-γ' phases coexist, the six cubic slip systems $\{100\}\langle 110\rangle$ may also contribute to deformation at high homologous temperatures and high resolved stress (in γ' phase) [145]. γ' phase becomes unstable above 650℃ [117, 72]. At temperatures above approximately 750 ℃, the microstructure of IN 617 is largely free of γ' precipitates, hence the cubic slip systems remain inactive. Figure 7.6(b) shows

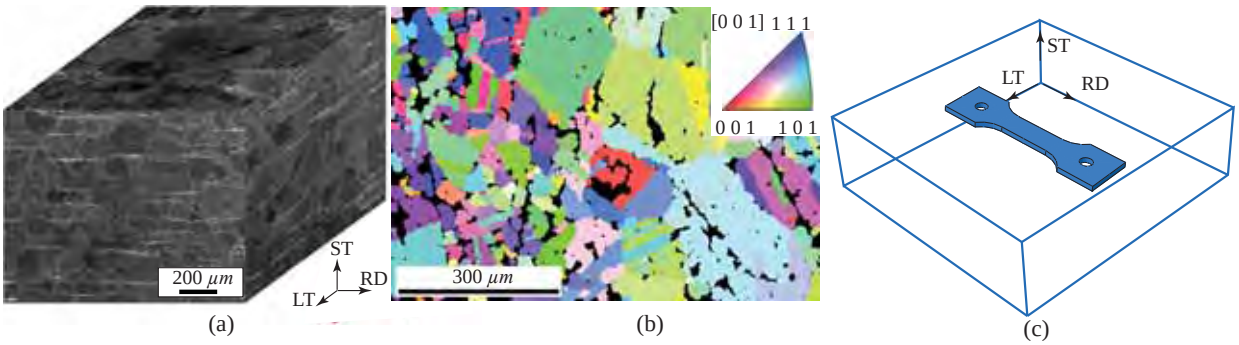

Fig. 7.6: IN 617 microstructure: (a) 3-D etched microstructure (reproduced from Ref. [122]; (b) [0 0 1] inverse pole figure (IPF) EBSD map on a short traverse plane of as received IN 617 sample; (c) specimen configuration.

Table 7.1: Composition in percentage weight of the IN 617 specimen used in this study.

	Ni	C	Cr	Co	Mo	Fe
ASTM standard	$\geq$ 44.5	0.05-0.15	20.0-24.0	10.0-15.0	8.0-10.0	$\leq$ 3.0
This study	bal	0.05	22.2	11.6	8.6	1.6
	Al	Ti	Si	Cu	Mn	S
ASTM standard	0.8-1.5	$\leq$ 0.6	$\leq$ 1.0	$\leq$ 0.5	$\leq$ 1.0	$\leq$ 0.015
This study	1.1	0.4	0.1	0.04	0.1	$\leq$ 0.02

a 2-D EBSD scan of IN 617. The microstructure exhibits distinguishable coarse and fine grains and random initial orientations as shown in Fig. 7.6(b). Similar observations have been previously made [122, 123, 121]. Annealing twins are evident in the as-received samples and deformation twinning has not been observed and not considered in the simulations. Annealing twins could serve as sites of strain localization and damage initiation in Ni-based alloys subjected to fatigue loading conditions [153, 154]. The focus of the current investigations is on modeling of the cyclic response prior to the onset of significant microstructural damage, and the presence of annealing twins are not taken into account in the microstructures employed in this study. The microstructure images (Fig. 7.6(a)) also show significant amount of carbides (mainly Mo-rich, Cr-rich carbides and Ti-rich carbonitrides) present within and at grain boundaries. While the presence of carbides may affect the fatigue and creep-fatigue damage, they are not explicitly modeled in the simulation of the cyclic behavior.

All experimental data used in this study are from specimens machined from the annealed plate produced by ThyssenKrupp VDM and solution annealed at 1175 ℃ [165]. The compositions of the specimens are given in Table 7.1 along with the specified ranges in ASTM Standard B168-08 for comparison. The long axis of the specimen is aligned with the rolling direction as schematically demonstrated in Fig. 7.6(c).

Fully reversed strain-controlled low cycle fatigue and creep-fatigue tests were conducted at total

Table 7.2: Summary of all tests studied.

Specimen	Temperature(℃)	Strain rate ($/s$)	Total Strain (%)	Hold time (s)
B-14	950	0.001	0.6	0
E-11	950	0.001	1.0	0
J-1	950	0.001	2.0	0
A-14	950	0.001	0.6	600
416-18	950	0.001	0.6	1800
B-16	950	0.001	0.6	180
F-5	950	0.001	1.0	180
A-13	950	0.001	1.0	600
E-6	950	0.001	1.0	1800
E-10	950	0.001	1.0	9000

strain ranges from 0.6-2.0% at 950℃, all with constant strain rate of 1.0×10^{-3}/s. One cycle was defined as the combination of a tension and compression load reversal using a symmetric triangular waveform. During the initial part of most experiments, several cycles with incrementally increasing strain values were used prior to reaching the target strain level to avoid overshooting the target strain, which can occur at high temperature in the presence of plastic deformation. Table 7.2 summarizes the experiments used in this study.

7.2.1 Microstructure reconstruction and meshing

Microstructure generation of IN 617 is conducted using the DREAM.3D software [90], which is capable of creating synthetic microstructures using experimentally determined microstructure morphological and crystallographic statistics. Grain size distribution computed from microstructure observations are employed to generate the synthetic microstructures, as well as their geometry and surface mesh information (see Fig. 7.7(a)). To accurately quantify the bi-modal grain size distribution observed in IN 617, the fine and coarse grains are treated as separate phases during the reconstruction process. The volume fractions of the fine and coarse grains are 75.61% and 24.39%, respectively. Figure 7.8 shows the log-normal distributions fitted to the experimentally observed distributions for both the fine and coarse grains. The Parallelized Polycrystal Mesher (PPM) software developed by Cerrone et al [81] is then used to build a volume mesh of the microstructures. Figure 7.7(b) shows the volume mesh generated using the above-mentioned process, which provides statically equivalent microstructures as the specimen.

7.2.2 Determination of the simulation domain size

In order to identify the appropriate size of the simulation domain that provides converged CPFE simulation results with reasonable computational cost, a parametric study was conducted. The

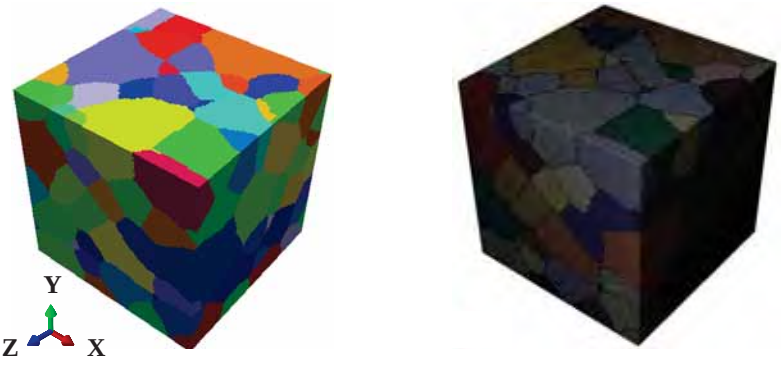

Fig. 7.7: Mistructure genertion and meshing: (a) microstructure generated in DREAM.3D; (b) volume mesh.

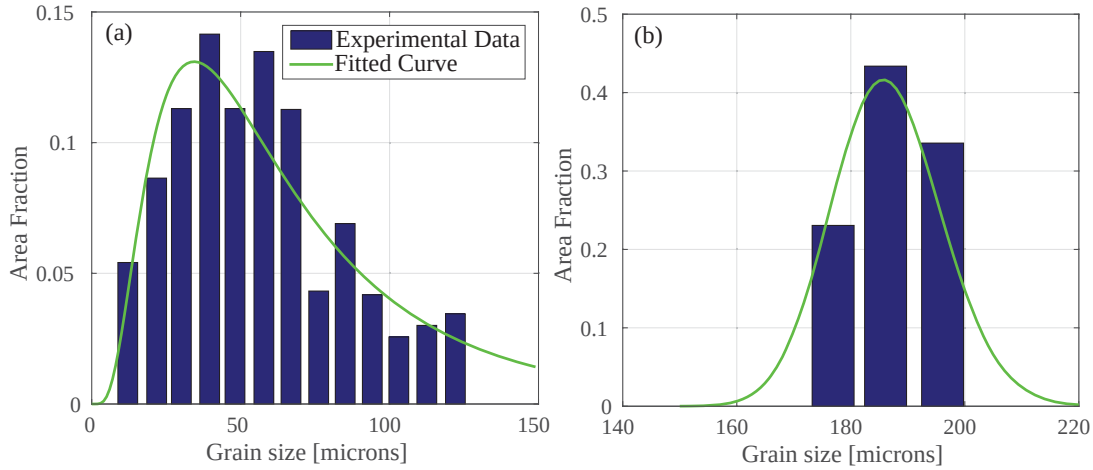

Fig. 7.8: Fitted log-normal grain size distribution: (a) fine grains; (b) coarse grains.

parametric study was performed with respect to the number of grains resolved within the simulated microstructure. Three different cubic simulation cells with edge length of 300 μm, 360 μm and 400 μm are constructed for this purpose. The discretization of the simulation cells are as shown in Fig. 7.9(b)-(d). The boundary conditions are schematically shown in Fig. 7.9(a). The three simulation cells contain 98, 140 and 243 grains, and are discretized using four-noded tetrahedra with 67,689, 113,986 and 243,801 elements, respectively. Each grain is assigned a random initial orientation. The applied strain follows a creep-fatigue test path with 1.0% strain range (R ratio equals to 1), 180 s hold time at the maximum tension and strain rate of 0.001/s.

Figure 7.10 shows the stress-strain responses obtained using the three simulation cells. While the three curves matched well during the elastic region and the stress hold, a noticeable gap between the 98-grain cell and the others is observed after yielding. This observation indicates 98-grain cell is not representative of a converged response while the simulation cell with 140 and 243 grains are sufficiently similar. We further investigate the convergence of the local stress distribution within

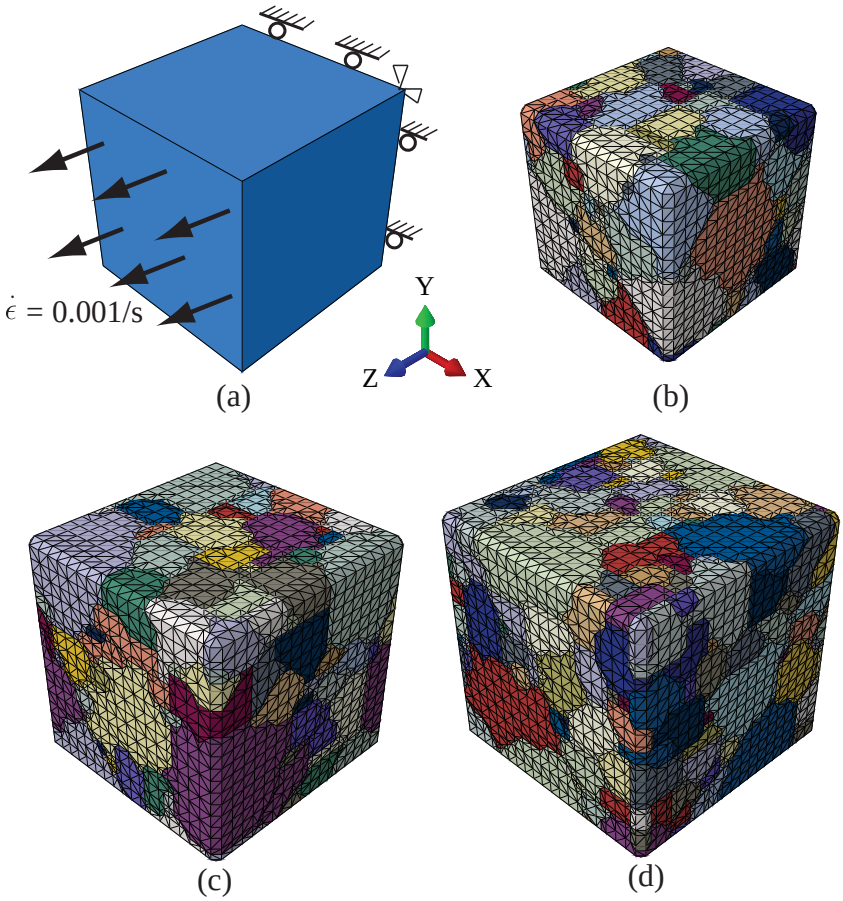

Fig. 7.9: (a) Schematic illustration of the boundary conditions and loading used in the microstructure size determination study; (b)-(d) Finite element meshes of the 98-, 140- and 243-grain microstructures.

five microstructures, including a 504- and 769-grain cells (microstructure geometries not plotted for brevity). The stress histograms of the cells at the beginning of the strain hold are plotted in Fig. 7.11. With the exception of the 98-grain cell, the stress distributions with the remainder of the cells are similar with slight variability. The CPFE simulations below are therefore performed using the 140-grain cell. The simulation cell is assigned with random initial texture with the {111} pole figure shown in Fig. 7.12.

7.2.3 Model parameter calibration

The full set of parameter values of the crystal plasticity model for IN 617 described above is not generally available in the literature. Those model parameters not available in the literature are therefore inferred from experimental data. The general calibration approach used in this study is based on optimization through the minimization of an objective function. Let Θ denote the set of all unknown parameters of the model. In the current study, 19 parameters define the model as

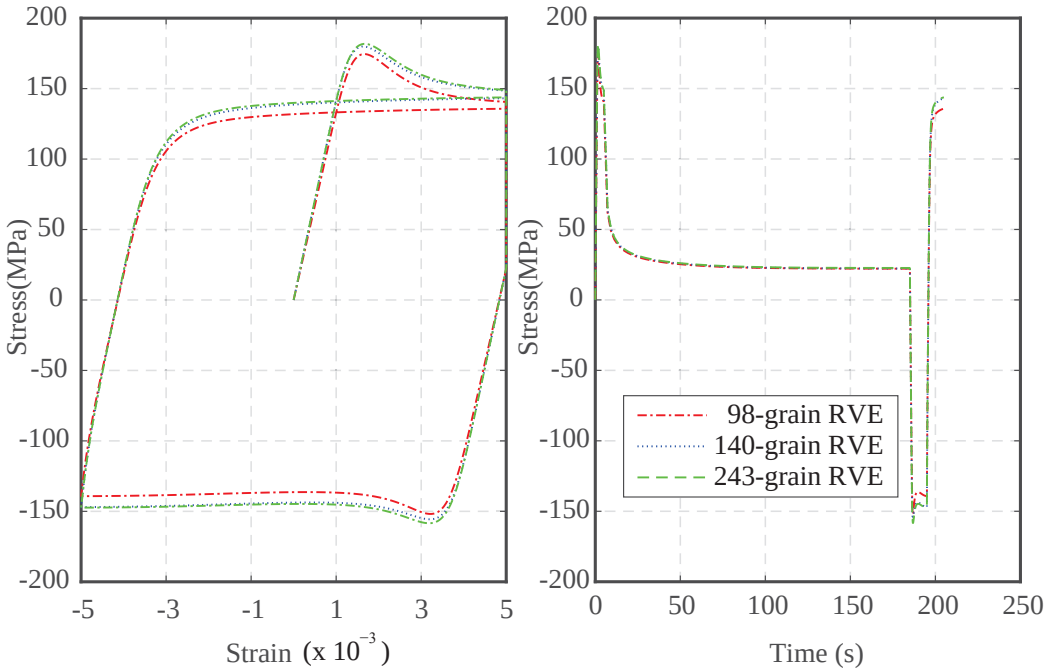

Fig. 7.10: Convergence study of microstructure size: (a) stress-strain response; (b) stress-time response.

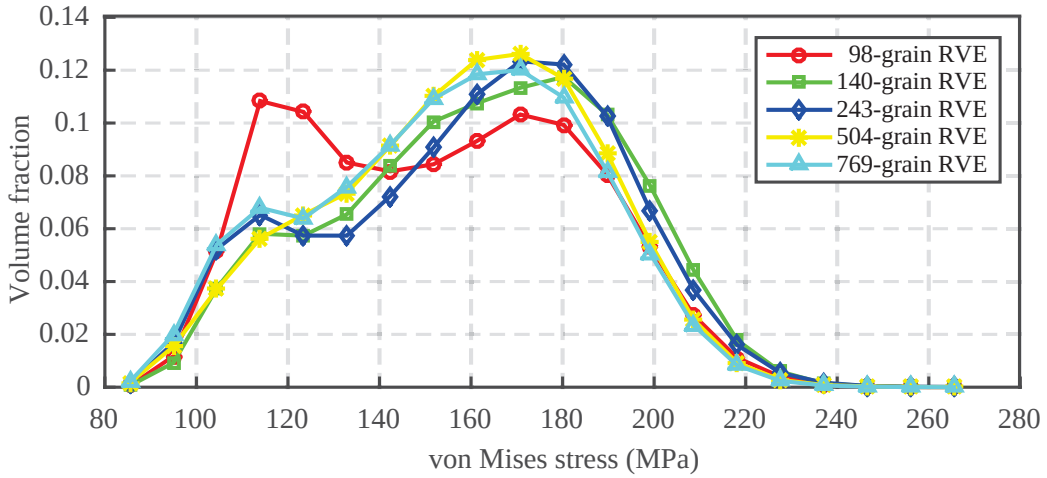

Fig. 7.11: von-Mises stress histogram of different RVEs.

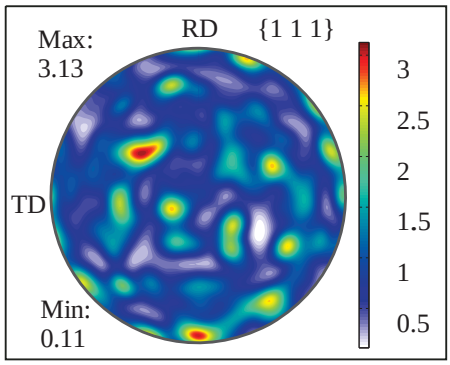

Fig. 7.12: {1 1 1} pole figure of the initial texture of the 140-grain microstructure.

indicated in Table 7.3. Consider an arbitrary but fixed subset of model parameters, $\hat{\Theta} \subset \Theta$. Each parameter within the parameter set, $\Theta_i \in \Theta$, lies within a range of values $\Theta_i \in [\Theta_i^l, \Theta_i^u]$, where Θ_i^l and Θ_i^u denote the lower and upper bound values of the parameter Θ_i, respectively. These bounds are typically chosen based on physical arguments, (e.g., magnitude of relative yield stress or strain hardening). The optimal set of parameters is achieved by solving the following equation:

$$\hat{\Theta}^{\text{opt}} = \arg\min \left\{ \sum_{i=1}^{M} w_i^t \left[\sum_{j=1}^{N_i} \left(\frac{R_{i,j}^{\text{exp}} - R_{i,j}^{\text{sim}}(\mathbf{X}_k)}{R_{i,j}^{\text{exp}}} \right)^2 \right], \hat{\Theta} \in [\hat{\Theta}^l, \hat{\Theta}^u] \right\} \tag{28}$$

in which, M is the total number of experiments used in the calibration process; w_i^t is the weight factor for the i^{th} test used to increase or reduce parameter sensitivity; N_i denotes the number of datasets obtained from test i (e.g., stress-strain, stress time histories); $R_{i,j}^{\text{exp}}$ and $R_{i,j}^{\text{sim}}$ are respectively the experimental and the simulated datasets. Equation (28) is written for a subset of parameters only and executed multiple times to calibrate all parameters, since the optimization of the full set of 19 parameters together is computationally prohibitive. At the beginning of the calibration process, each parameter is assigned an initial value, Θ_i^0. During the calibration of the parameter subset $\hat{\Theta}$, all parameters (not being calibrated) are either set to their initial values, or set to their calibrated values at an earlier parameter subset calibration. We further note that a very comprehensive dataset is necessary to uniquely identify all parameters, and experimental data is often quite limited. We therefore seek a set of optimal and physically reasonable parameters that accurately captures the available calibration data. The calibration is performed by executing the following steps: (1) Determine search range for each parameter (i.e., Θ_i^l and Θ_i^u). (2) Sample parameter subspace and execute CPFE simulations to compute $R_{i,j}^{sim}$. (3) Fit a surrogate model that approximates the response surface (i.e., R_{ij}^{sim}). (4) Solve Eq. (28) to obtain optimal parameters set $\hat{\Theta}^{\text{opt}}$. (5) Verify calibration accuracy by running CPFE simulation with $\hat{\Theta}^{\text{opt}}$.

Two out of the 19 parameters are set to fixed values and not calibrated, while three of them are dependent (i.e., can be computed from the remaining 16). The optimizations are therefore performed for 14 parameters only. f is set to 0.36 as suggested by Lin et al. [115] since its effect on the simulation results are found to be small. The lattice friction stress at 0 K, $\hat{\tau}_0$, in Eq. (20) is obtained by resolving the difference between the yield strength (at 0.2% offset strain) at 0 K, $\sigma^0_{0.2}$, and the temperature approaching infinity, $\sigma^\infty_{0.2}$ (i.e., see [77]):

$$\hat{\tau}_0 = \frac{\sigma^0_{0.2} - \sigma^\infty_{0.2}}{2} \tag{29}$$

with $\sigma^0_{0.2}$ and $\sigma^\infty_{0.2}$ estimated from Ref. [104], giving $\hat{\tau}_0 = 268.2$ MPa as a constant. This procedure has been previously employed to calibrate lattice friction stress [77]. A fixed anisotropy factor of $A = 2C_{44}/(C_{11} - C_{12}) = 2.5$ which is equal to that of pure nickel is enforced [135], decreasing the number of independent elastic parameters to two. The local shear modulus at 0 K, μ'_0, is given by Ref. [77] as:

$$\mu'_0 = \frac{C_{11} - C_{12}}{2} \tag{30}$$

and the shear modulus μ is equal to the elastic parameter C_{44}.

The search ranges for the remaining 14 parameters of the polycrystal model are established through the literature search on crystal plasticity modeling of similar alloys, and preliminary parametric analysis performed for each parameter. The elastic properties for pure nickel are used as the initial value of the elastic parameter (i.e., $C_{11} = 250$ GPa, $C_{12} = 151$ GPa, $C_{44} = 123$ GPa [135]). By referring to elastic parameters of other nickel-based alloys [145, 115] and the observation that bulk moduli of alloy at 950℃ is around 140 GPa, the ranges of C_{11} and C_{12} are set to be $150 \leq C_{11} \leq 280$ GPa and $30 \leq C_{12} \leq 160$ GPa, respectively. The activation energy F_0 for various nickel-based alloys was taken to be around 300 KJ/mol (4.98×10^{-19} J) in Refs. [145, 115, 78], which serves as the initial value of F_0 with the range set to be $4.5 \times 10^{-19} \leq F_0 \leq 5.5 \times 10^{-19}$J. The initial values for p and q are chosen to be $p = 0.31, q = 1.8$ [115] with recommendation as $0 \leq p \leq 1$ and $1 \leq q \leq 2$ in general by Kothari and Anand [107], while preliminary simulations further constrain them as $0.1 \leq p \leq 0.4$ and $1.5 \leq q \leq 2$. The initial values and ranges of the other parameters are provided in Table 7.3. The initial values used to initiate the optimization process that provided the global minimum are reported in the table.

Since the computational cost of CPFE simulations is high, it is computationally too costly to evaluate the minimization process using CPFE analysis as the forward solver. We rely on a surrogate model (i.e., Gaussian Process model [138]) to approximate the CPFE simulation for calibration purposes. GP model is a variant of a radial basis function built on Gaussian kernels and provides

Table 7.3: Summary of model parameters. (For fixed parameters, only initial value are provided; for dependent parameters, only dependency and calibrated value are provided.)

Parameter	Initial value	Lower bound	Upper bound	Calibrated value	Reference
C_{11} (GPa)	250	150	280	170.64	[135, 145, 115]
C_{12} (GPa)	151	30	160	108.39	[135, 145, 115]
$\dot{\gamma}_0$ (s^{-1})	5×10^{-3}	5×10^{-4}	3×10^{-2}	1.44×10^{-3}	[115]
F_0 (J)	4.98×10^{-19}	4.5×10^{-19}	5.5×10^{-19}	5.148×10^{-19}	[115, 145, 78]
μ_0 (GPa)	200	180	300	265.33	[115, 145, 78]
p	0.3	0.1	0.4	0.181	[107, 115]
q	1.8	1.5	2	1.633	[107, 115]
h_S (MPa)	2000	100	10000	397.73	[115, 78]
d_D (MPa)	100	1000	10000	5073.62	[115, 78]
S_0^α(MPa)	200	50	320	143.41	[115, 78]
$\bar{S}^\alpha$ (MPa)	200	20	S_0^α	18.03	-
h_B (MPa)	5000	10	10000	104.31	[115]
h_2 (MPa)	0	0	0.2	0.015	-
$\dot{\gamma}_{th}$ (s^{-1})	0	0	1×10^{-4}	1×10^{-6}	-
C_{44} (MPa)	$1.25(C_{11} - C_{12})$	-	-	77.82	[135]
μ (GPa)	$1.25(C_{11} - C_{12})$	-	-	77.82	[77]
μ_0' (GPa)	$0.5(C_{11} - C_{12})$	-	-	31.13	[77]
$\hat{\tau}_0$ (MPa)	268.2	-	-	-	[77, 104]
f	0.36	-	-	-	[115]

the fast transform function between the input (parameter set) and output ($R_{i,j}^{\text{sim}}$). The GP model is "trained" using a series of simulations using the CPFE. We employed Latin Hypercube sampling to sample the search space bounded by the parameter ranges. The optimization is performed using a constrained nonlinear multi-variable solver [136], where the objective function evaluations are performed using the GP models [74]. In order to ensure that the global minimum is achieved within the chosen parameter ranges, The optimization process is repeated several times with random initial parameter values. The final step consists of running a CPFE simulation, with optimal parameter set to assess accuracy. If accuracy is deemed insufficient, the GP model is retrained with denser sampling around the optimal point within the parameter space. The optimization procedure is repeated with retrained GP model.

In this study, the calibration is performed for elastic, monotonic and cyclic response in order to limit the number of unknowns (i.e., dimension of parameter space). Since the fatigue and creep-fatigue tests provide the same response of the elastic and monotonic case, only one test (F-5) is used for calibration while a fatigue and creep-fatigue (F-5 and J-1) are used during the cyclic calibration process. In the elastic calibration process, bulk Young's modulus is taken to be $E = 141$ GPa according to the experimental data while Poisson's ratio of the bulk material is reported to

be 0.3 at 950℃. The number of variables to be calibrated is equal to the number of properties, leading elastic calibration to a well-posed and unique optimization problem. (i.e., $\mathbf{X}_1 = \{C_{11}, C_{12}\}$, $\mathbf{R}_1 = \{E, \nu\}$).

In the monotonic calibration process, the softening part of the stress-strain curves are not considered at first while the slip resistance and backstress evolution are turned off (i.e., set initial value temporarily as: $h_S = 0$, $d_D = 0$, h_B=0, $h_2 = 0$) in the simulation. $R_{1,j}$ is the j^{th} data point out of the total N_1 data points selected from the tension part of the stress-strain curve with the stress drop region eliminated, while $\mathbf{X}_2 = \{F_0, S_0^\alpha, \mu_0\}$ and $\mathbf{X}_3 = \{S_0^\alpha, \dot{\gamma}_0, p, q\}$ are calibrated successively. Then another set of selected data points from the tension part of the stress-strain curve that mainly characterizes the initial yield stress, the stress drop speed and the stabilized flow stress are used in the objective function while the parameters set is chosen as $\mathbf{X}_4 = \{\bar{S}^\alpha, h_S, d_D, h_B\}$ with the static recovery term turned off (i.e., set initial value temporarily as: $h_2 = 0$).

In the cyclic calibration process, both fatigue test J-1 and creep-fatigue test F-5 are used to define the objective function. Data points that reflect the relaxation, yielding stress at compression, softening after the strain hold in the creep-fatigue test and hardening profile are selected while $\mathbf{X}_5 = \{p, q, \dot{\gamma}_0\ , h_2, \dot{\gamma}_{\text{th}}\}$ are used to match hysteresis response for both the fatigue and creep-fatigue tests. The final calibrated parameters are listed in Table 7.3, while the simulation results together with corresponding experimental tests are plotted in Fig. 7.13. It can be seen that the calibrated parameters can capture the stress-strain and stress-time response for both fatigue test and creep-fatigue tests with good accuracy. Their capability to predict other fatigue and creep-fatigue testes with different strain ranges and hold times is further validated next.

The primary challenges in the proposed optimization strategy, particularly for generalizing beyond the current study, are the identification of the parameter ranges and parameter sensitivity used in the selection of parameter subsets. The sensitivity analysis, which identifies the parameters with similar sensitivity (i.e., the selected parameter subset) to the corresponding experimental data used to calibrate them, depends on the chosen parameter ranges. In the current study the parameter ranges were identified based on a parametric study and values previously reported in the literature as discussed above. These challenges exist because of the relatively large number of parameters to be identified, and because the experiments are performed at the bulk scale to calibrate parameters defined at the grain scale.

7.3 Validation and analysis of microstructural response

The calibrated parameters are further validated by running CPFE simulations to compare the first cycle response with experimental data of the remaining tests. As illustrated in Table 7.2, the tests

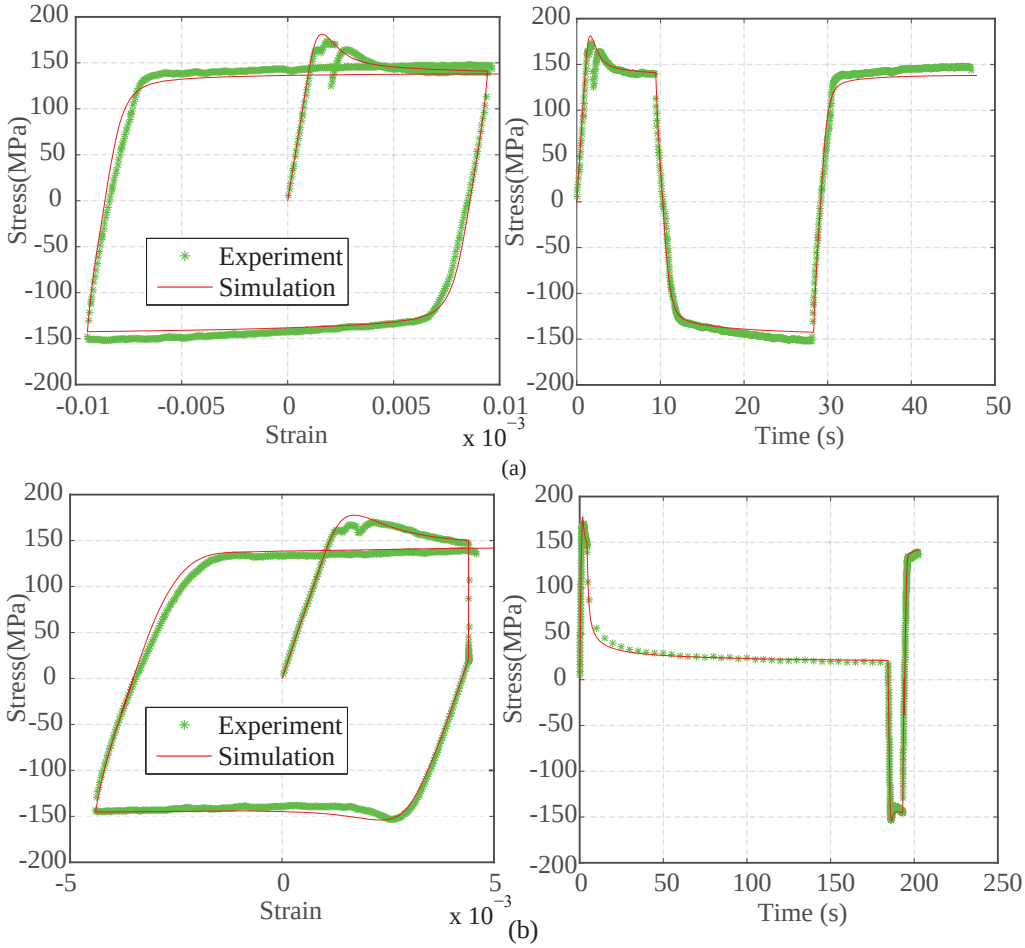

Fig. 7.13: Comparison of simulation results using the calibrated parameters with the two experiment tests used for calibration: (a) fatigue test J-1; (b) creep-fatigue test F-5.

were performed using various strain ranges and hold times beyond the calibration regime. The comparisons are first focused on the first cycle response. A multiple-cycle analysis and discussion is presented next.

7.3.1 First cycle response

Since the transient stress relaxation phenomenon is most prominent in the first cycle, particularly when subjected to fatigue loading, we first investigate the predictive capability of the proposed model in capturing the hysteresis behavior of the first cycle. In this section, we also provide a brief analysis of the evolution of the hysteresis behavior through the cycles and an investigation of the evolution of the stress state within the microstructure.

Figure 7.14 shows the first cycle responses of fatigue tests B-14 and E-11, respectively. The creep-fatigue tests B-16, A-14 and A-13 are shown in Fig. 7.15 while creep-fatigue tests 416-18, E-6 and E-10 are shown in Fig. 7.16. The applied strain ranges in B-16, A-14 and 416-18 are small enough such that the stress softening behavior is not significant. The stress softening effect is visible and prominent beyond approximately 0.3% and appears in the other fatigue and creep-fatigue tests. The initial tensile loading part of the stress-strain curves in all experiments is also marked by the presence of serrations induced by the Portevin-Le Chatelier effect [164]. The present approach does not account for this effect and the tensile loading part of the simulations exhibit a smooth loading path.

In view of the above-mentioned points, the simulated overall stress-strain hysteresis curves are in very good agreement with the experiments. In particular, the stress relaxations caused by solute-drag creep are accurately captured as a function of various hold times and strain ranges. Particularly, Fig. 7.16 reveals slight discrepancies in the experimentally observed and simulated compressive flow stresses for creep fatigue tests E-6 and E-10, where the simulations overestimate the flow stress especially during the transient relaxation part. Nevertheless, comparing to the remainder of the creep-fatigue experiments, the simulation results remain within experimental error range.

The evolution of the hysteresis behavior as a function of load cycles are analyzed in the context of experiment F-5, which is a creep-fatigue experiment with applied total strain range of 1% and hold time of 180 s. Figure 7.17 shows the hysteresis loops of the 1st, 50th and 100th cycles from both the experiments and the simulations. The experimentally observed creep-fatigue life of the specimens is 465 cycles. The deformation therefore remains within the viscoplastic regime, with only a small effect of creep processes within the first 100 cycles. The experiment hysteresis loops demonstrate a slightly larger amount of cyclic softening, compared to the simulations. We note that a small amount of cyclic softening is also observed in simulation results due to the viscoplastic processes

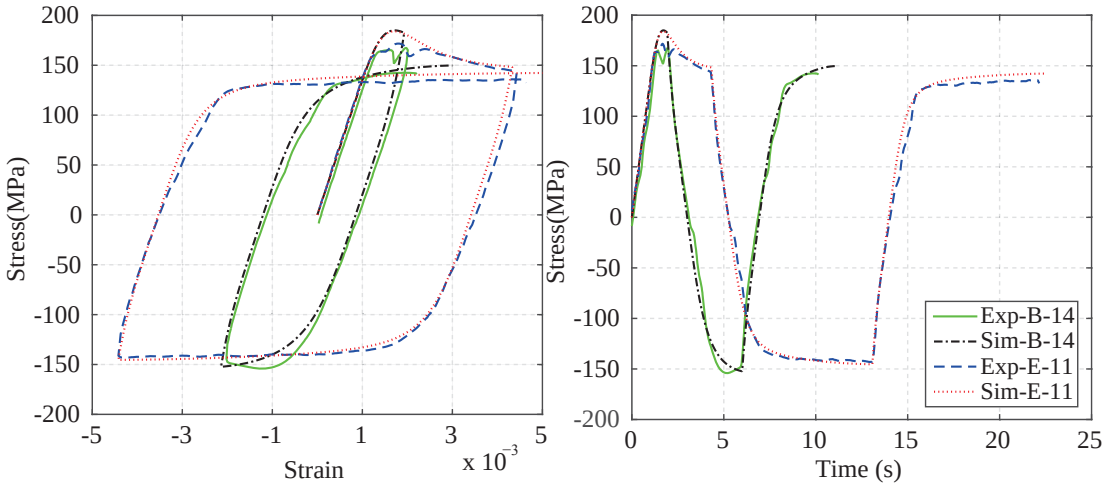

Fig. 7.14: First cycle response of fatigue test B-14 and E-11.

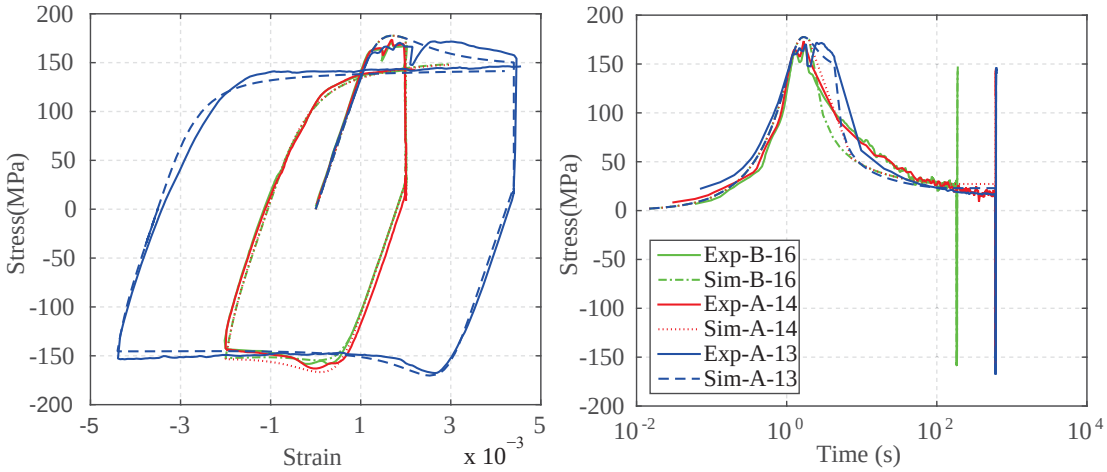

Fig. 7.15: First cycle response of creep-fatigue test B-16, A-14 and A-13.

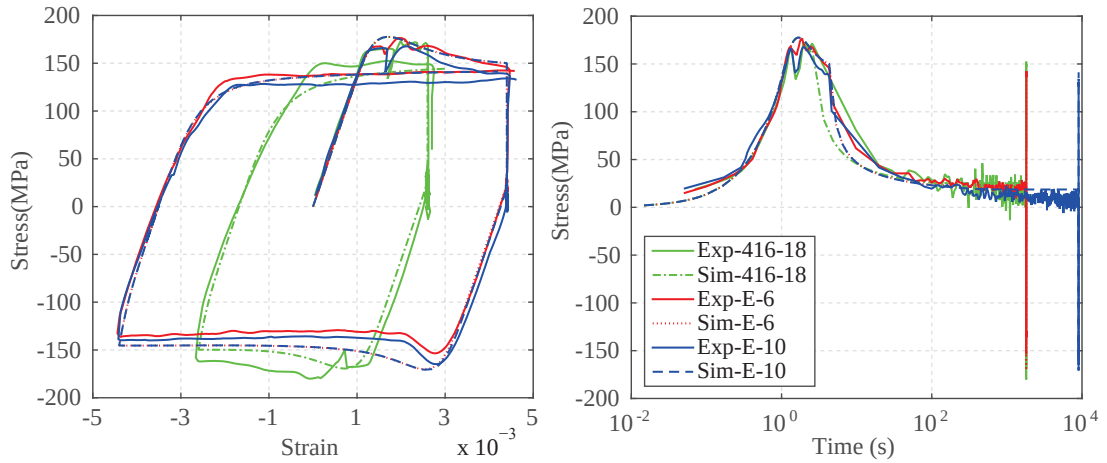

Fig. 7.16: First cycle response of creep-fatigue test 416-18, E-6 and E-10.

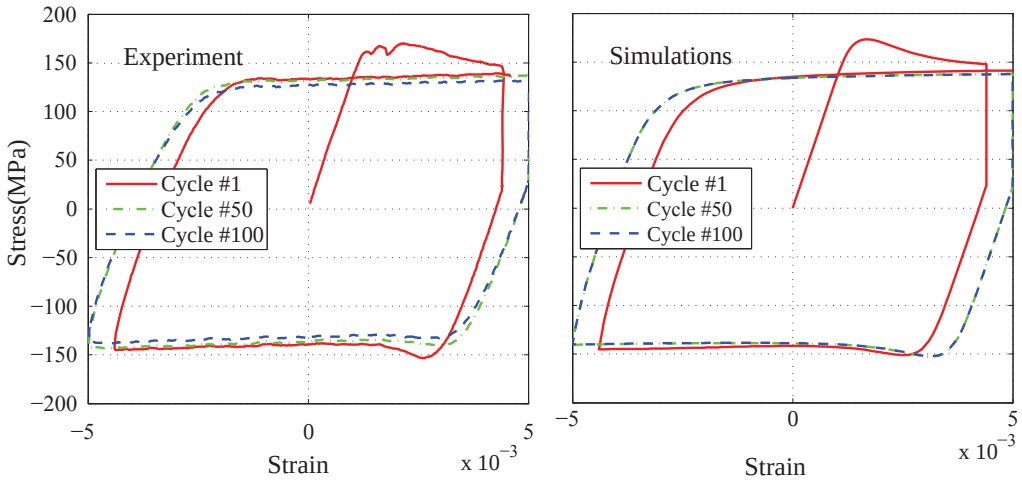

Fig. 7.17: Stress-strain curves of different cycles: (a) experiments; (b) simulations.

modeled in the context of grain deformation. The slight discrepancy between the experimental and simulated cyclic softening is due to the presence of (albeit small) diffusional grain boundary damage (e.g., cavitation) present in the experiments. The current model does not account for creep or fatigue induced damage evolution and these important effects will be investigated in the near future.

7.3.2 Microstructure analysis

The stress distributions within the simulation cell are investigated to gain more understanding of the microstructural aspects of deformation. The analyses are based on the creep-fatigue experiment, F-5. Figure 7.18 shows the stress contour plots over the simulation cell at the beginning, middle and end of hold of the first loading cycle. A complex stress distribution over the microstructure domain is observed with significant stress variations within and between grains, due to differences in grain orientations within the microstructure [84]. Stress concentrations around grain boundaries are also observed, with a naturally higher tendency of stress concentrations with higher misorientation angles. The locations of high stress concentrations (von-Mises stress higher than a threshold magnitude of 280 MPa) are highlighted in Fig. 7.19. It is observed that all of these locations are at the grain boundaries, and the orientations and misorientations around the locations of high stress are shown in Table 7.4. The misorientation angles are computed using the following equation [106, 84]:

$$\theta = \min\left|\cos^{-1}\left\{\frac{tr(\mathbf{g}_B\mathbf{g}_A^{-1}\mathbf{O})-1}{2}\right\}\right| \tag{31}$$

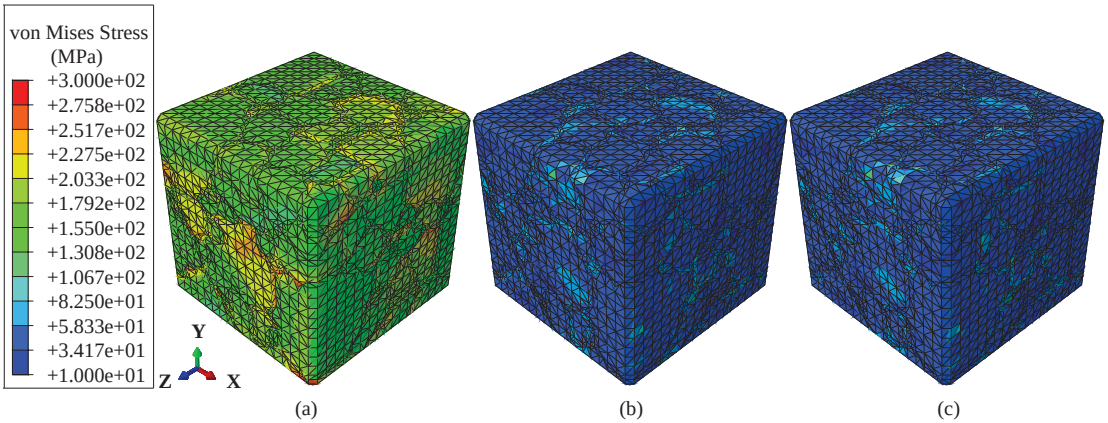

Fig. 7.18: Stress contour of the RVE of the first cycle: (a) beginning of hold; (b) middle of hold; (c) end of hold.

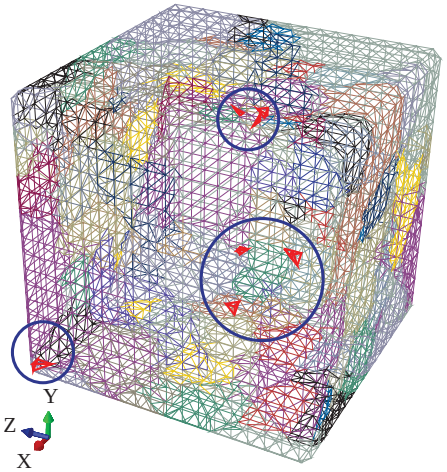

Fig. 7.19: Locations with von-Mises Stress higher than 280 MPa at the beginning of hold.

where, $\mathbf{g}_A$ and $\mathbf{g}_B$ are the orientation matrices of adjacent grains A and B, respectively, tr is the trace operator, and $\mathbf{O}$ is the crystal symmetry operator for FCC crystals.

The stress contours also indicate only a small amount stress redistribution occurs at the latter half of the hold (compare Figs. 7.18(b) and (c)) since the stress relaxation process has largely been completed within the first half of the strain hold. The significant stress relaxation observed during the first part of the hold is also associated with a stress redistribution. The effect of stress redistribution is further demonstrated using the von-Mises stress histograms as shown in Fig. 7.20 for the first, 50th and 100th cycles. The slight leftward shift of the mean stress at the beginning of strain hold from the first to the 100th cycle indicates the viscoplastic cyclic softening process. The {111} pole figure of the microstructure at different stages of the hold (from the first loading cycle) shown in Fig. 7.21 indicates no obvious texture evolution within the cycle. The subsequent loading

Table 7.4: Orientations (Bunge's convention) and misorientations of adjacent grains at the high stress locations.

Orientations of grain A	Orientations of Grain B	Misorientation
(148.51, 61.1, 291.5)	(352.38, 144.74, 242.35)	38.24
(279.2, 44.29, 98.96)	(311.07, 97.24, 264.9)	45.85
(250.05, 44.24, 131.00)	(237.19, 115.02, 41.72)	51.61
(237.19 , 115.02, 41.72)	(67.62, 65.15, 257.39)	34.79
(32.61, 48.65, 182.49)	(354.55, 84.24, 67.38)	57.48
(149.75, 133.74, 160.51)	(207.01, 153.38, 27.1)	37.54

cycles also did not indicate significant texture evolution.

To further investigate the distribution of stresses within and across grains, stress is plotted along the center line of the simulation cell along the X-direction as shown in Fig. 7.22. The dashed vertical lines indicate the grain boundaries, while each little cube shows the initial orientation of each grain relative to the sample coordinate system (Fig. 7.22(a)). Depending on the orientation of a grain with respect to the loading axis, those exhibit large plastic deformations are denoted as soft grains, and those have little or no plasticity are denoted as hard grains. Hard and soft grains are clearly recognized by different stress levels (approximately 200 MPa for the hard grain and 125 MPa for soft grains at the beginning of hold). At the end of the tensile loading process and the beginning of the hold, the stresses appear quite uniform within grains with sharp stress jumps occurring at the grain boundaries. The relaxation process significantly alters the stress patterns and stress gradients occur within grains. The interaction between neighboring grains that relax at different rates may contribute to the complex stress distributions observed during the creep fatigue relaxation process. Within a given cycle, a more uniform stress distribution is observed between hard and soft grains at the end of strain hold compared to the beginning of hold. This is because stresses throughout the microstructure asympotically reduce, due to the viscoplastic relaxation process under constant macroscopic strain. The simulations do not show a noticeably more uniform stress distribution as a function of cycles (i.e., from cycle 1 to 50 to 100). Furthermore, subgrain formation experimentally observed in creep-fatigue behavior of alloy 617 (see e.g., [80]) may be linked to the formation of persistent intragranular stress jumps and gradients.

7.4 Conclusions

We presented the formulation, implementation and calibration of a CPFE model for nickel-based alloy IN 617 at high temperature. Model formulation, implementation and model parameters calibration are discussed in detail, and verification against a series of fatigue and creep-fatigue tests with different strain ranges and hold times are conducted. The proposed evolution equation for the

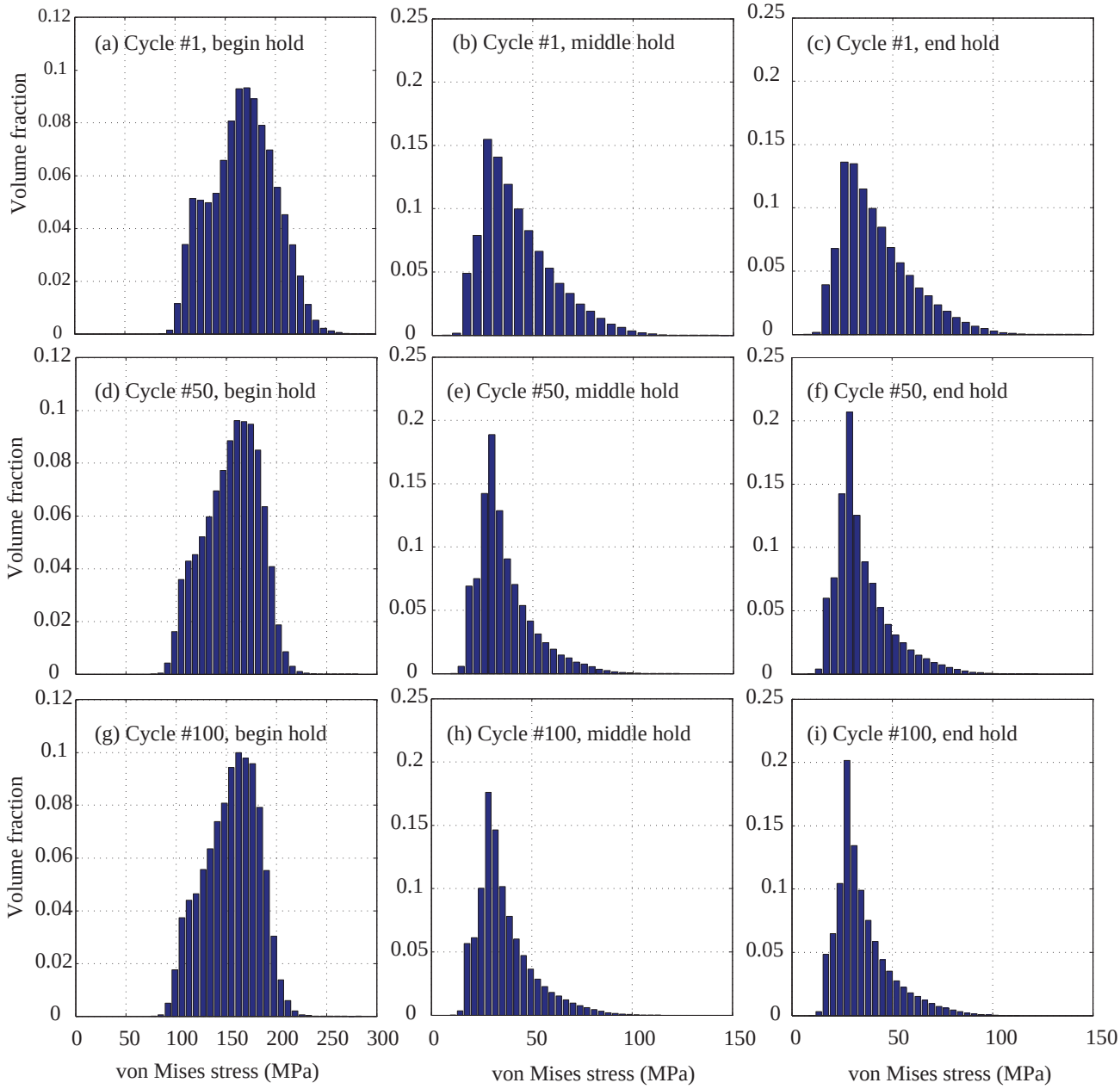

Fig. 7.20: Von Mises stress histograms at different stages within the first (a)-(c), 50th (d)-(e) and 100th (g)-(i) cycle.

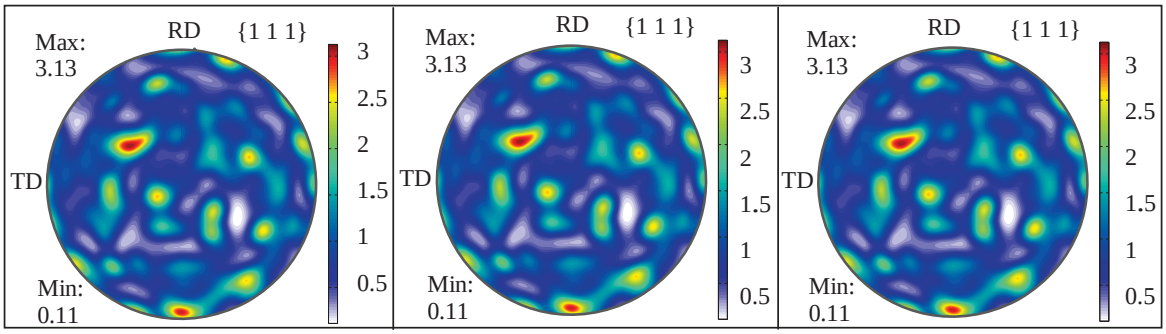

Fig. 7.21: {1 1 1} pole figures of the first cycle: (a) beginning of hold; (b) middle of hold; (c) end of hold.

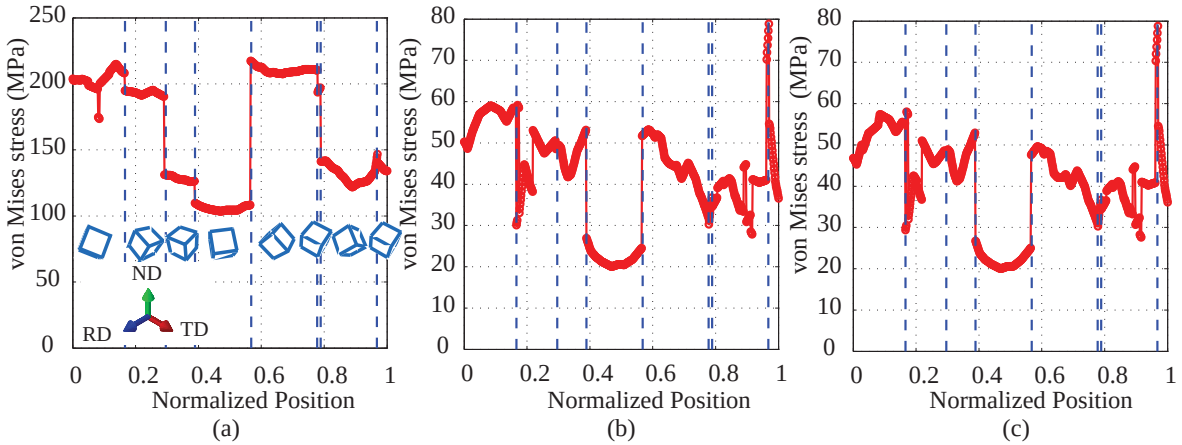

Fig. 7.22: Von Mises stress along a line passing the center of the RVE along X direction of the first cycle: (a) beginning of hold; (b) middle of hold; (c) end of hold.

slip resistance can well capture the stress drop in the first cycle of both fatigue and creep-fatigue tests, as well as the softening reemerging at every cycle after strain hold in the creep-fatigue tests. The current model assumes full traction continuity along grain boundaries while future work will involve cohesive zone modeling of the grain boundaries, which will allow the crack initialization prediction at grain boundaries, and ultimately life prediction. Furthermore, the proposed model will be coupled to structural scale simulations using concurrent-hierarchical multiscale modeling (e.g., [131, 175, 172, 173]), and through sequential multiscale modeling to calibrate model parameters of phenomenological models (e.g., [132, 31]).

8 Microscale Modeling of Creep Deformation and Rupture in IN 617 at High Temperature

In this chapter, a computational microstructure model is developed to capture creep deformation and failure behavior in IN 617 operating at high temperature. In particular, the proposed work is built on the previous glide-based CPFE framework (see also [174]) and incorporates a dislocation climb model originally proposed by Lebensohn and coworkers [110, 111] for capturing the viscoplastic deformation within the grains while grain boundary damage is modeled by CZM. The CPFE and the CZ models work in tandem to compute the viscoplastic deformation as well as progressive failure in the material microstructure. Model parameters are calibrated and validated using experimental creep tests at different hold stress amplitudes. Microscale stress and damage distribution as well as their evolution during the creep process are analyzed to gain further understanding of the underlying deformation mechanisms.

8.0.1 Constitutive Models

Using the virtual work principle, the sum of the strain energy in the domain and the cohesive fracture energy on the intergranular fracture surfaces are equal to the virtual work done by external traction along the boundary (ignoring body forces). The weak form of governing equilibrium equation is expressed as:

$$\int_{\Omega} \mathbf{S} : \delta\mathbf{E} d\Omega + \int_{\Gamma_{\mathrm{GB}}} \mathbf{T} : \delta[\![\mathbf{u}]\!] d\Gamma = \int_{\Gamma_{\mathrm{t}}} \hat{\mathbf{T}} \cdot \delta\mathbf{u} d\Gamma \tag{32}$$

in which, $\mathbf{S}$ is the second Piola Kirchhoff stress, $\mathbf{T}$ the tractions along the grain boundaries idealized as sharp interfaces and denoted as Γ_{GB}, and $\hat{\mathbf{T}}$ the prescribed tractions along the Neumann boundaries of the representative volume domain. $\delta\mathbf{u}$, $\delta\mathbf{E}$ and $\delta[\![\mathbf{u}]\!]$ denote the variations of the displacement, Green-Lagrange strain, and grain boundary displacement jump fields, respectively. In the present formulation, the weak form is closed by the stress-strain relationship within the grains and the traction-displacement jump relationship (i.e., cohesive law) across the grain boundaries.

8.0.2 Crystal plasticity model with dislocation glide and climb

To incorporate the dislocation climb mechanism, the same multiplicative decomposition of deformation gradient as in Eq. (5) and symmetric/skew decomposition of the velocity gradient as in Eq. (11) are used, while the velocity gradient have contributions from dislocation glide (indicated

by subscript g) and climb (indicated by subscript c):

$$\begin{aligned}\widetilde{\mathbf{D}}^{\mathrm{p}} &= \widetilde{\mathbf{D}}^{\mathrm{p}}_{\mathrm{g}} + \widetilde{\mathbf{D}}^{\mathrm{p}}_{\mathrm{c}} \\ \widetilde{\mathbf{W}}^{\mathrm{p}} &= \widetilde{\mathbf{W}}^{\mathrm{p}}_{\mathrm{g}} + \widetilde{\mathbf{W}}^{\mathrm{p}}_{\mathrm{c}}\end{aligned} \tag{33}$$

A dislocation glide based model for IN 617 at high temperature has been previously developed, calibrated and verified in previous chapter (see also Ref. [174]). The dislocation model as well as the calibrated parameters are kept the same as in previous chapter and skipped for brevity. While the dislocation-glide-based model can accurately capture the response of the polycrystal subjected to a fatigue or a creep-fatigue cycle, the ability to capture the long-term creep deformation, particularly at stress levels much lower than the yield stress, requires the inclusion of the dislocation climb mechanism. The rate of deformation and spin contributions of dislocation climb are expressed as [110]:

$$\begin{aligned}\widetilde{\mathbf{D}}^{\mathrm{p}}_{\mathrm{c}} &= \mathbf{R}^{\mathrm{e}} \cdot \sum_{\alpha=1}^{N} \dot{\gamma}^{\alpha}_{\mathrm{c}} \big(\mathbf{m}^{\alpha}_{0} \otimes \boldsymbol{\chi}^{\alpha}_{0}\big)_{\mathrm{S}} \cdot \mathbf{R}^{\mathrm{e}T} = \sum_{\alpha=1}^{N} \dot{\gamma}^{\alpha}_{\mathrm{c}} (\widetilde{\mathbf{K}}^{\alpha})_{\mathrm{S}} \\ \widetilde{\mathbf{W}}^{\mathrm{p}}_{\mathrm{c}} &= \mathbf{R}^{\mathrm{e}} \cdot \sum_{\alpha=1}^{N} \dot{\gamma}^{\alpha}_{\mathrm{c}} \big(\mathbf{m}^{\alpha}_{0} \otimes \boldsymbol{\chi}^{\alpha}_{0}\big)_{\mathrm{A}} \cdot \mathbf{R}^{\mathrm{e}T} = \sum_{\alpha=1}^{N} \dot{\gamma}^{\alpha}_{\mathrm{c}} (\widetilde{\mathbf{K}}^{\alpha})_{\mathrm{A}}\end{aligned} \tag{34}$$

in which, $\dot{\gamma}^{\alpha}_{\mathrm{c}}$ is the shear strain rate as a result of dislocation climb. $\widetilde{\mathbf{K}}^{\alpha} = \widetilde{\mathbf{m}}^{\alpha} \otimes \widetilde{\boldsymbol{\chi}}^{\alpha}$ is the climb tensor associated with the slip system α in the crystal coordinate system [92, 110] (see Fig. 8.1), and $\widetilde{\boldsymbol{\chi}}^{\alpha}$ the unit vector parallel to the product of normal to the glide plane ($\tilde{\mathbf{n}}^{\alpha}$) and the tangent to the dislocation line ($\tilde{\mathbf{t}}^{\alpha}$) defined as:

$$\widetilde{\boldsymbol{\chi}}^{\alpha} = \tilde{\mathbf{n}}^{\alpha} \times \tilde{\mathbf{t}}^{\alpha} \tag{35}$$

It is straightforward to see that the climb tensor depends on the dislocation orientation with respect to the glide coordinate system, and this dependence is expressed in terms of a single parameter ψ (i.e., the angle between $\tilde{\mathbf{t}}^{\alpha}$ and $\tilde{\mathbf{m}}^{\alpha}$) as shown in Fig. 8.1. The climb tensor is then expressed as:

$$\widetilde{\mathbf{K}}^{\alpha} = [\widetilde{\mathbf{m}}^{\alpha} \otimes (\widetilde{\mathbf{m}}^{\alpha} \times \widetilde{\mathbf{n}}^{\alpha})]\mathrm{cos}\psi + (\widetilde{\mathbf{m}}^{\alpha} \otimes \widetilde{\mathbf{m}}^{\alpha})\mathrm{sin}\psi \tag{36}$$

which resolves the applied shear stress into an individual climb system as $\tau^{\alpha}_{\mathrm{c}} = \boldsymbol{\tau} : (\widetilde{\mathbf{K}}^{\alpha})_{\mathrm{dev}}$ and accumulates the climb strain based on a climb flow rule given by:

$$\dot{\gamma}^{\alpha}_{\mathrm{c}} = \dot{\gamma}_{0} \mathrm{exp}\left(-\frac{F_0}{\kappa\theta}\right)\left(\frac{|\tau^{\alpha}_{\mathrm{c}} - B^{\alpha}_{\mathrm{c}}|}{\hat{\tau}_{0\mathrm{c}}}\right)^{p_{\mathrm{c}}} \mathrm{sgn}(\tau^{\alpha}_{\mathrm{c}} - B^{\alpha}_{\mathrm{c}}) \tag{37}$$

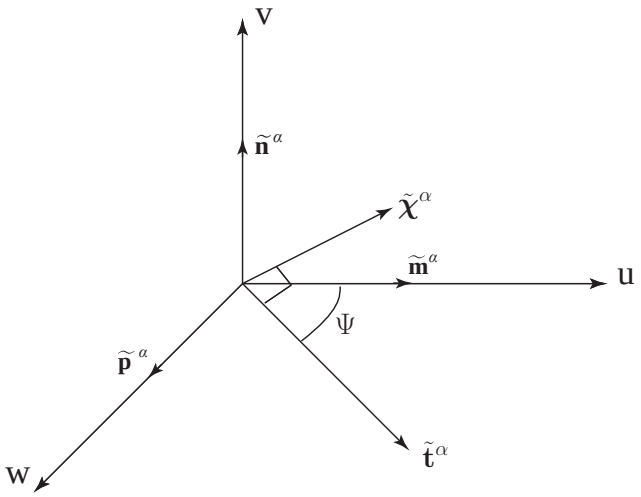

Fig. 8.1: Illustration of dislocation orientation: coordinate system $u - v - w$ is aligned with dislocation glide system α ($\tilde{\mathbf{p}}^{\alpha}$ is the unit vector to complete a right-hand orthogonal coordinate system defined by $\tilde{\mathbf{n}}^{\alpha}$ and $\tilde{\mathbf{m}}^{\alpha}$) and dislocation climb orientation depends the angle ψ formed by the dislocation line $\tilde{\mathbf{t}}^{\alpha}$ and the slip direction $\tilde{\mathbf{m}}^{\alpha}$.

where $\dot{\gamma}_0$ denotes the reference shear strain rate, F_0 the activation energy, κ the Boltzmann constant and θ the temperature in Kelvin. $\hat{\tau}_{0\mathrm{c}}$ and p_{c} are the scalar threshold creep stress and the creep exponent, respectively. The evolution of backstress B_{c}^{α} is formulated through a saturation value, B_{∞}, related to the end of the primary creep stage as follows [152]:

$$\dot{B}_{\mathrm{c}}^{\alpha} = C_1 \dot{\gamma}_{\mathrm{c}}^{\alpha} - C_2 |\dot{\gamma}_{\mathrm{c}}^{\alpha}| B_{\mathrm{c}}^{\alpha} = h_{\mathrm{c}} (\dot{\gamma}_{\mathrm{c}}^{\alpha} B_{\infty} - |\dot{\gamma}_{\mathrm{c}}^{\alpha}| B_{\mathrm{c}}^{\alpha}) \tag{38}$$

where, h_{c} is a material parameter.

Equations (5)-(11) and (33)-(38) together with the flow rule and the hardening rule associated with dislocation glide lead to a coupled nonlinear equation system, with $\boldsymbol{\tau}$, $\mathbf{R}^e$, glide resistance S^{α}, glide backstress B^{α} and climb backstress B_c^{α} as unknowns. To facilitate the solution process, an operator split method with a two-level staggering scheme is adopted to solve the nonlinear system. The numerical implementation of the glide and climb based constitutive model is a straightforward generalization of the glide-only model (see [174] for more details).

The incorporation of dislocation climb mechanism in Eqs. (33)-(38) allows the prediction of primary creep deformations. As observed in experimental creep curves of [101, 162], IN 617 does not exhibit a clear secondary creep stage. The extension of the present glide-climb model to capture secondary creep is possible and straightforward for evaluation of the creep response of other alloys that exhibit clear secondary creep.

8.0.3 Cohesive zone modeling (CZM) for creep damage

CZM is a computational approach to track propagation of distinct cracks, where fracture is considered as a gradual process of surface separation that takes place along an extended crack tip (or cohesive zone) resisted by cohesive tractions. Cohesive zone model is advantageous over other fracture mechanics based models, since it does not require the presence of pre-cracks. It can predict the behavior starting from an uncracked configuration, and performs well in the context of nonlinear material behavior. One significant caveat is that, unless coupled with adaptive meshing techniques, the direction of crack propagation is prescribed by the underlying finite element discretization. The CZM approach is therefore particularly powerful in cases, where the path of crack propagation is known a-priori (e.g., cracking along grain boundaries).

The cohesive law is derived from a damage-based cohesive grain boundary potential defined by:

$$\phi = \frac{1}{2\delta_{\mathrm{c}}}\left(1-\omega_{\mathrm{n}}\right)k_{\mathrm{n}}[\![u_{\mathrm{n}}]\!]^2 + \frac{1}{2\delta_{\mathrm{s}}}\left(1-\omega_{\mathrm{s}}\right)k_{\mathrm{t}}\|[\![\mathbf{u}_{\mathrm{t}}]\!]\|^2 \tag{39}$$

where, $[\![u_{\mathrm{n}}]\!]$ and $[\![\mathbf{u}_{\mathrm{t}}]\!]$ denote the normal and tangential separation vectors, respectively, ω_{n} the interface damage induced by creep cavitation, ω_{s} the damage induced by grain boundary sliding, k_{n} and k_{t} are the initial stiffness along the normal and tangential directions, respectively, δ_{c} and δ_{s} are respectively the critical displacement jump in the normal and tangential directions at the point of complete separation when loaded monotonically:

$$\omega_{\mathrm{n}} = 1 \rightarrow [\![u_{\mathrm{n}}]\!] = \delta_{\mathrm{c}}; \quad \omega_{\mathrm{s}} = 1 \rightarrow \|[\![\mathbf{u}_{\mathrm{t}}]\!]\| = \delta_{\mathrm{s}}. \tag{40}$$

In order to idealize progressive creep failure, the cohesive law proposed by Bouvard et al. [75] is employed. The cohesive law is built by considering $\delta_{\mathrm{s}} = \delta_{\mathrm{c}}$, $k_{\mathrm{t}} = \alpha k_{\mathrm{n}}$, and:

$$\omega_{\mathrm{c}} := \omega_{\mathrm{n}} = \omega_{\mathrm{s}} \tag{41}$$

in which, ω_{c} denotes the creep damage variable. The potential function in Eq. (39) then becomes:

$$\phi = \frac{1}{2\delta_{\mathrm{c}}}(1-\omega_{\mathrm{c}})k_{\mathrm{n}}\left([\![u_{\mathrm{n}}]\!]^2 + \alpha\|[\![\mathbf{u}_{\mathrm{t}}]\!]\|^2\right). \tag{42}$$

The derivatives of the cohesive potential ϕ with respect to the normal and two tangential separations lead to the normal and shear tractions:

$$T_{\mathrm{n}} = \frac{\partial\phi}{\partial[\![u_{\mathrm{n}}]\!]} = k_{\mathrm{n}}(1-\omega_{\mathrm{c}})\frac{[\![u_{\mathrm{n}}]\!]}{\delta_{\mathrm{c}}} \tag{43}$$

$$\mathbf{T}_{\mathrm{t}} = \frac{\partial \phi}{\partial [\![\mathbf{u}_{\mathrm{t}}]\!]} = \alpha k_{\mathrm{n}} (1 - \omega_{\mathrm{c}}) \frac{[\![\mathbf{u}_{\mathrm{t}}]\!]}{\delta_{\mathrm{c}}}. \tag{44}$$

When subjected to compression, the normal traction is described as:

$$T_{\mathrm{n}} = k_{\mathrm{c}} \frac{[\![u_{\mathrm{n}}]\!]}{\delta_{\mathrm{c}}} \tag{45}$$

where, k_{c} is the penalty parameter. Equation (45) ensures that the impenetrability across the cohesive interface is satisfied under compressive loading condition through the penalty method. The magnitude of the penalty parameter is chosen as large as possible to limit interpenetration. Setting this parameter to extremely large values is known to result in numerical convergence difficulties.

Creep damage evolution is idealized using a power law in the following form [75]:

$$\dot{\omega}_{\mathrm{c}} = \frac{1}{(1 - \omega_{\mathrm{c}})^{p}} \left\langle \frac{||\mathbf{T}|| - T_{\mathrm{c}}}{C} \right\rangle^{r} \tag{46}$$

where T_{c}, C, p and r are model parameters defining the evolution of the creep damage. T_{c} denotes a threshold traction, above which creep damage accumulates. The norm of traction vector is defined by:

$$||\mathbf{T}|| := \sqrt{\langle T_{\mathrm{n}} \rangle^{2} + \frac{1}{\alpha} \|\mathbf{T}_{\mathrm{t}}\|^{2}} \tag{47}$$

where $\langle \cdot \rangle = (|\cdot| + (\cdot))/2)$ denotes the Macaulay brackets, which eliminates the compressive grain boundary tractions from contributing to creep damage evolution.

The CZM model has been numerically implemented via a user defined element (UEL) subroutine in the commercial software Abaqus. At each increment of the nonlinear finite element analysis, the UEL is called at each cohesive zone element to solve the separation-traction equation, perform interface element level integration, and update the incremental local force vector and stiffness matrix. In order to evaluate the cohesive law and determine the creep damage state within the cohesive element, the creep damage variable ω_{c} of all Gauss points belonging to each cohesive zone element is solved at each time increment through a Newton-Raphson method using a creep damage residual function obtained from the creep damage evolution in Eq. (46). At each time increment, the nodal displacement fields in the global coordinate system and the cohesive zone model parameters (k_n, α, T_c, δ_c, C, p and r) are considered as inputs while the local force vector and the stiffness matrix of each cohesive element are computed and passed back for the finite element assembly and solver operations. The detailed implementation of CZ elements are provided in Ref. [151].

8.1 Model Preparation

IN 617 is a solid solution strengthened alloy with face center cubic (FCC) lattice structure. While γ' precipitates exist at lower temperature, IN 617 is largely free of γ' phase at temperature above 750°C [72] and 12 $\{100\}\langle 110\rangle$ slip systems remain active. The microstructure exhibits distinguishable coarse and fine grains and random initial orientation [123] and a bimodal grain size distribution. This section briefly reviews the microstructure generation and meshing process, based on which, the insertion of cohesive zone elements along the grain boundaries is described.

8.1.1 Microstructure generation

A microstructure reconstruction and meshing work flow has been developed to obtain representative volume discretization for microstructure analysis. The work flow consists of (1) Generation of the microstructure morphology based on experimental data; (2) Volume meshing; and (3) Insertion of cohesive elements between grain pairs.

Microstructure generation is performed using the software DREAM.3D [90] as detailed in the previous chapter. The microstructure generation and meshing procedure is briefly summarized here to facilitate the demonstration of the seamless incorporation of the CZ elements insertion procedure. Experimental EBSD measurements (Fig. 8.2(a)) are used to extract the microstructure statistical and morphological information (e.g., grain size distributions in Fig. 8.2(b) and (c)) and construct statistically equivalent microstructures (Fig. 8.2(d)), based on which surface mesh of individual grains are obtained. The surface mesh of each grain is essentially a collection of triangular facets that enclose the domain of that grain and belongs to either an external boundary of the microstructure, or to the internal grain boundaries. The parallel polycrystal mesher (PPM) software [81] is used to generate the volume mesh of each individual grain using the surface mesh, which is then stitched together to form the volume mesh of the whole microstructure (Fig. 8.2(e)). Zero-thickness cohesive zone elements are inserted along the grain boundaries (Fig. 8.2(f)) using the surface mesh information of each grain following a consistent and automated procedure described below.

In general, a microstructure volume must be chosen large enough to be statistically representative. In contrast, the high computational cost of combined CPFE-CZM simulations necessitates the use of the smallest possible microstructure. In order to choose the representative volume element (RVE), a microstructure convergence study was conducted [174] on a series of increasing size microstructures generated using the bimodal grain size distribution (Fig. 8.2(b)-(c)) and random orientation distribution from the EBSD measurements (Fig. 8.2(a)). A 144-grain RVE (Fig. 8.2(e)) is identified to be appropriate for the current study and shows convergence in terms of both overall

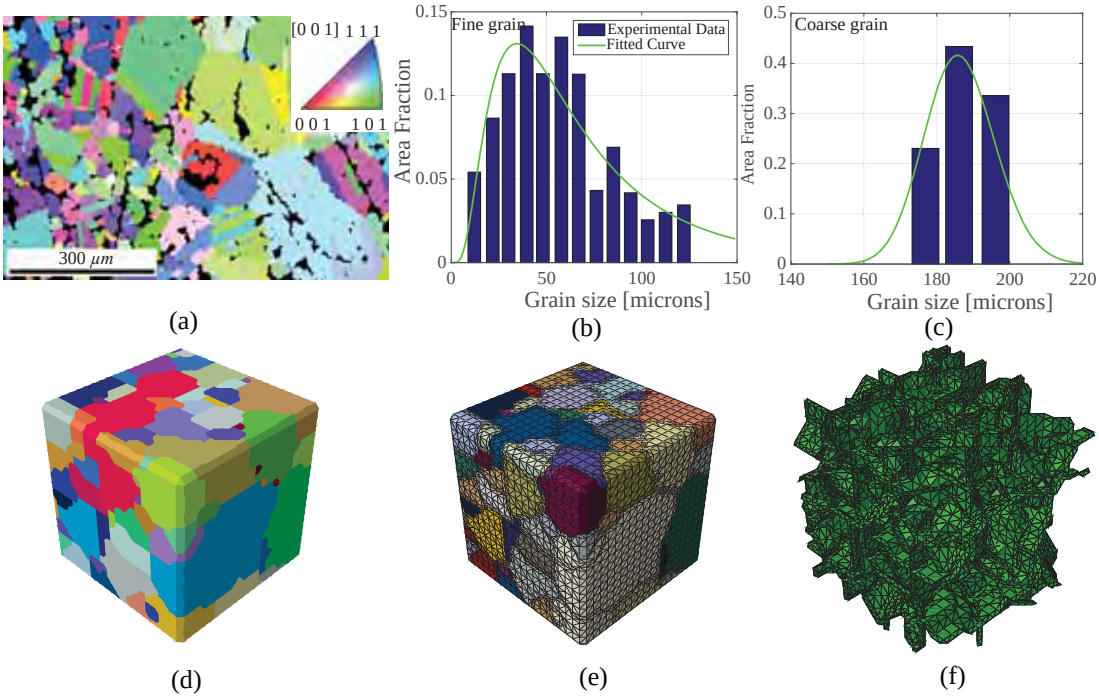

Fig. 8.2: Microstructure reconstruction and meshing: (a) EBSD data; (b)-(c) bimodal grain size distribution; (d) synthetic microstructure reconstruction; (e) volume mesh of the microstructure; (f) zero-thickess cohesive zone elements for grain boundaries.

stress-strain response as well as the local stress distributions. This 144-grain RVE microstructure with edge length of $320\mu m$ discretized by 133,372 linear four-node tetrahedral (C3D4) elements (Fig. 8.2(e)) is used in all numerical simulations performed in this study.

8.1.2 Incorporation of cohesive elements

The cohesive elements are embedded into the microstructure mesh using an automated element insertion methodology that defines the element connectivities for arbitrary 3-D microstructures.

The cohesive element incorporation procedure is implemented consistent with the microstructure morphology and surface mesh generation in DREAM.3D and the insertion process only adds cohesive zone element connectivity using grain boundary nodes, leaving the tetrahedral volume mesh of the grains intact. The surface mesh (triangular facets) of each grain either belongs to an external boundary of the representative volume or to the grain boundaries. Nodes on the surface mesh of each grain are assigned a unique node ID. A k-d tree based search process is then conducted to identify the cohesive node pairs (i.e., nodes sharing the same coordinates but belong to two different grains) and subsequently the cohesive face pairs (i.e., two triangle facets formed by three pairs of cohesive node pairs belonging to two different grains) of each grain boundary facet. Each cohesive

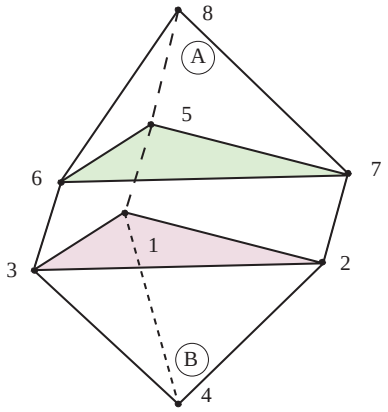

Fig. 8.3: Configuration of the cohesive zone element. Thickness is exaggerated to be nonzero for illustration purpose.

face pair is used to define a zero-thickness cohesive zone element.

To guarantee the correct calculation of separation and traction, and a positive element Jacobian within the cohesive element, a set of consistent cohesive zone element connectivity construction rules as illustrated in Fig. 8.3 is defined as follows:

1. One cohesive zone element is inserted between two adjacent bulk elements that belong to two different adjacent grains. As illustrated in Fig. 8.3, element A and B belong to two different grains with node pairs 6-3, 5-1 and 7-2 being three cohesive node pairs and the blue and green faces being a cohesive face pair. A cohesive zone element is inserted between element A and B using nodes 5, 6, 7, 1, 2 and 3.

2. Element connectivity starts from any node that belongs to one of the two cohesive face pairs, loops over all nodes belongs to that face and then nodes on the other face. We ensure that the ordering of nodes of the face of the first grain (starting from the chosen node), and the opposing face are identical. For instance, starting from node 1 of grain B, either 1-2-3-5-7-6 or 1-3-2-5-6-7 are the two possible connectivities.

3. The normal direction for the starting grain face using the right-hand rule is taken to point to the opposing grain. For instance, the first element connectivity 1-2-3-5-7-6 yields the normal direction of face 1-2-3 pointing away from the second grain while the second element connectivity 1-3-2-5-6-7 has the normal direction of face 1-3-2 pointing to the second grain. The latter is therefore the valid cohesive element connectivity.

The three rules mentioned above provide a consistent cohesive element connectivity definition methodology. Using this procedure, 22,430 cohesive elements are inserted into the above 144-grain

RVE to discretize the grain boundaries (Fig. 8.2(f)), which together with the 133,372 tetrahedral elements form the full discretization of the microstructure.

8.2 Model Calibration

The parameters of the model associated with the intragranular deformation mechanisms, as well as the intergranular creep damage are calibrated based on experimental data. Model parameters related to the dislocation glide in IN 617 at 950°C have been previously calibrated [174] and employed as is in this study. Table 1 includes the calibrated parameters that control the dislocation glide. In what follows, the calibration of model parameters related to the dislocation climb and the cohesive grain boundary behavior is discussed. In order to facilitate the calibration process, we first isolate the effects of the dislocation climb parameters by focusing on creep deformation prior to the onset of significant grain boundary damage. The cohesive zone parameters are subsequently calibrated by focusing on creep deformation after grain boundary damage initiation until rupture. Creep tests on IN 617 specimens conducted at Idaho and Argonne National Labs (INL and ANL) have been used to calibrate these parameters [162]. In particular, creep behavior at two applied stress amplitudes of 28.6 and 24 MPa at 950°C are used for calibration.

It is important to note that the number of parameters that describe dislocation climb as well as intergranular damage is high (i.e., 12 parameters). In contrast, only a small number of detailed experiments are available, primarily at the bulk scale. In view of limited calibration data, we rely on: (1) use of previously published data to establish values for some of the parameters and discard them from the calibration set; (2) perform least squares optimization to identify the parameters by minimizing the discrepancy between the experimental and simulated behavior; and (3) ensure that the values of the parameters are within physically meaningful ranges. The third step is necessary, since multiple local minima may result from the optimization process.

8.2.1 Calibration of dislocation climb parameters

The dislocation climb parameters including the orientation of dislocation climb ψ, the creep exponential parameter p_{c}, the threshold stress $\hat{\tau}_{0\mathrm{c}}$, the saturation stress B_{∞} and the primary creep saturation parameter h_{c} as represented in Eqs. (36), (37) and (38) have been identified. We only focus on the creep-deformation prior to the onset of tertiary creep, where progressive grain boundary damage accumulation using cohesive zone modeling is not included in this calibration step. The calibration process starts with a parametric study to investigate the sensitivity of each parameter in order to identify the ranges for each parameter, where the optimization will be performed. In view of the computational complexity of performing many forward simulations using the CPFE

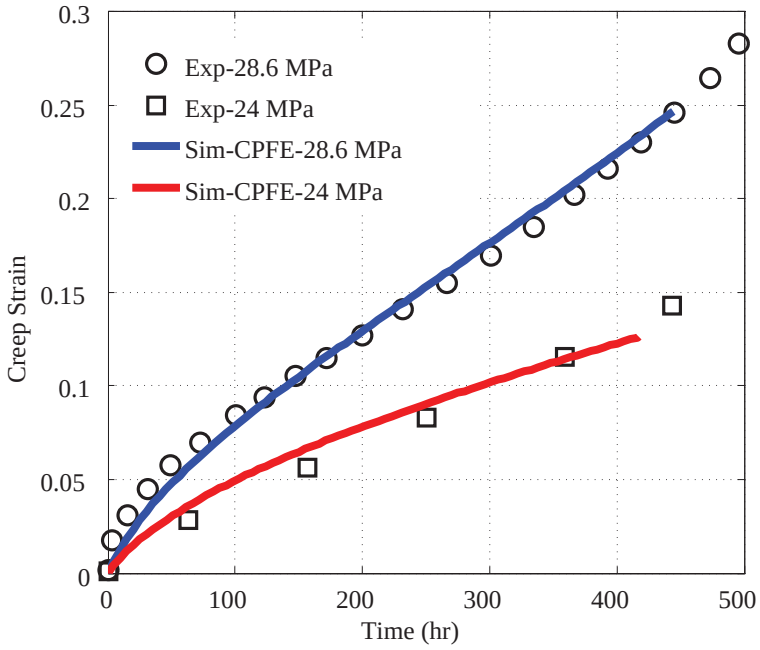

Fig. 8.4: Calibrated results of the creep tests to capture the primary creep at two different stress levels.

model within an optimization framework, we first performed the optimizations based on Taylor's hypothesis [158] to quickly arrive at a set of parameters that provide an acceptable match for the two calibration tests. The identified parameters are further fine-tuned by performing full CPFE simulations. The creep exponent value is set to be $p_c = 3$ according to the creep strains controlled mainly by climb at high temperatures [125]. It is difficult to determine experimentally the angle ψ, i.e., the average edge/screw ratio since it is related to the measurement of dislocation motion in each slip system during creep deformation process. Therefore, the angle is assumed to be $\pi/4$ that corresponds to a length equal of edge and screw dislocation lines in each face-centered cubic slip system [76, 110]. The remaining parameters are calibrated by minimizing the discrepancy between the experimental and simulated creep curves in the primary stage. The set of parameters that results from the above-mentioned calibration process is shown in Table 8.1.

The comparisons between simulated creep curves using the calibrated parameters and experimental creep curves for the two different stress levels are shown in Fig. 8.4. It can be seen that a reasonable match is achieved between the simulated and experimentally observed creep strain evolution as a function of time prior to the onset of grain boundary damage. The yield strength of the material at 950°C is approximately 150 MPa and the applied creep stress amplitudes are substantially lower than yield. We note that in the absence of the climb mechanism, CPFE simulations with only the glide does not show any appreciable creep at stress magnitudes lower than

Table 8.1: Dislocation glide and climb parameters. Glide related parameters are explained in Ref. [174]

C_{11} (GPa)	C_{12} (GPa)	C_{44} (GPa)	$\dot{\gamma_0}$ (s^{-1})	F_0 (J)
170.64	108.39	77.82	1.44×10^{-3}	5.148×10^{-19}
μ_0 (GPa)	μ (GPa)	μ_0'	$\hat{\tau}_0$ (MPa)	f
265.33	77.82	31.13	268.2	0.36
p	q	h_{s} (MPa)	d_{D} (MPa)	S_0^{α} (MPa)
0.181	1.633	397.73	5073.62	143.41
$\bar{S}^{\alpha}$ (MPa)	h_{B} (MPa)	h_2 (MPa)	$\dot{\gamma}_{\mathrm{th}}$ (s^{-1})	
18.03	104.31	0.015	1.0×10^{-6}	
$\psi(^{\circ})$	p_{c}	$\hat{\tau}_{0\mathrm{c}}$(Pa)	h_{c}	B_{∞}(MPa)
$\pi/4$	3	$7,750$	32	4.7

yield. The climb mechanism is therefore primarily responsible for creep strain accumulation at low stress levels. .

8.2.2 Calibration of cohesive zone model parameters

The combined CPFE-CZM is employed to capture the creep damage behavior at grain boundaries in the tertiary stage. Two of the cohesive zone parameters (k_{n} and α) correspond to the elastic behavior of the interface. k_{n} and α are chosen large enough such that no significant separation is observed under normal or shear loading in the absence of damage, while keeping the numerical stability in the simulations. k_{n} ($= 10^5$ GPa) is identified through a parameter sensitivity analysis. A lower amplitude of k_n results in softening in the elastic region of the stress-strain curves. α is chosen as 0.5 consistent with the prior studies on Nickel alloy microstructures (e.g., [155]). The penalty parameter is taken as $k_{\mathrm{c}} = 10k_{\mathrm{n}}$ [75] in the numerical simulations to constrain against granular interpenetration. Friction is not considered along the grain boundaries following decohesion.

Table 8.2: Calibrated parameters of the cohesive zone model.

α	k_{n}(Pa)	$\delta_{\mathrm{c}}(\mu\mathrm{m})$	r	p	C(Pa)	T_{c}(Pa)
0.5	10^{14}	450	2.6	3	4.87×10^5	8.5×10^6

The remainder of the model parameters for the CZM model is calibrated by minimizing the discrepancy between the experimental and simulated creep curves in the tertiary stage. The intrinsic length parameter δ_{c} is identified as 450 μm which lies within the range provided by Bouvard et al. [75] and Sun et al. [155]. The threshold traction T_{c} corresponding to creep strength is assumed to be 8.5 MPa. The exponent p is 3 consistent with that provided in Ref. [155]. The complete set of

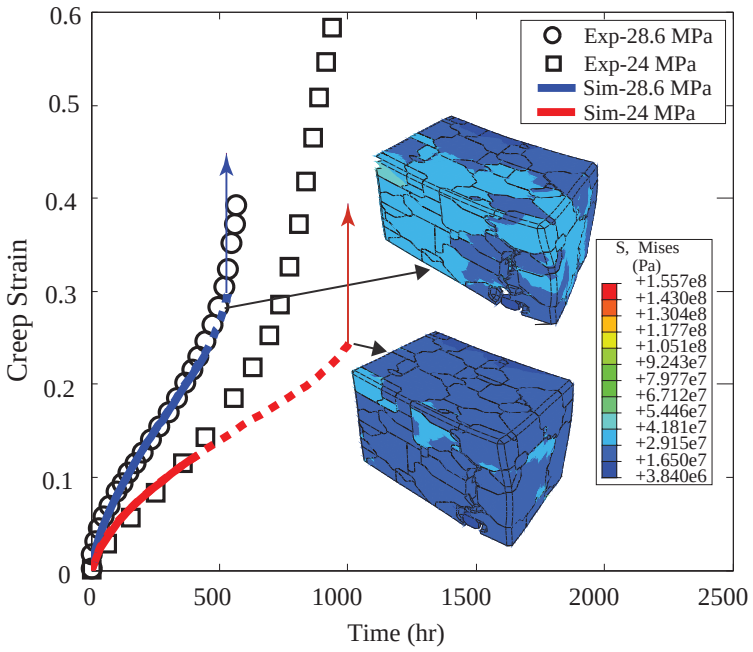

Fig. 8.5: Calibrated results of the creep tests in both primary and tertiary stages for two different stress levels. Dotted lines indicate the presence of GB damage.

calibrated CZM parameters is shown in Table 8.2.

Figure 8.5 shows the comparison between the numerically simulated and experimental creep curves. The match indicates that CPFE-CZM simulation can capture the progressive damage evolution and rupture in the specimens at two stress levels with reasonable accuracy. The experimentally observed rupture times for specimens subjected to 24 MPa and 28.6 MPa are 940 and 566 hours, respectively. The simulated rupture times for the two cases are 1010 and 540 hours, respectively. Rupture is determined when the intergranular separations are fully developed, and when the simulations loose stability under the applied stress amplitude.

The creep damage evolution in the tertiary stage for the specimen subjected to 28.6 MPa has been captured well, whereas the simulated creep strain evolution underpredicts strain rate at the tertiary stage for the 24 MPa case. The simulations also predict a more sudden rupture compared to the experiments.

8.3 Microstructural Analysis and Validation

8.3.1 Microstructural analysis

We investigate the state of stress and damage within the microstructure at various creep strain levels to understand the initiation and evolution of grain boundary damage. Figure 8.6 compares the

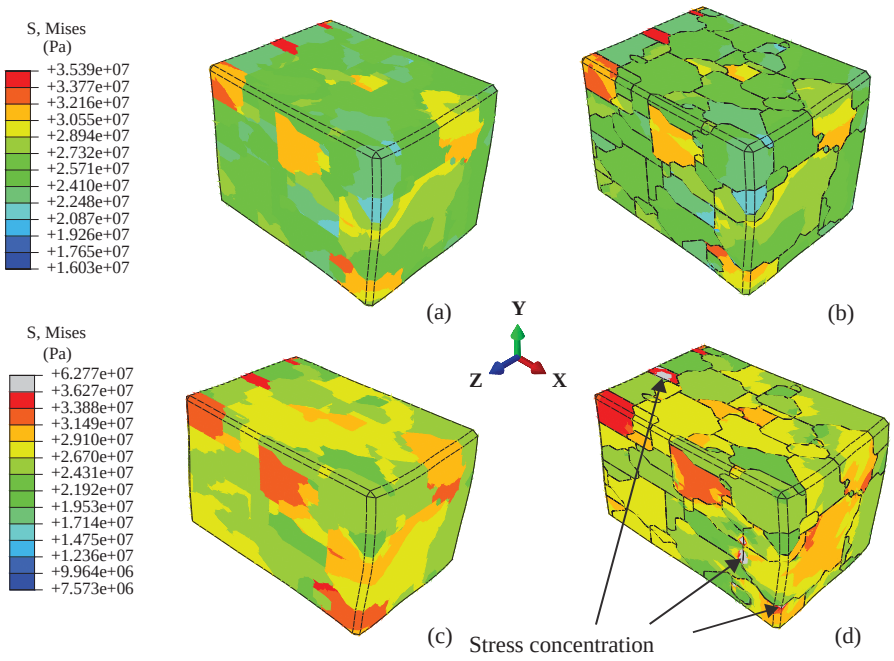

Fig. 8.6: Comparison of stress distribution in the microstructure under 28.6 MPa loading. The CPFE (left) and the CPFE-CZM (right): (a-b) 12% and (c-d) 19% of creep strain at 180 and 347 hours, respectively.

microstructural stress distributions obtained by CPFE-CZM simulation and glide-climb controlled CPFE simulation (without grain boundary damage) at 12% and 19% creep strains under the applied stress of 28.6 MPa. The stress distributions are very similar between the two models at the strain level of 12%, indicating that there is negligible cavitation and/or sliding at the grain boundaries. This observation is consistent with experimental investigations on the microstructures of crept IN 617 specimens, which did not show appreciable grain boundary cavitation prior to approximately 12% strain levels as discussed in Ref. [114]. At 19% creep strain, significant grain boundary damage is observed in the CPFE-CZM simulation that results in the formation of stress concentrations shown in Fig. 8.6(d). The stress concentrations in turn accelerate further damage propagation. This behavior is consistent with the observations in the literature [148, 169] on the nucleation of grain boundary cavities for metals and superalloys. Figure 8.7 displays the further growth of grain boundary damage at 25% and 30% creep strains modeled using the CPFE-CZM simulation. The figure indicates that the separation initiates at the grain boundary and continues to grow until rupture. The extent and magnitude of separation at the strain level of 30% are very significant, which causes an acceleration of the creep strain rate and immediate rupture in the simulation.

Figure 8.8 shows the deformation of the RVE at the time when the cracks shown in Fig. 8.7 initiate. All cracks initiate at triple junctions, where three or more grains adjoin each other.

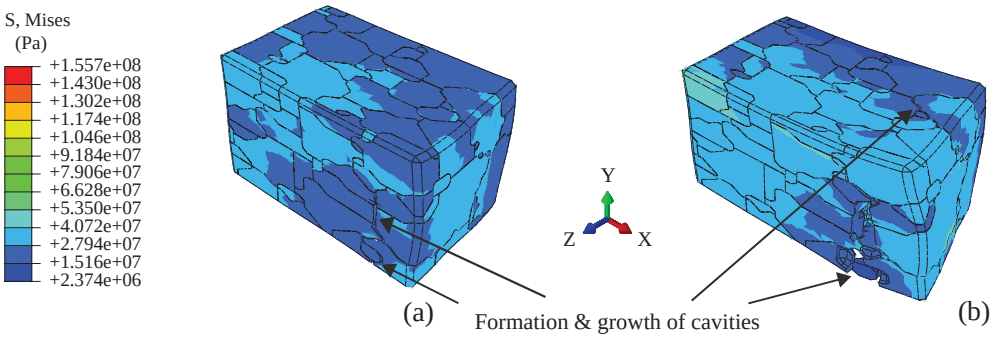

Fig. 8.7: Stress distribution in the microstructure applied by 28.6 MPa loading using the CPFE-CZM: (a) 25% and (b) 30% of creep strain at 472 and 540 hours, respectively.

Table 8.3: Orientations (Bunge's convention) and misorientations of grains along the crack initiation sites.

ID of grain A	ID of grain B	Misorientation
93	98	53.26
105	42	28.78
136	42	36.49
136	95	21.09
43	10	41.83
43	42	45.42
29	26	39.49
80	122	47.37
5	122	60.91

Furthermore, cracks initiate at the grain boundaries perpendicular to the loading direction (e.g., between grains 93 and 98, 105 and 42, 136 and 42, 136 and 95, 43 and 10, 43 and 42, 29 and 26, 80 and 122 and grains 5 and 122) and later propagate to the boundaries nearby (e.g., between grains 105 and 136 and grains 80 and 5). The misorientations of the grain boundary crack initiation sites in Fig. 8.8 are calculated in Table 8.3 using the expression [174]:

$$\theta = \min \left| \cos^{-1} \left\{ \frac{tr(\mathbf{g}_B \mathbf{g}_A^{-1} \mathbf{O}) - 1}{2} \right\} \right| \tag{48}$$

where, $\mathbf{g}_A$ and $\mathbf{g}_B$ are the orientation matrices of adjacent grains A and B, respectively, tr is the trace operator, and $\mathbf{O}$ is the crystal symmetry operator for FCC crystals. The histogram of misorientations of all grain boundaries within the microstructure are shown in Fig. 8.9. The misorientations on the damage initiation sites are relatively large as shown in Table 8.3.

In order to illustrate damage nucleation and evolution, the creep damage variable ω_c is plotted along all grain boundaries as shown in Fig. 8.10 for various states of creep strain. The grain boundary damage initiates at around 12% creep strain state as shown in Fig. 8.10(a). The growth of damage

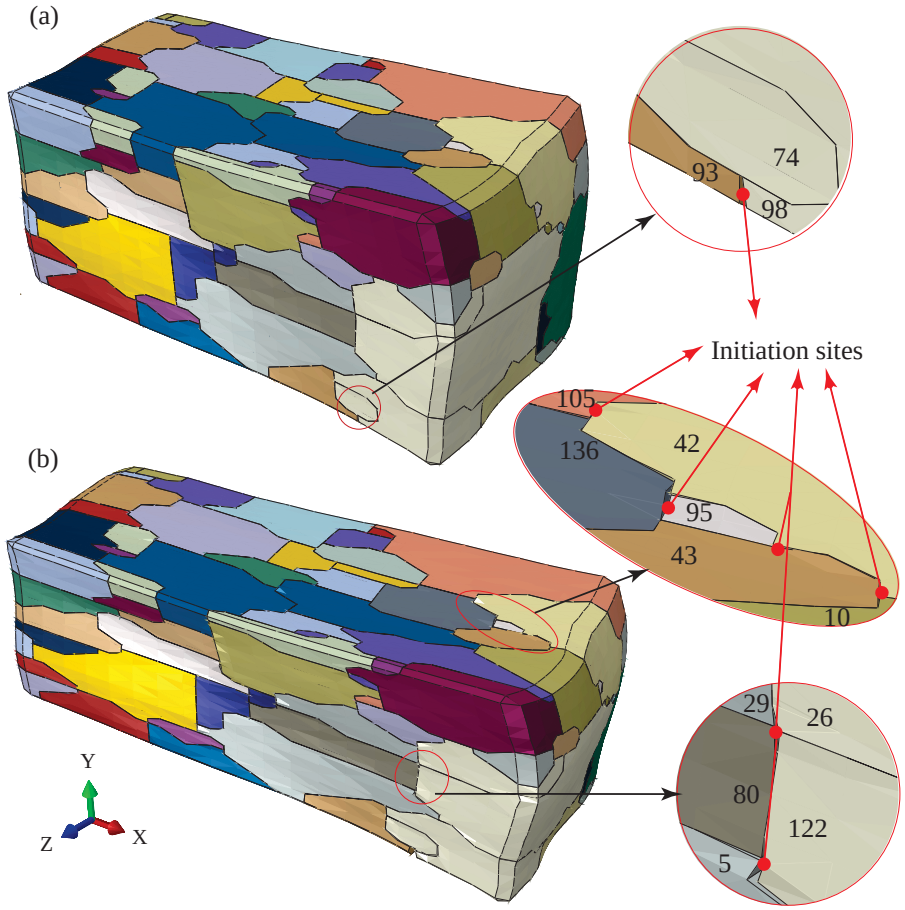

Fig. 8.8: Crack initiation sites at: (a) t=220 h and; (b) 355 h. (Different colors indicate different grains with black lines indicating grain boundaries. Numbers indicate grain IDs. Deformation is exaggerated by a factor of 5.)

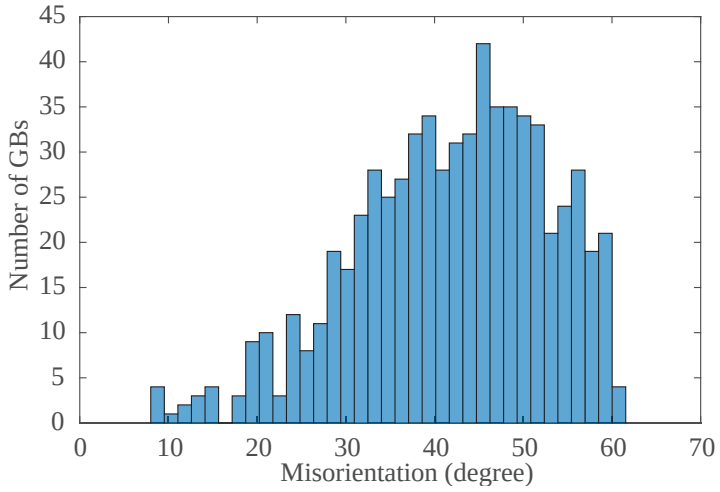

Fig. 8.9: Misorientation of all the grain boundaries in the RVE.

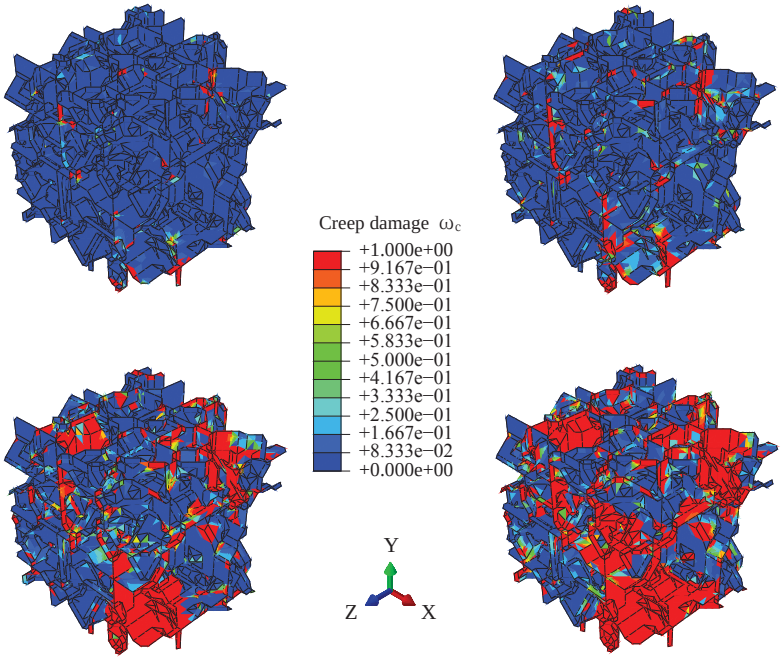

Fig. 8.10: Creep damage evolution represented by cohesive elements in the microstructure under 28.6 MPa loading: (a) 12%, (b) 19%, (c) 25%, and (d) 30% of creep strain at 180, 347, 472 and 540 hours, respectively.

progresses fairly uniformly across the microstructure (Fig. 8.10(b)) until approximately 25% creep strain, after which damage localizes to a grain boundary that is perpendicular to the load direction (lower left corner in Fig. 8.10(c)). Near the point of rupture (Fig. 8.10(d)) the intergranular crack has propagated significantly. Figure 8.11 further demonstrates the state of intergranular damage from different viewpoints near the rupture time.

Previous investigations generally relied on the assumption that damage predominantly resides on the grain boundaries oriented perpendicular to the loading direction [8]. Considering the applied stress of 28.6 MPa, Figs. 8.12-8.14 illustrate the progressive damage accumulation as a function of creep strain for three different grain boundary orientations. The grain boundary orientation is characterized by the parameter, ϕ, which is the angle between the normal to a cohesive element and the loading direction. In each figure, the evolution of the normalized area fraction of all cohesive elements with angle ϕ are plotted. $\phi = 0^\circ$ indicates that the cohesive elements are perpendicular to the loading direction, whereas, $\phi = 90^\circ$ indicates the cohesive elements are parallel to the loading direction and primarily undergoes sliding. At early stages of the creep process (5%, 12% and 19% of strain), grain boundaries show little damage for all three orientations. As the creep strain increases, more of the grain boundaries incur damage leading to a higher area fraction of grain boundaries with more damage. Two observations are made: First, a large majority of the cohesive

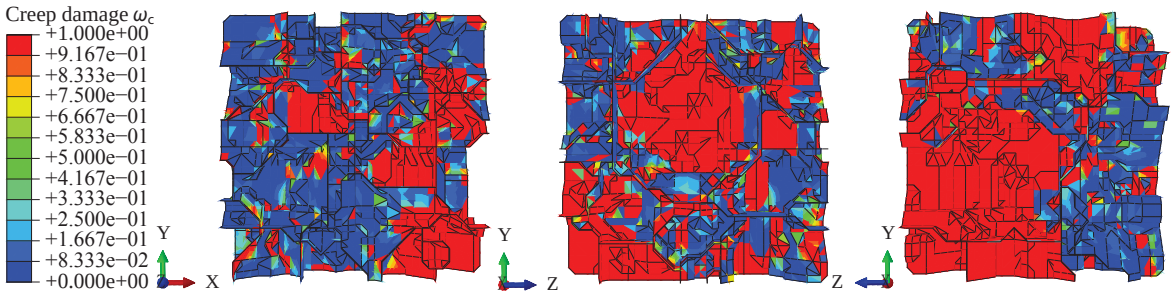

Fig. 8.11: Creep damage contour of the microstructure under 28.6 MPa loading at 30% of creep strain: (a) Front view, (b) Left view, and (c) Right view.

zone elements either display no significant damage or complete failure. This implies a sudden damage accumulation process at the local scale. Second, despite the fact that the grain boundaries perpendicular to the loading direction show a much greater extent of damage, those with different orientations and notably those parallel to the loading direction, also display damage. This indicates the possible presence and role of grain boundary sliding in addition to cavity growth.

8.3.2 Validation of creep strength predictions

In order to further validate the predictive capability of the proposed model against available experimental data, creep rupture times are computed for various stress levels at 950°C. Several numerical calculations for the 144-grain microstructure with different applied stress amplitudes (i.e., at 18.5 MPa, 24 MPa, 28.6 MPa, 35 MPa, 42 MPa, 52 MPa, 62.55 MPa, 68 MPa and 91 MPa) are performed. All experimental and simulated data are plotted together as logarithmic stress versus the Larson-Miller parameter (LMP) [109]. The basic equation of the LMP [109] is given by

$$\text{LMP} = T[\log(t) + P] \tag{49}$$

where T is the absolute temperature in Kelvin, t is the rupture time in hours, and the constant parameter P is taken as 20. Figure 8.15 shows the comparison between the experimental and predicted creep rupture data at different stress levels at 950°C. The ANL experiments are the rupture data used in the preceding calibration and microstructure analysis (24 MPa and 28.6 MPa), whereas Kim et al. [103] provides the creep rupture data collected from literature for several different stress levels. A reasonable match is observed for different stress levels when comparing the experimental data to the corresponding simulated results. The predicted rupture data of high stress levels (e.g., 68 MPa and 91 MPa) show a slightly shorter life than the experimental rupture life. A slightly longer rupture life is identified for the stress levels lower than 35 MPa. Some of the discrepancies between

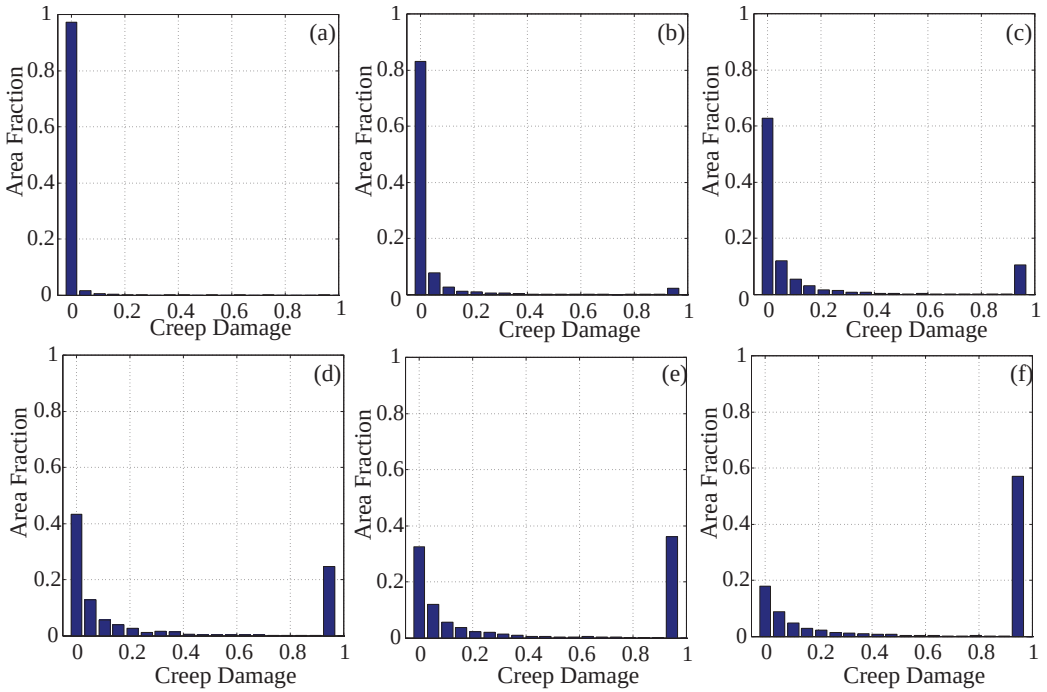

Fig. 8.12: Creep damage distribution of cohesive elements with their normal direction parallel to the creep stress axis ($\phi = 0°$): (a) 8%, (b) 12%, (c) 19%, (d) 22.4%, (e) 25%, and (f) 30% of creep strain.

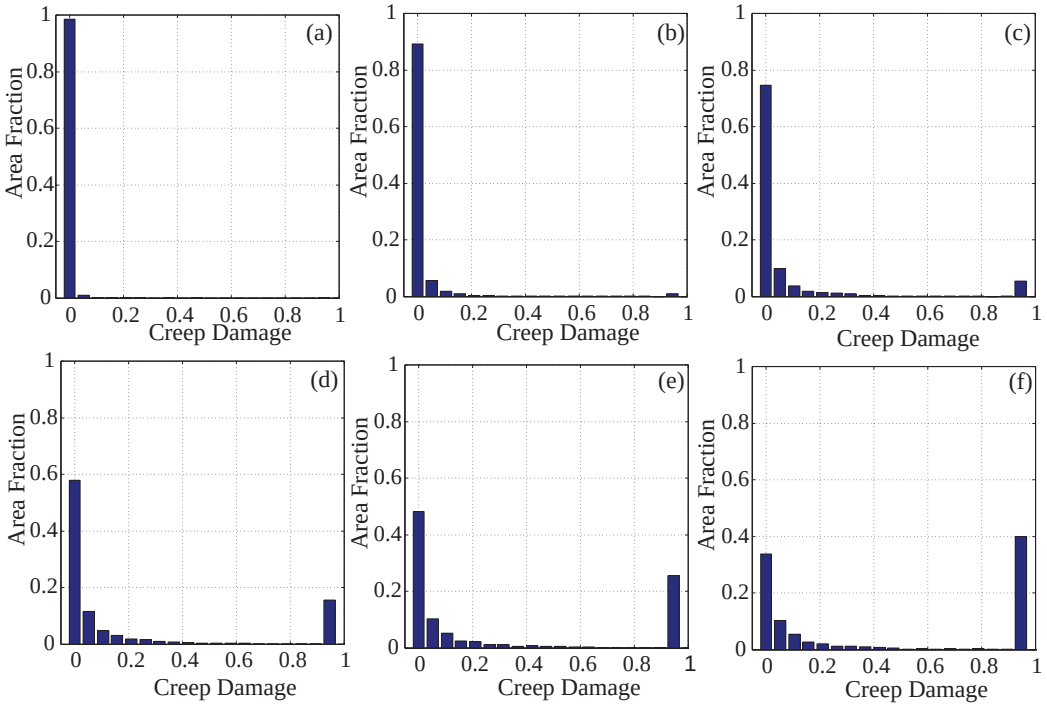

Fig. 8.13: Creep damage distribution of cohesive elements with the angle $\phi = 45°$ between their normal direction and the creep stress axis: (a) 8%, (b) 12%, (c) 19%, (d) 22.4%, (e) 25%, and (f) 30% of creep strain.

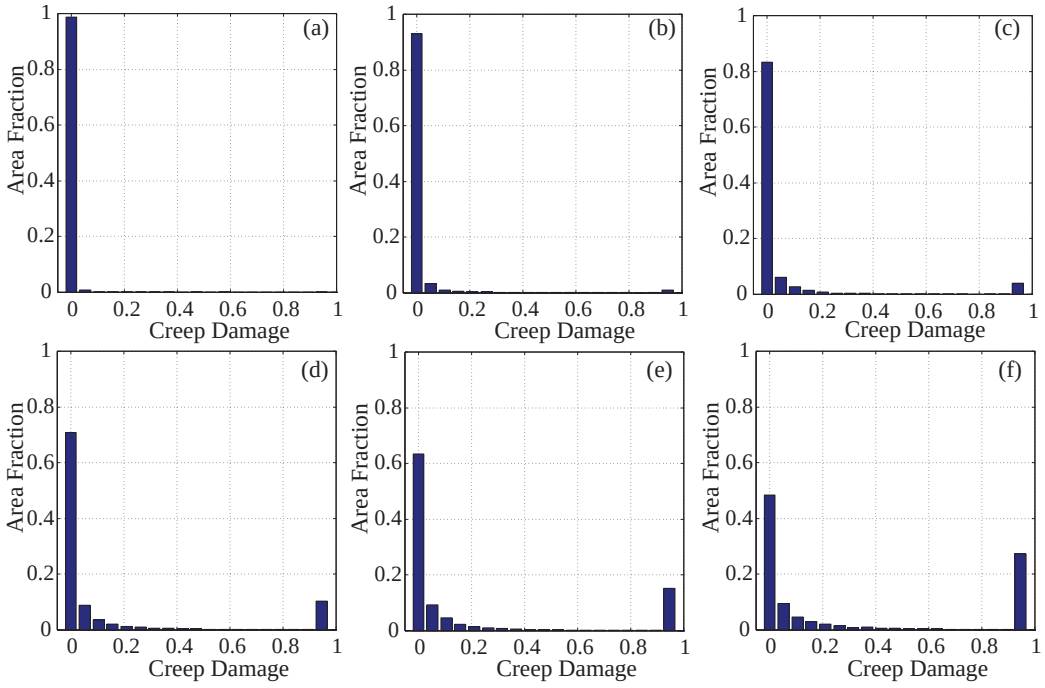

Fig. 8.14: Creep damage distribution of cohesive elements with their normal direction perpendicular to the creep stress axis ($\phi = 90°$): (a) 8%, (b) 12%, (c) 19%, (d) 22.4%, (e) 25%, and (f) 30% of creep strain.

the predicted and experimental rupture lives are attributed to the variability in the experiments, possibly due to material processing differences in experiments as they were performed independently. We note that the predictive capability of the proposed microstructural model could be further validated with direct microstructural observations, when such data becomes available.

8.4 Conclusions

In this chapter, we presented the formulation, implementation and calibration of a CPFE framework coupled with intergranular progressive damage accumulation modeled using the CZM approach. The proposed model considers the deformation mechanisms of dislocation climb and glide, along with grain boundary damage. The proposed model was employed to investigate the microstructural mechanisms contributing to the degradation of IN 617 under creep loading at 950℃.

The proposed model accurately captures the creep strain evolution and rupture in IN 617, and provides insight into the microscale stress, grain boundary damage distribution and their evolution. The microstructure simulations reveal that (1) Intergranular creep damage initiates primarily at triple junctions and near high misorientation angle boundaries; (2) The intergranular creep damage accumulation process is sudden at the microscale with intergranular elements displaying either no

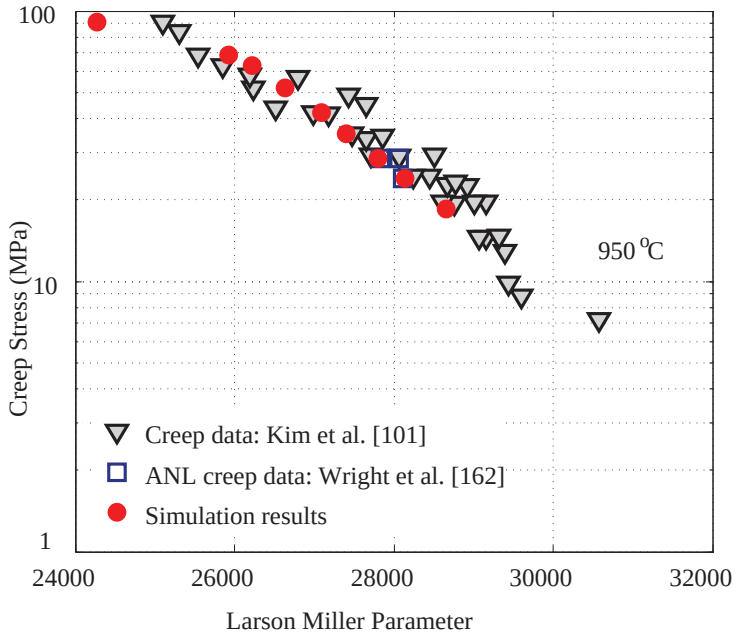

Fig. 8.15: Larson-Miller plot: comparison between simulated results and experimental creep data obtained from ANL creep tests and data from iterature.

significant damage or complete failure; (3) Some damage is observed at grain boundaries parallel to the loading direction, indicating a possible presence and role of sliding, in addition to cavity growth. Additionally, a good agreement is obtained between the experimental creep rupture data and corresponding simulations at several applied stress amplitudes. This illustrates the predictive capability of the proposed model.

A key interest is the application of the proposed CPFE-CZM model to understand the microstructural failure mechanisms under creep-fatigue loading. Creep-fatigue is a life limiting mechanism in a range of high temperature reactor applications [17, 8]. From the computational perspective, while such detailed CPFE-CZM based microstructure models can accurately capture failure mechanisms, they are computationally very costly. A future focus will be in the development of reduced order algorithms to efficiently simulate the response at a fraction of computational cost [130, 175] and employ such algorithms in the context of multiscale frameworks [131, 129, 172].

9 Microscale Modeling of Hybrid-Controlled tests in Nickel-based Superalloy IN 617 at High Temperature

In this section, the fully calibrated and verified CPFE-CZM model developed in Chapter 7 and 8 is adopted to investigate the hybrid-controlled tests with various hold stress magnitudes and hold times as well as a creep test with hold stress magnitude of 85 MPa from ASU.

9.1 Overview of Hybrid-Controlled Creep-Fatigue Testing and Modeling

9.1.1 Hybrid-controlled tests overview

The detailed experimental settings and loading profiles for the hybrid-controlled tests were described in Chapter 3. The goal of the hybrid-controlled tests is to generate creep dominated failure. In this chapter, the investigations focus on three hybrid-controlled tests as listed in Table 9.1. The numerical simulations were performed for the experiments that exhibited relatively small fatigue damage, since the focus of this project is on capturing creep dominated failure mechanisms.

Table 9.1: Hybrid-controlled tests to be investigated.

Test ID	Strain range ϵ_0 (%)	Hold stress σ_0 (MPa)	Hold Time T (s)	Cycles to failure
5	0.8	85	900	33
6	0.6	100	900	12
7	0.6	100	180	94

Figure 9.1(a) plots the first cycle response of the three hybrid-controlled tests together with one of the INL creep-fatigue tests (F-5 from Table 7.2), where the initial tension part of the curves are plotted in Fig. 9.1(b). It can be seen that ASU tests have approximately 10% higher elastic modulus and 15% higher yield stress than the INL tests. These differences possibly come from different material processing of the specimens used in testing. In order to capture the response of the hybrid-controlled tests from ASU, some of the glide and climb parameters (associated with the elastic modulus, yield stress) need to be recalibrated and discussed in detail below.

9.1.2 Hybrid-controlled test simulation realization using Abaqus-Python scripting

In experiments, both the strain and applied force are available in real time from the extensometer and the loading cell, hence switching from strain-controlled regime to stress-controlled regime,

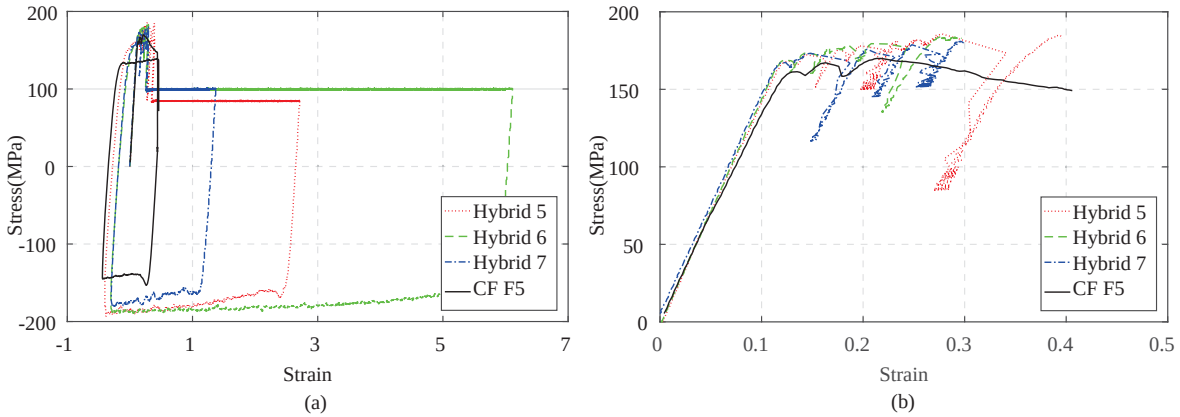

Fig. 9.1: Strain-strain curves of the Hybrid-controlled tests from ASU and INL creep-fatigue test F-5: (a) first cycle; (b) initial tension part.

or vice visa, could be automatically controlled. In contrast, automated switching from strain to stress controlled loading is not straightforward from the simulation perspective, as the information from overall stress-strain response needs to be tracked. In order to simulate the hybrid-controlled tests, Abaqus-Python scripting has been employed to switch between stress-controlled and strain-controlled loadings.

In order to implement the switch, An Abaqus restart analysis is a technique that allows the user to resume a finite element simulation from a certain point of an existing simulation, with the flexibly to redefine the loading or boundary conditions. To restart an simulation, one need to store necessary information related with the model definition and save to the hard disk at user–specified time point (restart point), from which, the restart analysis can be launched. The restart analysis either continues the previous analysis or adds additional information into the analysis (e.g., changes in loading or boundary conditions).

To be more specific for implementing the switch between stress- and strain controlled loadings in an automated manner, it is necessary to monitor the applied total force in strain controlled loading and trigger the switching when the applied total forces reaches the designated value. This can be achieved using the Abaqus-Python scripting combined with the restart analysis technique by two alternative methods: (1) constantly access Abaqus simulation database file (i.e., .odb file) at the end of each increment around the region where switching is expected and terminate the analysis and write restart file once the switching criterion (e.g., applied force reaches designated value) is reached; (2) conduct an analysis step longer than needed with frequent restart points requested (e.g., during the unloading to hold stress, unload to a point where the resulting stress is lower than the hold stress) and access the Abaqus database file at the end of simulation to determine the appropriate restart point. In the current work, the latter option is utilized for the hybrid-controlled

test simulation, as frequent accessing to the odb file (i.e., launching Abaqus CAE kernel and file I/O operations) during the simulation causes significant overhead and is not computationally efficient.

The implementation of the multiple-cycle hybrid-controlled test simulation is shown in Fig. 9.2. The simulation starts with an initial Abaqus analysis with the input file *Start.inp*, which contains the initial strain-controlled tension and unloading steps. The unloading is sufficient enough such that the applied stress drops bellow the critical value RF_c corresponding to the the hold stress σ_0. Restart point is requested for every increment in the unloading step. Then the Abaqus-Python scripting interface is used to access the simulation database file *Start.odb* to extract the reaction force history at the fixed end of the RVE (which has a magnitude equal to the applied force). A restart point is determined at which the reaction force is equal to RF_c and an restart file, *Res_i_1.inp* (i indicates cycle number and is 1 currently for the first cycle) is prepared. The restart file contains the restart point and also defines the step for the stress hold where only one restart point at the end of the step is requested to allow the restart analysis afterwards. A restart file *Res_i_2.inp* is then written using the final increment of the stress hold step as restarting point and contains the unloading (to strain $-0.5\epsilon_0$), reloading (to strain $0.5\epsilon_0$) and unloading steps. The above process is repeated until the total number of cycles to be simulated (N) is reached. The simulation process is implemented in an automatic manner and all restart and restart frequency are appropriately chosen to keep record of the necessary information, while minimizing the cost from file I/O operations.

9.2 Model Calibration and Verification

9.2.1 Recalibration of the glide and climb parameters

As demonstrated in Fig. 9.1, the ASU experiments show higher elastic modulus and yield stress than the INL experiments employed in previous calibration studies. In order to accommodate these differences, we first increase the elastic parameters (C_{11}, C_{12} and C_{44} by 10%) to match the change in the elastic modulus, and then recalibrate parameters $\bar{S}^\alpha$, S_0^α and $\hat{\tau}_{0c}$ using the first cycle response of hybrid-controlled test 7 in Table 9.1 and the creep test with 85 MPa hold stress. The recalibration of the crystal plasticity model parameters are performed for the part of the creep test prior to the onset of tertiary creep.

Figure 9.3 shows the comparison between simulations and experiments of the creep test and hybrid-controlled test 7 following the calibration. The calibrated parameters are listed in Table 9.2. The simulations accurately capture the first cycle response of the hybrid-controlled test 7 (Fig. 9.3(a)) and the creep response at stress magnitude until the beginning of tertiary creep (9.3 (b)). The ability to capture the strain accumulation in the tertiary creep regime necessitates the

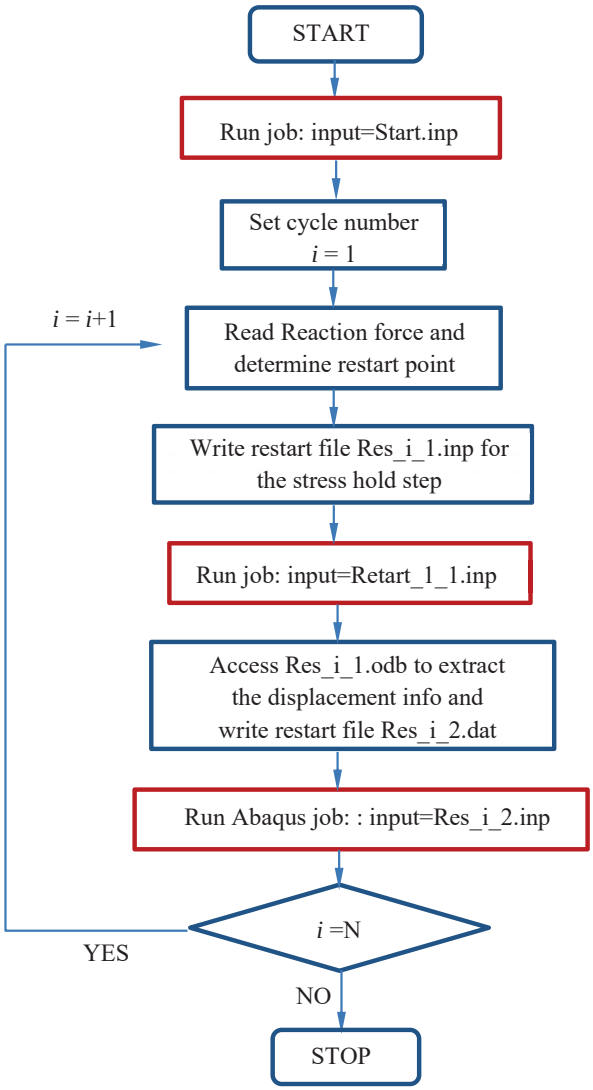

Fig. 9.2: Flow chart of the hybrid-controlled test simulation in Abaqus (red boxes indicates Abaqus simulations and blue boxes are Python scripts).

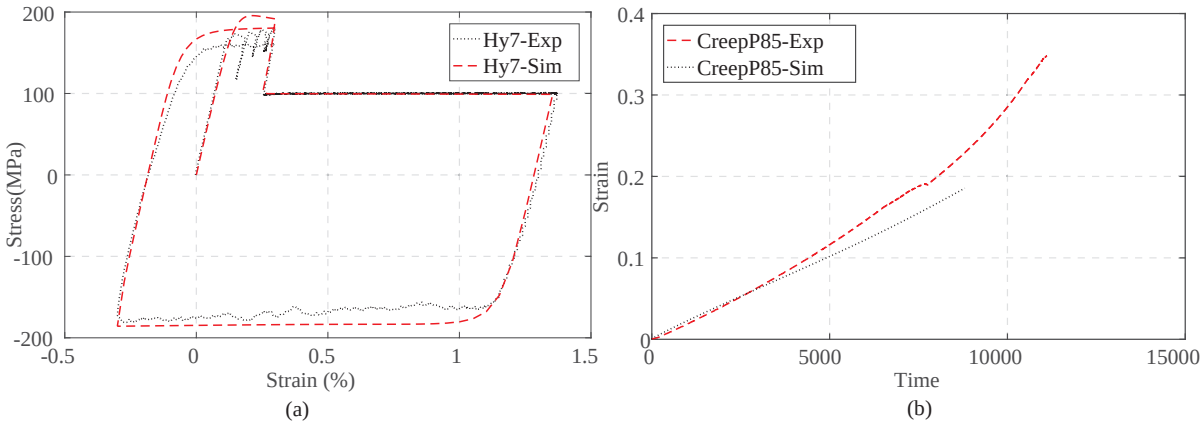

Fig. 9.3: Calibrated results of: (a) first cycle of hybrid-controlled test 7; (b) creep test.

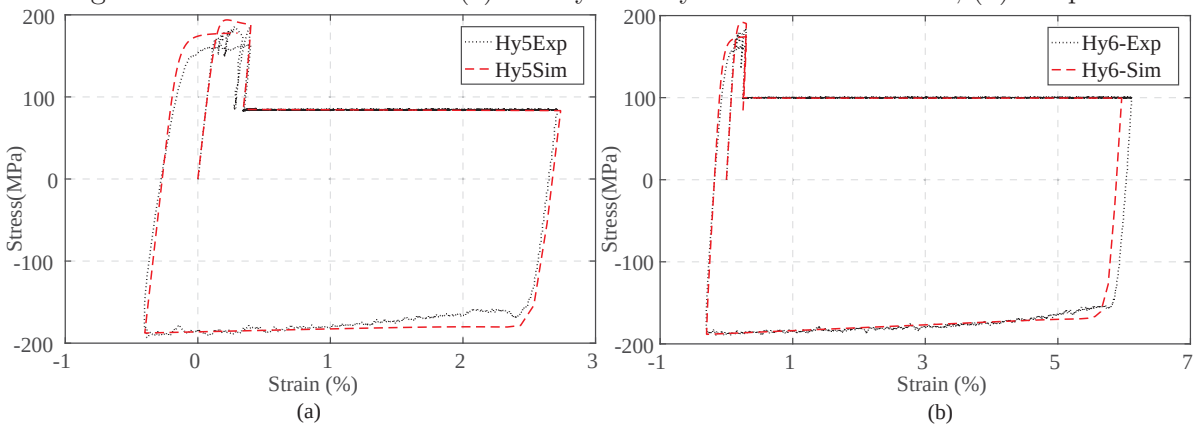

Fig. 9.4: Verification of the recalibrate CPFE model: (a) hybrid-controlled test 5; (b) hybrid-controlled test 6.

calibration of the cohesive zone model parameters as well. We note that the simulation in Fig. 41(b) does not include the cohesive zone models at the grain boundaries.

Table 9.2: Recalibrated crystal plasticity parameters.

C_{11} (MPa)	C_{12} (MPa)	C_{44} (MPa)	$\bar{S}^{\alpha}$ (MPa)	S_0^{α}	$\hat{\tau}_{0c}$ (Pa)
176.64	112.20	81.24	181.47	103.49	6750

To thoroughly validate the model, the first cycle response of the hybrid-controlled tests 5 and 6 are simulated and compared to experimental data as shown in Fig. 9.4. It is observed that the model captures the response of test 5 accurately, while it predicts slightly less creep strain in the stress hold stage (Fig. 9.4(b)). Overall, the simulation provides a reasonable match with the experiments.

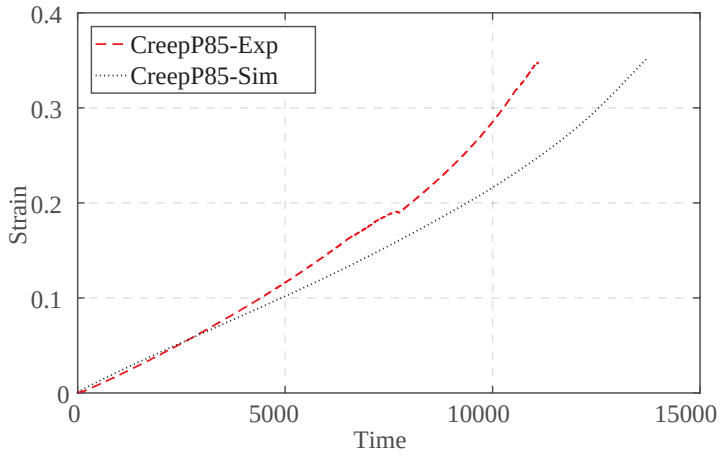

Fig. 9.5: Recalibrated creep response at hold stress magnitude of 85 MPa.

9.2.2 Recalibration of the CZM parameters

In order to capture the intergranular damage well, we slightly recalibrate the CZ parameters using the creep test under applied stress magnitude of 85 MPa. Since the grains show increased modulus and yield stress, the threshold traction, T_c and parameter C are expected to increase to capture the creep response of the creep test at 85 MPa.

The recalibrated parameters T_c and C are listed in Table 9.3 and the strain-time response is compared with experiment in Fig. 9.5(a). Reasonable match between the simulation and the experimental creep test at hold stress 85 MPa is observed.

Table 9.3: Recalibrated CZ parameters.

C (Pa)	T_c (Pa)
$8.87e9$	38.5

9.3 Microscale Analysis of the Hybrid-Controlled tests

In this section, the automated multiple cycle simulation algorithm described above employed to model the multiple cycle response of the hybrid-controlled tests. In view of the high computational costs of cyclic simulations with CZM, we focus on hybrid-controlled test 6 since it has a relatively small number of cycles to failure. The recalibrated CPFE and CZM parameters are used in this simulation.

Figure 9.6 demonstrates the stress-strain response comparison between simulation and experiment at the 6th and 8th cycle, respectively. It is found that the simulation accurately captures the

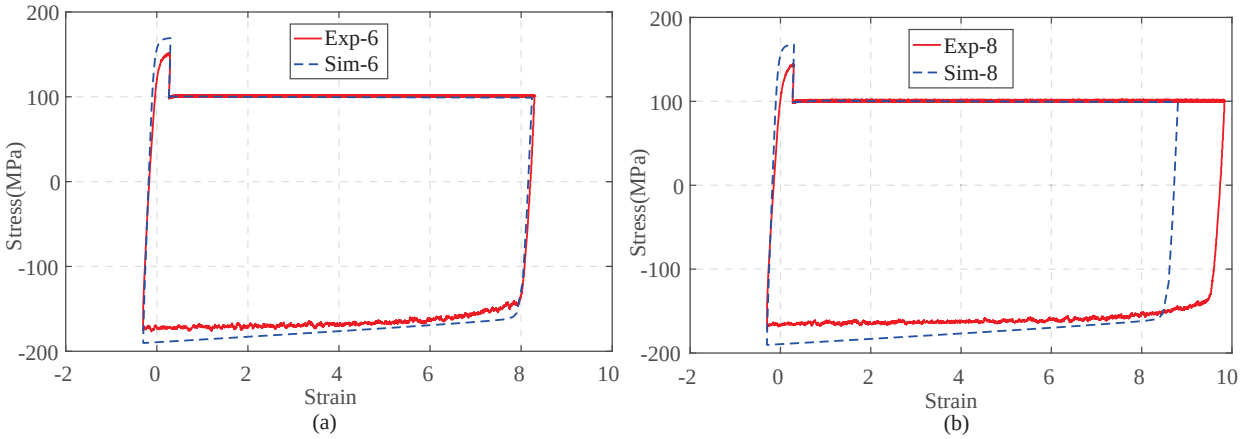

Fig. 9.6: Stress-strain response comparison at: (2) 6th cycle and ; (b) 8th cycle of hybrid-controlled test 6.

response of the 6th cycle but starts to deviate at the 8th cycle. The microstructure deformation as well as the grain boundary damage distribution are plotted in Fig. 9.7 for the 6th cycle, where negligible grain boundary damage is observed, indicating that the creep strain up until the 6th cycle is mainly due to viscoplastic deformation instead of damage.

To further identify the source of creep strain discrepancy in the 8th cycle, the experimental creep strain as a function of cycle number is plotted in Fig. 9.8. Dramatic increase of creep strain is observed starting from the 6th cycle, which indicates damage accumulation significantly contributes to the creep strain after the 6th cycle. However, the simulated deformation and damage of the 8th cycle in Fig. 9.9 shows only slightly grain boundary damage. This explains that the underpredicted creep strain in the 8th cycle is due to under predicted grain boundary damage. The current CZ model demonstrates a more sudden increase in damage growth rate compared to a more gradual accumulation of strain observed in the experiments at later cycles. Potential improvement of the predicted strain in the later cycles could be achieved if the CZ parameters are further calibrated to yield a more gradual accumulation of damage. One possibility in this regard is a change in the exponential damage model employed in this research. The exponential model is associated with a high rate of damage accumulation in the post peak region. A model that exhibits a slower damage growth in the post peak region will be investigated in the future.

9.4 Conclusions

In this chapter, we adopted the combined CPFE-CZM model previously developed to study the response of the hybrid-controlled tests conducted at ASU. An automated multiple cycle hybrid-controlled test modeling approach was implemented using the Abaqus-Python scripting interface to

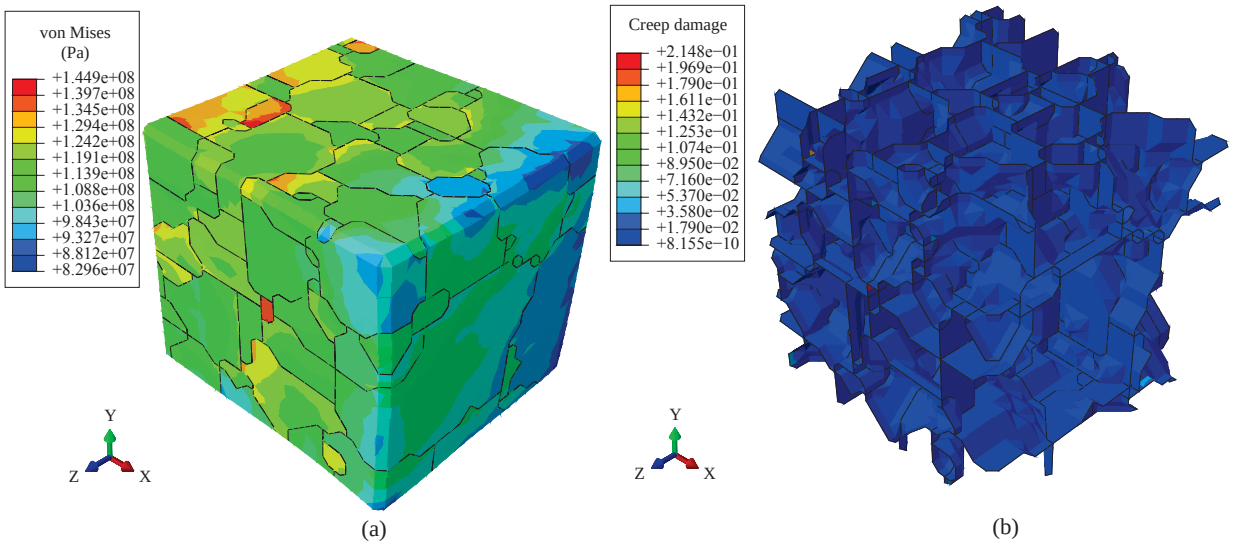

Fig. 9.7: (a) Deformation and (b) grain boundary damage at the end of stress hold of the 6th cycle.

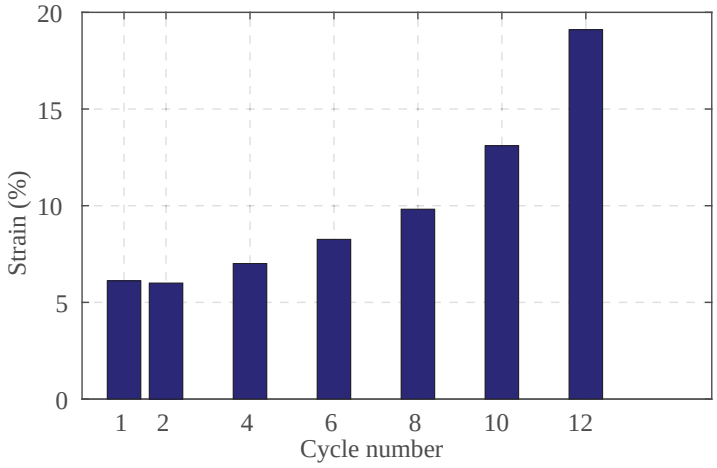

Fig. 9.8: Creep strain at the end of stress hold vs. cycle number.

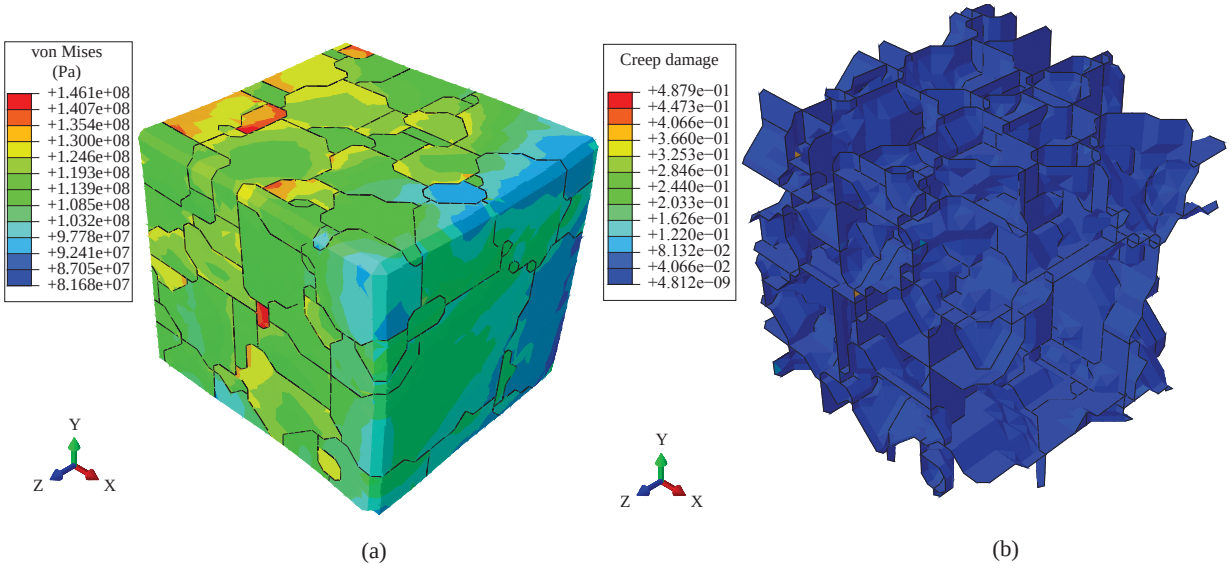

Fig. 9.9: (a) Deformation and (b) grain boundary damage at the end of stress hold of the 8th cycle.

facilitate the simulation. Due to possible material processing difference by separate manufactures, the hybrid-controlled tests show relatively higher elastic modulus and yield stress compared with the INL tests. A subset of the CPFE and CZM parameters were recalibrated to reflect the material differences. The recalibration was conducted in an progressive manner to focus first on the creep response before damage initiation and the first cycle responses of the hybrid-controlled tests and then on the creep response until failure. The recalibrated model was further utilized to simulate the multiple cycle response of the hybrid-controlled test with hold stress 100 Mpa and hold time 900 s. The model captures well the stress-strain response up until the middle cycle to failure, while starts to have discrepancies later on. Microscale analysis indicates the discrepancy in later cycles is due to the under predicted grain boundary damage, which can be potentially improved when more creep test data become available to allow more thorough probing of the CZ parameters at this high stress level.

10 Conclusions

The elevated temperature creep-fatigue behavior of Alloy 617 was investigated in this study, using a combination of experimental testing, image-based damage analysis, microstructure based constitutive modeling and life-prediction. The initial problem of generating creep-dominated creep-fatigue interaction was resolved by selecting a non-traditional loading profile with force-controlled tensile hold periods. The failed test specimens from various tests were analyzed using Scanning Electron Microscopy (SEM), Energy Dispersive Spectroscopy (EDS), and Electron Backscatter Diffraction (EBSD). The area fraction of creep-induced voids and average length of fatigue-induced surface cracks were quantified to find correlations between creep and fatigue damage. Unlike the time fraction rule, the image based damage analysis indicated a clear trend in creep-fatigue interaction. A new life-prediction methodology based on an effective time fraction was proposed as an alternative to the traditional time fraction rule. Finally, a unified viscoplastic model with a damage variable was implemented to obtain an energy-based life prediction. Several major conclusions are listed below:

- Strain-controlled testing is not able to generate creep-dominant creep-fatigue (CF) testing results due to the rapid stress relaxation of Alloy 617 at high temperatures. On the contrary, pure force-controlled testing produces cyclic ratchetting and is therefore not ideal for the CF investigation. Hybrid controlled testing with stress hold at peak strain tends to produce very large and non-representative CF interaction due to the holding stress exceeding the initial yield stress. The proposed hybrid control with a separately controlled holding stress appears to be well suited for the investigated material and temperature range to generate desired creep and fatigue portions.

- Detailed imaging analysis showed that the microstructural damage features are not correlated with the classical damage diagram parameters. Specifically, the void density is not correlated with the classical time fraction and is correlated with the time spent for the net creep strain increment. The crack length is well correlated with the cycle fraction in fatigue. Thus, the application of the classical time fraction approach is questionable for the investigated load spectrum as it is not supported by the physical damage patterns.

- An effective time fraction approach based on the image analysis shows good agreement for the life prediction under both hybrid control and strain-controlled testing. The scatter of life factor of three is observed for the in-house testing and literature experimental data. The empirical damage interaction diagram using the proposed effective time fraction approach

shows a bi-linear curve for the creep and fatigue damage.

- A unified constitutive and damage model is developed by coupling the hysteresis energy with the softening behavior of the material. The fatigue hysteresis energy and creep hysteresis energy shows monotonic relationship with respect to the Youngs modulus and creep law exponent. A nonlinear power damage summation rule is proposed and shows that an exponent of 1/3 for the two hysteresis energies. The final failure prediction is in good agreement with experiments.

Through the development and exercising of the combined CPFE-CZM model, it can be concluded:

- Solute-drag creep effect due to the interaction between dislocation and mobile solutes at high temperature is responsible for the transient stress softening observed at the initial tension part of the first cycle fatigue and creep-fatigue tests and its persistent re-emerging at each creep-fatigue tests after stress hold. This transient phenomenon is accurately modeled through the proposed slip resistance evolution model.

- Dislocation climb is an import deformation mechanism of Alloy 617 at high temperature. Incorporation of this mechanism is important in capture the creep response up until the onset of significant grain boundary damage, especially when the applied stress magnitude is much lower than yield stress.

- Combined CPFE-CZM model is an effective method in capturing the viscoplastic deformation and well as intergranular damage induced rupture of Alloy 617 at high temperature under creep loading. Exercising of the CPFE-CZM model on high fidelity microstructure reveals the following observations about the damage initiation and propagation characteristics: (1) Intergranular creep damage initiates primarily at triple junctions and near high misorientation angle boundaries; (2) The intergranular creep damage accumulation process is sudden at the microscale with intergranular elements displaying either no significant damage or complete failure; (3) Some damage is observed at grain boundaries parallel to the loading direction, indicating a possible presence and role of sliding, in addition to cavity growth. Additionally, a good agreement is obtained between the experimental creep rupture data and corresponding simulations at several applied stress amplitudes. This illustrates the predictive capability of the proposed model.

11 Research Output

Students and postdoctoral associates research associates trained

[1] Mr. Fraaz Tahir, fully supported by this project between February 2014 and February 2017, currently Research Assistant at Arizona State University, Tempe, AZ.

[2] Mr. Dong Pan, fully supported by this project between August 2014 and January 2017, currently Research Assistant at Arizona State University, Tempe, AZ.

[3] Ms. Sonam Dahire, partially suppported by this project from August 2014 to August 2015, currently Research Assistant at Arizona State University, Tempe, AZ.

[4] Dr. Robert Crouch, fully supported by this project between April 2014 and August 2014 at Vanderbilt University, currently at Altair Engineering, Nashville, TN.

[5] Dr. Yumeng Li, fully supported by this project between February 2015 and December 2015 at Vanderbilt University, currently Assistant Professor at Wichita State University, Wichita, KS.

[6] Dr. Van Tung Phan, fully supported by this project between February 2016 to January 2017 at Vanderbilt University, currently Researcher at Argonne National Laboratory , Lemont, IL.

[7] Mr. Xiang Zhang, partially supported by this project at Vanderbilt University, currently Researcher Assistant at Vanderbilt University, Nashville, TN.

Journal publications

[1] F. Tahir and Y. Liu. A New Experimental Testing Method for Investigation of Creep-Dominant Creep-Fatigue Interaction in Alloy 617 at 950C. *Int. J. Press. Vessel. Pip.*, submitted, 2016

[2] X. Zhang and C. Oskay. Polycrystal Plasticity Modeling of Nicke-based Superalloy IN 617 Subjected to Cyclic Loading at High Temperature. *Modelling Simul. Mater. Sci. Eng.*, 24:055009, 2016

[3] X. Zhang and C. Oskay. Microscale Modeling of Creep Deformation and Rupture in Nickel-based Superalloy IN 617 at High Temperature. *Mech. Mater.*, submitted, 2017

[4] F. Tahir and Y. Liu. An Effective Time Fraction Approach for Creep-Fatigue Life Prediction of Alloy 617 at High Temperatures. *J. Nucl. Mater.*, submitted, 2017

[5] F. Tahir, S. Dahire and Y. Liu. Image-based Creep-Fatigue Damage Mechanism Investigation of Alloy 617 at 950C. *Mat. Sci Eng. A*, 679, 391-400, 2017

Conference proceedings

[1] X. Zhang, V. T. Phan and C. Oskay, Microstructural Creep, Fatigue and Creep-Fatigue modeling of Nickel-based Superalloy Inconel 617 at High Temperature, Proceedings of the High Temperature Reactor Technology (HTR) Meeting 2016 , Las Vegas, NV, November 7-10, 2016.

[2] F. Tahir and Y. Liu, Investigation of Creep-Fatigue Damage in Alloy 617 at High Temperatures. MRS Spring Meeting, Phoenix, AZ, 2017.

[3] F. Tahir and Y. Liu, Image-based Mechanism Explanation of Creep-Fatigue Fracture of Alloy 617 at High Temperature. 14th International Conference on Fracture, Rhodes, Greece, 2017

[4] F. Tahir and Y. Liu, Development of Creep Dominant Creep-Fatigue Testing for Alloy 617. 57th AIAA/ASCE/AHS/ASC Structures, Structural Dynamics, and Materials Conference, San Diego, CA, 2016

[5] F. Tahir and Y. Liu, Creep-Fatigue Life Prediction of Alloy 617 at 950℃ using an Effective Hold Time Approach. Transactions of the ANS Winter Meeting and Nuclear Technology Expo, Las Vegas, NV, 2016

[6] F. Tahir and Y. Liu, Development of Creep-Dominant Creep-Fatigue Tests for Alloy 617. Transactions of ANS Winter Meeting and Nuclear Technology Expo, Washington, DC, Vol. 113, Pg. 133-144, 2015

Conference presentations

[1] X. Zhang and C. Oskay. Fatigue and Creep-Fatigue Modeling of Alloy 617 at High Temperature. ASME 2015 International Mechanical Engineering Congress & Exposition, Houston, TX, November 13-19, 2015

[2] X. Zhang V. T. Phan and C. Oskay. Microstructural Creep, Fatigue and Creep-Fatigue Modeling of Nickel-based Superalloy IN 617 at High Temperature. ANS 8th International Topical Meeting on High Temperature Reactor Technology, Las Vegas, NV, November 7-10, 2016

[3] X Zhang, C. Oskay. Microscale modeling of creep deformation and rupture using cohesive zone-crystal plasticity finite element analysis. ASCE 2017 Engineering Mechanics Institute Conference, San Diego, CA, June 4-7, 2017

12 Bibliography

[1] P. Rodriguez and K.B.H. Rao. Nucleation and growth of cracks and cavities under creep-fatigue interaction. *Prog. Mater. Sci.*, 37:403–480, 1993.

[2] A. Dasgupta. Solder creep-fatigue analysis by an energy-partitioning approach. *J. Electron. Packag.*, 114:152–160, 1992.

[3] D. Chapin, S. Kiffer, and J. Nestell. The very high temperature reactor: A technical summary. Technical report, MPR Assoc., 2004.

[4] J.M. Corum and J.J. Blass. Rules for design of alloy 617 nuclear components to very high temperatures. Technical report, Oak Ridge Natlional Lab, 1991.

[5] X. Chen, M.A. Sokolov, S. Sham, D.L. Erdman, J.T. Busby, K. Mo, and J.F. Stubbins. Experimental and modeling results of creep-fatigue life of inconel 617 and haynes 230 at 850c. *J. Nucl. Mater.*, 432:94–101, 2013.

[6] J.A. Simpson, J.K. Wright, and L.J. Carroll. Novel experiments to characterize creep-fatigue degradation in vhtr alloys. Technical report, Idaho National Laboratory, 2013.

[7] L. Carroll and M. Carroll. Creep-fatigue behavior of alloy 617 at 850 and 950°C. Technical report, Idaho National Laboratory, 2015.

[8] L.J. Carroll, C. Cabet, M.C. Carroll, and R.N. Wright. The development of microstructural damage during high temperature creep-fatigue of a Nickel alloy. *Int. J. Fatigue*, 47:115–125, 2013.

[9] ASME. *Boiler and Pressure Vessel Code, Section III, Sub-Section.* NH, New York, 2001.

[10] W.Z. Zhuang and N.S. Swansso. Thermo-mechanical fatigue life prediction: A critical review. Technical report, DSTO Aeronautical and Maritime Research Laboratory, 1998.

[11] RCC-MRx. Design and construction rules for mechanical components of nuclear installations, 2014. AFCEN.

[12] R.A. Ainsworth. The development of microstructural damage during high temperature creep-fatigue of a Nickel alloy. *Int. Mater. Rev.*, 51:107–126, 2006.

[13] Y. Takahashi. Study on creep-fatigue evaluation procedures for high-chromium steels-part i: Test results and life prediction based on measured stress relaxation. *Int. J. Press. Vessel. Pip.*, 85:406–422, 2008.

[14] Y. Takahashi. An improved method for calculation of creep damage during creepfatigue cycling. *Mater. Sci. Technol.*, 23:1461–1470, 2007.

[15] W. Hoffelner. Creep-fatigue life determination of grade 91 steel using a strain-range separation method. *in: ASME 2009 Press. Vessel. Pip. Div. Conf.*, pages 1–5, 2009.

[16] H.B.S. Rao, , H-P Meurer, and H. Schuster. Creep-fatigue interaction of lnconel 617 at 950c in simulated nuclear reactor helium. *Mater. Sci. Eng. A*, 104:37–51, 1988.

[17] C. Cabet, L. Carroll, and J. Wright. Low cycle fatigue and creep-fatigue behavior of Alloy 617 at high temperature. *J. Press. Vess. T.*, 135:061401.1–061401.7, 2013.

[18] H. Nickel and F. Schubert. Development and qualification of materials for components for high-temperature gas-cooled reactor. *Nucl. Eng. Des.*, 121:183–192, 1990.

[19] B. Fournier, M. Sauzay, C. Caes, M. Noblecourt, M. Mottot, A. Bougault, and V. Rabeau. Creep-fatigue-oxidation interactions in a 9Cr-1Mo martensitic steel. part I: Effect of tensile holding period on fatigue lifetime. *Int. J. Fatigue*, 30:649–662, 2008.

[20] M.E.M.E. Kassner and J.S. Tiley. *Fundamentals of Creep in Metals and Alloys*. Elsevier, 2008.

[21] E.P. Esztergar. Creep-fatigue interaction and cumulative damage evaluations for type 304 stainless steel. Technical report, Oak Ridge Natlional Lab, 1972.

[22] G.J. Lloyd and J. Wareing. Life prediction methods for combined creep-fatigue endurance. *Met. Technol.*, 8:297–305, 1981.

[23] J.K. Wright. Draft asme boiler and pressure vessel code section III, division 5, section hb, subsection b, code case for alloy 617 and background documentation. Technical report, Idaho National Laboratory, 2015.

[24] S.F. DiMartino, R.G. Faulkner, S.C. Hogg, S. Vujic, and O. Tassa. Characterisation of microstructure and creep properties of alloy 617 for high-temperature applications. *Mater. Sci. Eng. A.*, 619:77–86, 2014.

[25] S.K. Sharma, G.D. Ko, F.X. Li, and K.J. Kang. Oxidation and creep failure of alloy 617 foils at high temperature. *J. Nucl. Mater*, 378:144–152, 2014.

[26] T.C. Totemeier and H. Tian. Creep-fatigueenvironment interactions in INCONEL 617. *Mater. Sci. Eng. A.*, 468-470:81–87, 2007.

[27] S. SCHLEGEL, S. HOPKINS, E. YOUNG, J. COLE, T. LILLO, and M. FRARY. Precipitate redistribution during creep of Alloy 617. *Metall. Trans. A*, 40A:2812–2823, 2009.

[28] F. Tahir and Y. Liu. Development of creep-dominant creep-fatigue testing for alloy 617. In *in: 57th AIAA/ASCE/AHS/ASC Struct. Struct. Dyn. Mater. Conf*, San Diego, California, USA., 2012.

[29] R.N. Wright. High temperature materials characterization database. Technical report, Idaho National Laboratory, 2015.

[30] R. Campbell. Creep/fatigue interaction correlation for 304 stainless steel subjected to strain-controlled cycling with hold times at peak strain. *J. Eng. Ind.*, 93:887–892, 1971.

[31] X.-L. Yan, X.-C. Zhang, S.-T. Tu, S.-L. Mannan, F.-Z. Xuan, and Y.-C. Lin. Review of creepfatigue endurance and life prediction of 316 stainless steels. *Int. J. Press. Vessel. Pip.*, 126-127:17–28, 2015.

[32] E.L. Robinson. Effect of temperature variation on the creep strength of steel, trans. *Trans. ASME*, 60:253–259, 1938.

[33] R.H. Priest and E.G. Ellison. A combined deformation map-ductility exhaustion approach to creep-fatigue analysis. *Mater. Sci. Eng.*, 49:7–17, 1981.

[34] R. Hales. a method of creep damage summation based on accumulated strain for the assessment of creep-fatigue endurance. *Fatigue Fract. Eng. Mater. Struct.*, 49:121–135, 1983.

[35] Y. Takahashi and D.G. BilalDogan. Systematic evaluation of creep-fatigue life prediction methods for various alloys. *J. Press. Vessel Technol.*, 49:121–135, 2013.

[36] S.S. Manson and G.R. Halford. Creep-fatigue analysis by strain-range partitioning. Technical report, NASA, 1971.

[37] E.H. Wong, W.D. vanDriel, A. Dasgupta, and M. Pecht. Creep fatigue models of solder joints: A critical review. *Microelectron. Reliab.*, 59:1–12, 2015.

[38] T. Asayama. Update and improve subsection nh-alternative simplified creep-fatigue design methods. Technical report, Japan Atomic Energy Agency, 2011.

[39] L.J. Carroll, R.N. Wright, T.-L. Sham, N.J. Lybeck, and R.N. Wright. Determination of the creep-fatigue interaction diagram for alloy 617. In *Proc. ASME 2016 Press. Vessel. Pip. Conf.*, pages 1–10, 2016.

[40] F. Tahir, S. Dahire, and Y. Liu. Image-based creep-fatigue damage mechanism investigation of alloy 617 at 950°C. *Mater. Sci. Eng. A*, 679:391–400, 2017.

[41] S. Taira. Lifetime of structures subjected to varying load and temperature. In N.J. Hoff, editor, *Creep Struct. Colloq*, pages 96–124. Springer Berlin Heidelberg, Berlin, Heidelberg, 1962.

[42] J.L. Chaboche and G. Rousselier. On the plastic and viscoplastic constitutive equations, part I: Rules developed with internal variable concept. *ASME J. Press. Vessel Technol.*, 105:153–158, 1983.

[43] C.J. Hyde, W. Sun, T.H. Hyde, J.P. Rouse, T. Farragher, N.P. ODowd, and S.B. Leen. Cyclic viscoplasticity testing and modeling of a service-aged p91 steel. *J. Press. Vessel Technol.*, 136: 44501, 2014.

[44] J. Lemaitre and J.-L. Chaboche. *Mechanics of Solid Materials*. Cambridge University Press, 1990.

[45] B. Vermeulen J. Tong. The description of cyclic plasticity and viscoplasticity of waspaloy using unified constitutive equations. *Int. J. Fatigue*, 25:413–420, 2003.

[46] J. Tong, Z.L. Zhan, and B. Vermeulen. Modelling of cyclic plasticity and viscoplasticity of a nickel-based alloy using chaboche constitutive equations. *Int. J. Fatigue*, 26:829–837, 2004.

[47] Z. Zhan, U.S. Fernando, and J. Tong. Constitutive modelling of viscoplasticity in a nickel-based superalloy at high temperature. *Int. J. Fatigue*, 30:1314–1323, 2008.

[48] J.-T. Yeom, S.J. Williams, I.-S. Kim, and N.-K. Park. Unified viscoplastic models for low cycle fatique behavior of waspaloy. *Met. Mater. Int.*, 7:233–240, 2001.

[49] M. Yaguchi, M. Yamamoto, and T. Ogata. A viscoplastic constitutive model for nickel-base superalloy, part 1: Kinematic hardening rule of anisotropic dynamic recovery. *Int. J. Plast.*, 18:1083–1109, 2002.

[50] R. Ahmed, P.R. Barrett, and T. Hassan. Unified viscoplasticity modeling for isothermal low-cycle fatigue and fatigue-creep stress-strain responses of haynes 230. *Int. J. Solids Struct.*, 89: 131–145, 2015.

[51] L.J. Carroll, R.N. Wright, T.-L. Sham, N.J. Lybeck, and R.N. Wright. Constitutive modeling of high temperature uniaxial creep-fatigue and creep-ratcheting responses of alloy 617. In *Proc. ASME 2013 Press. Vessel. Pip. Conf.*, page 97251, 2013.

[52] T.-L. Sham and K.P. Walker. Preliminary development of a unified viscoplastic constitutive model for alloy 617 with special reference to long term creep behavior. In *ASME Proceedings, Materials and Components*, volume 2, page 97251, 2008.

[53] R. Hales, S.R. Holdsworth, M.P. ODonnell, I.J. Perrin, and R.P. Skelton. A code of practice for the determination of cyclic stress-strain data. In *Mater. High Temp.*, volume 19, pages 165–185, 2002.

[54] V.G. Ramaswamy, D.C. Stouffer, and J.H. Laflen. A unified constitutive model for the inelastic uniaxial response of rene' 80 at temperatures between 538c and 982c. In *J. Eng. Mater. Technol.*, volume 112, pages 280–286, 1990.

[55] J. Chaboche. A review of some plasticity and viscoplasticity constitutive theories. *Int. J. Plast. Special Issue in Honor of Jean-Louis Chaboche*, 24:1642–1693, 2008.

[56] R. Krishna, H. V. Atkinson, S. V. Hainsworth, and S.P. Gill. Gamma prime precipitation, dislocation densities, and tin in creep-exposed inconel 617 alloy. *Metall. Mater. Trans. A*, 24: 178–193, 2016.

[57] D. Tytko, P.P. Choi, J. Klwer, A. Kostka, G. Inden, and D. Raabe. Microstructural evolution of a Ni-based superalloy (617b) at 700c studied by electron microscopy and atom probe tomography. *Acta. Mater.*, 60:1731–1740, 2012.

[58] X. Chen, Z. Yang, M.A. Sokolov, D.L. Erdman III, K. Mo, and J.F. Stubbins. Effect of creep and oxidation on reduced fatigue life of Ni-based alloy 617 at 850c. *J. Nucl. Mater.*, 444: 393–403, 2014.

[59] F.P.E. Dunne and D.R. Hayhurst. Continuum damage based constitutive equations for copper under high temperature creep and cyclic plasticity. *Proc. R. Soc. A.*, 437:545–566, 1992.

[60] W. Wang, P. Buhl, A. Klenk, and Y. Liu. A continuum damage mechanics-based viscoplastic model of adapted complexity for high-temperature creepfatigue loading. *J. Eng. Gas Turbines Power*, 138:092501, 2016.

[61] T.W. Kim, D.H. Kang, J.T. Yeom and N.K. Park, Continuum damage mechanics-based creep-fatigue-interacted life prediction of nickel-based superalloy at high temperature. *Scr. Mater.*, 57:1149–1152, 2007.

[62] J.L. Chaboche and G. Rousselier. On the plastic and viscoplastic constitutive equations, part II: Applications of internal variable concepts to the 316 stainless steel. *ASME J. Press. Vessel Technol.*, 105:159–164, 1983.

[63] C.O. Frederick and P.J. Armstrong. A mathematical representation of the multiaxial bauschinger effect. *Mater. High Temp.*, 24:1–26, 2007.

[64] Y.P. Gong, C.J. Hyde, W. Sun, and T.H. Hyde. Determination of material properties in the chaboche unified viscoplasticity model. *J. Mater. Des. Appl.*, 224:19–29, 2009.

[66] K.B.S. Rodriguez, P. Rao. Materials challenges for nuclear systems. *Mater. Today*, 13(12): 14–23, 2010.

[66] T. Allen, J. Busby, M. Meyer, and D. Petti. Materials challenges for nuclear systems. *Mater. Today*, 13(12):14–23, 2010.

[67] Masoud Anahid, Mahendra K. Samal, and Somnath Ghosh. Dwell fatigue crack nucleation model based on crystal plasticity finite element simulations of polycrystalline titanium alloys. *J. Mech. Phys. Solids*, 2011.

[68] A. Argon. Mechanisms and mechanics of fracture in creeping alloys. *Recent Advances in Creep and Fracture of Engineering Materials and Structures. Pineridge press, Swansea*, pages 1–52, 1982.

[69] L. Balogh, S.R. Niezgoda, A.K. Kanjarla, D.W. Brown, B. Clausen, W. Liu, and C.N. Tom. Spatially resolved in situ strain measurements from an interior twinned grain in bulk polycrystalline AZ31 alloy. *Acta Mater.*, 61:3612–3620, 2013.

[70] G. Barenblatt. The formation of equilibrium cracks during brittle fracture. General ideas and hypotheses. Axially-symmetric cracks. *J. Appl. Math. Mech.*, 23:622–636, 1959.

[71] T. Belytschko, W.K. Liu, B. Moran, and K. Eikhodary. *Nonlinear Finite Elements for Continua and Structures*. John Wiley and Sons, New York, 2nd edition, 2014.

[72] J. Benz, T. Lillo, and R. Wright. Aging of alloy 617 at 650 and 750 °c. Technical report, Idaho National Laboratory, 2013.

[73] J. Benz, L. Carroll, J. Wright, R. Wright, and T. Lillo. Threshold stress creep behavior of Alloy 617 at intermediate temperatures. *Metall. Trans. A*, 45:3010–3022, 2014.

[74] Michael J. Bogdanor, Sankaran Mahadevan, and Caglar Oskay. Uncertainty quantification in damage modeling of heterogeneous materials. *Int. J. Multisc. Comp. Eng.*, 11:289–307, 2013.

[75] J. Bouvard, J. Chaboche, F. Feyel, and F. Gallerneau. A cohesive zone model for fatigue and creepfatigue crack growth in single crystal superalloys. *Int. Journal of Fatigue*, 31:868–879, 2009.

[76] V.V. Bulatov and W. Cai. *Computer Simulations of Dislocations*. Oxford University Press, Oxford, 2006.

[77] E. P. Busso and F. A. McClintock. A dislocation mechanics-based crystallographic model of a B2-type intermetallic alloy. *Int. J. Plast.*, 12:1–28, 1996.

[78] E.P. Busso, F.T. Meissonnier, and N.P. O'Dowd. Gradient-dependent deformation of two-phase single crystals. *J. Mech. Phys. Solids*, 48:2333–2361, 2000.

[79] R. Carmona, Q. Zhu, C.M. Sellars, and J.H. Beynon. Controlling mechanisms of deformation of AA5052 aluminium alloy at small strains under hot working conditions. *Mater. Sci. Eng. A*, 393:157–163, 2005.

[80] M.C. Carroll and L.J. Carroll. Developing dislocation subgrain structures and cyclic softening during high-temperature creepfatigue of a Nickel alloy. *Metall. Trans. A*, 44:3592–3607, 2013.

[81] A. Cerrone, J. Tucker, C. Stein, A. Rollett, and A. Ingraffea. Micromechanical modeling of RENE88DT:from characterization to simulation. In *Proceedings of the 2012 Joint Conference of the Engineering Mechanics Institute and the 11th ASCE Joint Specialty Conference on Probabilistic Mechanics and Structural Reliability*, 2012.

[82] Albert Cerrone, Paul Wawrzynek, Aida Nonn, Glaucio H. Paulino, and Anthony Ingraffea. Implementation and verification of the Park-Paulino-Roesler cohesive zone model in 3D. *Eng. Fract. Mech.*, 120:26–42, 2014.

[83] J.L. Chaboche. Constitutive equations for cyclic plasticity and cyclic viscoplasticity. *Int. J. Plast.*, 5:247–302, 1989.

[84] J. Cheng and S. Ghosh. A crystal plasticity FE model for deformation with twin nucleation in magnesium alloys. *Int. J. Plast.*, 67:148–170, 2015.

[85] J.W. Christian and S. Mahajan. Deformation twinning. *Prog. Mater. Sci.*, 39:1–157, 1995.

[86] D. Dugdale. Yielding of steel sheets containing slits. *J. Mech. Phys. Solids*, 8:100–104, 1960.

[87] M.G.D. Geers, M. Cottura, B. Appolaire, E.P. Busso, S. Forest, and A. Villani. Coupled glide-climb diffusion-enhanced crystal plasticity. *J. Mech. Phys. Solids*, 70:136–153, 2014.

[88] M.G.D. Geers, M. Cottura, B. Appolaire, E.P. Busso, S. Forest, and A. Villani. Coupled glide-climb diffusion-enhanced crystal plasticity. *J. Mech. Phys. Solids*, 70:136 – 153, 2014.

[89] D. Gonzalez, I. Simonovski, P.J. Withers, and J. Quinta da Fonseca. Modelling the effect of elastic and plastic anisotropies on stresses at grain boundaries. *Int. J. Plast.*, 61:49–63, 2014.

[90] M. Groeber and M. Jackson. DREAM.3D: A digital representation environment for the analysis of microstructure in 3D. *Integr. Mater. Manuf. Innov.*, 3:5–19, 2014.

[91] S. Hafez Haghighat, G. Eggeler, and D. Raabe. Effect of climb on dislocation mechanisms and creep rates in $\gamma'-$strengthened Ni base superalloy single crystals: A discrete dislocation dynamics study. *Acta Mater.*, 61:3709–3723, 2013.

[92] Craig S. Hartley. A method for linking thermally activated dislocation mechanisms of yielding with continuum plasticity theory. *Phil. Mag.*, 83(31-34):3783–3808, 2003.

[93] R. Hill and J.R. Rice. Constitutive analysis of elastic-plastic crystals at arbitrary strain. *J. Mech. Phys. Solids*, 20:401–413, 1972.

[94] R. Hu, C. Prakash, V. Tomar, M. Harr, I. Emre Gunduz, and C. Oskay. Experimentally-validated mesoscale modeling of the coupled mechanical–thermal response of ap–htpb energetic material under dynamic loading. *Int. J. Fract.*, 203:277–298, 2017.

[95] M. Huang, Z. Lia, and J. Tong. The influence of dislocation climb on the mechanical behavior of polycrystals and grain size effect at elevated temperature. *Int. J. Plast.*, 61:112–127, 2014.

[96] S. Jimenez and R. Duddu. On the parametric sensitivity of cohesive zone models for high-cycle fatigue delamination of composites. *Int. J. Solids and Struct.*, 82:111–124, 2016.

[97] S. R. Kalidindi. Incorporation of deformation twinning in crystal plasticity models. *J. Mech. Phys. Solids*, 46:267–290, 1998.

[98] M.E. Kassner. *Fundamentals of Creep in Metals and Alloys 3rd Edition.* Butterworth-Heinemann, 2015.

[99] M.E. Kassner and T.A. Hayes. Creep cavitation in metals. *Int. J. Plast.*, 19:1715–1748, 2003.

[100] S. Keshavarz and S. Ghosh. A crystal plasticity finite element model for flow stress anomalies in Ni_3Al single crystals. *Philos. Mag.*, 95:2639–2660, 2015.

[101] W. Kim, S. Yin, G. Lee, Y. Kim, and S. Kim. Creep oxidation behavior and creep strength prediction for Alloy 617. *Int. J. Press. Vessels Pip.*, 87:289–295, 2010.

[102] W. Kim, J. Park, I.M.W. Ekaputra, M. Kim, and Y. Kim. Analysis of creep behavior of Alloy 617 for use of VHTR system. *Procedia Mater. Sci.*, 3:1285–1290, 2014.

[103] W.G. Kim, J.Y. Park, I.M.W. Ekaputra, S.J. Kim, M.H. Kim, and Y.W. Kim. Creep deformation and rupture behavior of Alloy 617. *Eng. Fail. Anal.*, 58:441–451, 2015.

[104] W.-G. Kim, S.-N. Yin, J.-Y. Park, S.-D. Hong, and Y.-W. Kim. An improved methodology for determining tensile design strengths of alloy 617. *J. Mech. Sci. Technol.*, 26:379–387, 2012.

[105] M. Knezevic, A. Levinson, R. Harris, R.K. Mishra, R.D. Doherty, and S.R. Kalidindi. Deformation twinning in AZ31: Influence on strain hardening and texture evolution. *Acta Mater.*, 58:6230–6242, 2010.

[106] U. F. Kocks, C. N. Tome, and H. R. Wenk. *Texture and Anisotropy: Preferred Orientations in Polycrystals and Their Effect on Materials Properties*. Cambridge University Press, Cambridge, 1998.

[107] M. Kothari and L. Anand. Elasto-viscoplastic constitutive equations for polycrystalline metals: Application to tantalum. *J. Mech. Phys. Solids*, 46:51–83, 1998.

[108] D. Kupka, N. Huber, and E.T. Lilleodden. A combined experimental-numerical approach for elasto-plastic fracture of individual grain boundaries. *J. Mech. Phys. Solids*, 64:455–467, 2014.

[109] F.R. Larson and J. Miller. A time-temperature relationship for rupture and creep stresses. *Trans. ASME*, 74:765–771, 1952.

[110] R. Lebensohn, C. Hartley, C. Tomé, and O. Castelnau. Modeling the mechanical response of polycrystals deforming by climb and glide. *Philos. Mag.*, 90:567–583, 2010.

[111] R. Lebensohn, R. Holt, A. Caro, A. Alankar, and C. Tomé. Recent advances in micromechanics of materials: Improved constitutive description of single crystal viscoplastic deformation by dislocation climb. *C. R. Mécanique*, 340:289–295, 2012.

[112] Ricardo A. Lebensohn, Craig S. Hartley, Carlos N. Tome, and Olivier Castelnau. Modeling the mechanical response of polycrystals deforming by climb and glide. *Philos. Mag.*, 90:567–583, 2010.

[113] T. Lillo and R. Wright. Microstructural characterization of Alloy 617 crept into the tertiary regime. *Proceedings of the ASME 2015 Pressure Vessels and Piping Conference, PVP2015*, 2015.

[114] Thomas Lillo, James Cole, Megan Frary, and Scott Schlegel. Influence of grain boundary character on creep void formation in alloy 617. *Metallurgical and Materials Transactions A*, 40(12):2803–2811, 2009. ISSN 1073-5623.

[115] B. Lin, L.G. Zhao, J. Tong, and H.J. Christ. Crystal plasticity modeling of cyclic deformation for a polycrystalline nickel-based superalloy at high temperature. *Mater. Sci. Eng. A*, 527: 3581–3587, 2010.

[116] A. Ma and F. Roters. A constitutive model for FCC single crystals based on dislocation densities and its application to uniaxial compression of aluminium single crystals. *Acta Mater.*, 52:3603–3612, 2004.

[117] W.L. Mankins, J.C. Hosier, and T.H. Bassford. Microstructure and phase stability of inconel alloy 617. *Metall. Trans.*, 5:2579–2590, 1974.

[118] E. B. Marin. On the formulation of a crystal plasticity model. Technical report, Sandia National Laboratories, 2006.

[119] E.B. Marin and P.R. Dawson. On modelling the elasto-viscoplastic response of metals using polycrystal plasticity. *Comput. Methods Appl. Mech. Engrg.*, 165:1–21, 1998.

[120] S.F. Di Martino, R.G. Faulkner, S.C. Hogg, S. Vujic, and O. Tassa. Characterisation of microstructure and creep properties of Alloy 617 for high-temperature applications. *Mater. Sci. Eng. A*, 619:77–86, 2014.

[121] S.F. Di Martino, R.G. Faulkner, S.C. Hogg, S. Vujic, and O. Tassa. Characterisation of microstructure and creep properties of alloy 617 for high-temperature applications. *Mater. Sci. Eng. A*, 619:77–86, 2014.

[122] Kun Mo. *Microstructural Evolution and Mechanical Behavior in Nickel based Alloy for Very High Temperature Reactor*. PhD thesis, University of Illinois at Urbana-Champaign, 2011.

[123] Kun Mo, Gianfranco Lovicu, Xiang Chen, Hsiao-Ming Tung, Jon B. Hansen, and James F. Stubbins. Mechanism of plastic deformation of a ni-based superalloy for VHTR applications. *J. Nucl. Mater.*, 441:695 – 703, 2013.

[124] Kun Mo, Gianfranco Lovicu, Hsiao-Ming Tung, Xiang Chen, Yinbin Miao, Jon B. Hansen, and James F. Stubbins. Effect of orientation on plastic deformations of alloy 617 for VHTR applications. *J. Nucl. Mater.*, 443:366–377, 2013.

[125] F.R.N Nabarro. Steady-state diffusional creep. *Philos. Mag.*, 16:231, 1967.

[126] Shahriar Quayyum Nazrul Islam and Tasnim Hassan. A unified constitutive model for high temperature multiaxial creep-fatigue and ratcheting response simulation of alloy 617. In *ASME Proceedings 22nd Scavuzzo Student Paper Symposium and Competition*, 2014.

[127] P. Onck and E. van der Giessen. Microstructurally-based modelling of intergranular creep fracture using grain elements. *Mech. Mater.*, 26:109–126, 1997.

[128] P. Onck and E. van der Giessen. Micromechanics of creep fracture: simulation of intergranular crack growth. *Comput. Mater. Sci.*, 13:90–102, 1998.

[129] C. Oskay. Variational multiscale enrichment method with mixed boundary conditions for modeling diffusion and deformation problems. *Comput. Methods Appl. Mech. Engg.*, 264:178–190, 2013.

[130] C. Oskay and J. Fish. Eigendeformation-based reduced order homogenization for failure analysis of heterogeneous materials. *Comput. Methods Appl. Mech. Engrg.*, 196:1216–1243, 2007.

[131] Caglar Oskay. Variational multiscale enrichment for modeling coupled mechano-diffusion problems. *Int. J. Numer. Methods Eng.*, 89(6):686–705, 2012.

[132] Caglar Oskay and Mark Haney. Computational modeling of titanium structures subjected to thermo-chemo-mechanical environment. *Int. J. Solids Struct.*, 47(24):3341–3351, 2010.

[133] D. Peirce, R.J. Asaro, and A. Needleman. An analysis of nonuniform and localized deformation in ductile single crystals. *Acta Metall.*, 30:1087–1119, 1982.

[134] D. Peirce, R.J. Asaro, and A. Needleman. Material rate dependence and localized deformation in crystalline solids. *Acta Metall.*, 31:1951–1976, 1983.

[135] H. Pottebohm, G. Neite, and E. Nembach. Elastic properties (the stiffness constants, the shear modulus and the dislocation line energy and tension) of Ni-Al solid solutions and of the nimonic alloy PE16. *Mater. Sci. Eng. A*, 60:189–194, 1983.

[136] M.J.D. Powell. A fast algorithm for nonlinearly constrained optimization calculations. In G.A. Watson, editor, *Numerical Analysis*, volume 630 of *Lecture Notes in Mathematics*, pages 144–157. Springer Berlin Heidelberg, 1978.

[137] P.G. Pritchard, L. Carroll, and T. Hassan. Constitutive modeling of high temperature uniaxial creep-fatigue and creep-ratcheting responses of alloy 617. In *Proceedings of the ASME 2013 Pressure Vessels and Piping Conference*, 2013.

[138] C. Rasmussen and C. Williams. *Gaussian Processes for Machine Learning*. Springer, New York, 2006.

[139] W. Ren and R. W. Swindeman. A review on current status of alloys 617 and 230 for Gen IV nuclear reactor internals and heat exchangers. *ASME. J. Pressure Vessel Technol.*, 131, 2009.

[140] D.N. Robinson. Constitutive relationships for anisotropic high-temperature alloys. *Nucl. Eng. Des.*, 83:389–396, 1984.

[141] F. Roters, P. Eisenlohr, L. Hantcherli, D.D. Tjahjanto, T.R. Bieler, and D. Raabe. Overview of constitutive laws, kinematics, homogenization and multiscale methods in crystal plasticity finite-element modeling: Theory, experiments, applications. *Acta Mater.*, 58:1152–1211, 2010.

[142] F. Roters, P. Eisenlohr, T.R. Bieler, and D. Raabe. *Crystal Plasticity Finite Element Methods*. John Wiley and Sons, New York, 1st edition, 2013.

[143] A. Roy, M. Hasan, and J. Pal. Deformation of Alloys 617 and 276 at $750 - 950°C$. *Mater. Sci. Eng. A*, 520:184–188, 2009.

[144] M. Shenoy, J. Zhang, and D. McDowell. Estimating fatigue sensitivity to polycrystalline Ni-base superalloy microstructures using a computational approach. *Fatigue Fract Eng M Journal*, 30:889–904, 2007.

[145] M.M. Shenoy, A.P. Gordon, D.L. McDowell, and R.W. Neu. Thermomechanical fatigue behavior of a directionally solidified Ni-base superalloy. *J. Eng. Mater. Technol.*, 127:325–336, 2005.

[146] O.D. Sherby and P.M. Burke. Mechanical behavior of crystalline solids at elevated temperature. *Prog. Mater. Sci.*, 13:323–390, 1968.

[147] Y. Shi, K. Yuan, X. Zhao, and Y. Wu. Study on comparison between Inconel 617 and Gh3128 as structural material candidates for intermediate heat exchanger. In *Proceedings of the 2013 21st International Conference on Nuclear Engineering ICONE21*. ASME, 2013.

[148] K. Shiozawa and J. Weertman. Studies of nucleation mechanisms and the role of residual stresses in the grain boundary cavitation of a superalloy. *Acta Metall.*, 31, 1983.

[149] I. Simonovski and L. Cizelj. Cohesive element approach to grain level modelling of intergranular cracking. *Engng. Fract. Mech.*, 110:364–377, 2013.

[150] I. Simonovski and L. Cizelj. Cohesive zone modeling of intergranular cracking in polycrystalline aggregates. *Nucl. Eng. Des.*, 283:139–147, 2015.

[151] D. Spring and G. Paulino. A growing library of three-dimensional cohesive elements for use in ABAQUS. *Engng. Fract. Mech.*, 126:190–216, 2014.

[152] A. Staroselsky and B. N. Cassenti. Creep, plasticity, and fatigue of single crystal superalloy. *Int. J. Solids Struct*, 48:2060–2075, 2011.

[153] J.C. Stinville, N. Vanderesse, F. Bridier, P. Bocher, and T.M. Pollock. High resolution mapping of strain localization near twin boundaries in a nickel-based superalloy. *Acta Mater.*, 98: 29–42, 2015.

[154] J.C. Stinville, W.C. Lenthe, J. Miao, and T.M. Pollock. A combined grain scale elasticplastic criterion for identification of fatigue crack initiation sites in a twin containing polycrystalline nickel-base superalloy. *Acta Mater.*, 103:461–473, 2016.

[155] Y. Sun, K. Maciejewski, and H. Ghonem. A damage-based cohesive zone model of intergranular crack growth in a nickel-based superalloy. *Int. J. Damage Mech.*, 22(6):905–923, 2013.

[156] R.W. Swindeman and Swindeman M.J. A comparison of creep models for Nickel base alloys for advanced energy systems. *Proceeding of ECCC Creep Conference, 12-14 September 2005, London*, 2005.

[157] E.M. Taleff, W.P. Green, M.-A. Kulas, T. R. McNelley, and P.E. Krajewski. Analysis, representation, and prediction of creep transients in class I alloys. *Mater. Sci. Eng. A*, 410-411: 32–37, 2005.

[158] G.I. Taylor. Plastic Strain in Metals. *J. Inst. Met.*, 62:307–324, 1938.

[159] T. C. Totemeier, H. Tian, D. E. Clark, and J. A. Simpson. Microstructure and strength characteristics of alloy 617 welds. Technical report, Idaho National Laboratory, 2005.

[160] H.S. Turkmen, P.R. Dawson, and M.P. Miller. The evolution of crystalline stresses of a polycrystalline metal during cyclic loading. *Int. J. Plast.*, 18:941–969, 2002.

[161] Xingshuo Wen. *Creep Behavior of High Temperature Alloys for Generation IV Nuclear Energy Systems*. PhD thesis, University of Cincinnati, 2014.

[162] J. Wright, L. Carroll, and R. Wright. Creep and creep-fatigue of Alloy 617 weldments. *Tech. Rep., Idaho National Laboratory*, 2014.

[163] J. K. Wright, L. J. Carroll, C. Cabet, T. M. Lillo, J.K. Benz, J. A. Simpson, W. R. Lloyd, J. A. Chapman, and R. N. Wright. Characterization of elevated temperature properties of heat exchanger and steam generator alloys. *Nucl. Eng. Des.*, 251:252–260, 2012.

[164] J. K. Wright, L. J. Carroll, J. A. Simpson, and R. N. Wright. Low cycle fatigue of alloy 617 at 850°C and 950°C. *J. Eng. Mater. Technol.*, 135:031005, 2013.

[165] J. K. Wright, N. J. Lybeck, and R. N. Wright. Tensile properties of alloy 617 bar stock. Technical report, Idaho National Laboratory, 2013.

[166] J.K. Wright, J.A. Simpson, R.N. Wright, L.J. Carroll, and T.L. Sham. Strain rate sensitivity of alloys 800h and 617. In *Proceedings of the 2013 ASME Pressure Vessels & Piping Conference*, Paris, France, 2013.

[167] H. Yang, M. Huang, and Z. Li. The influence of vacancies diffusion-induced dislocation climb on the creep and plasticity behaviors of Nickel-based single crystal superalloy. *Comp. Mat. Sc.*, 99:348–360, 2015.

[168] M.H. Yoo and J.K. Lee. Deformation twinning in h.c.p. metals and alloys. *Phil. Mag. A*, 63: 987–1000, 1991.

[169] J. Zhang. *High temperature deformation and fracture of materials*. Woodhead Publishing, 2010.

[170] K.-. Zhang, J.W. Ju, Z. Li, Y.-L. Bai, and W. Brocks. Micromechanics based fatigue life prediction of a polycrystalline metal applying crystal plasticity. *Mech. Mater.*, 85:16–37, 2015.

[171] M. Zhang, J. Zhang, and D.L. McDowell. Microstructure-based crystal plasticity modeling of cyclic deformation of Ti-6Al-4V. *Int. J. Plast.*, 23:1328–1348, 2007.

[172] Shuhai Zhang and Caglar Oskay. Variational multiscale enrichment method with mixed boundary conditions for elasto-viscoplastic problems. *Comput. Mech.*, 55:771–787, 2015.

[173] Shuhai Zhang and Caglar Oskay. Reduced order variational multiscale enrichment method for elasto-viscoplastic problems. *Comput. Methods Appl. Mech. Engg.*, 300:199–224, 2016.

[174] X. Zhang and C. Oskay. Polycrystal plasticity modeling of nickel-based superalloy IN 617 subjected to cyclic loading at high temperature. *Modelling Simul. Mater. Sci. Eng.*, 24:055009, 2016.

[175] Xiang Zhang and Caglar Oskay. Eigenstrain based reduced order homogenization for polycrystalline materials. *Comput. Methods Appl. Mech. Engg.*, 297:408–436, 2015.